SISSA

INTERNATIONAL SCHOOL FOR ADVANCED STUDIES

PHD COURSE IN THEORY AND NUMERICAL SIMULATION OF CONDENSED MATTER

Sliding Nanofriction In Low Dimensional Model-Systems

Thesis submitted for the degree of
Doctor Philosophiae

Candidate:
Davide MANDELLI

Supervisor:
Prof. Erio TOSATTI

Academic Year 2014-2015

Contents

Abstract

Thanks to novel experimental techniques, physicists are now able to characterize the dynamics of interacting surfaces down to molecular length scales. This possibility has brought fresh interest in the field of friction and has opened a new branch of research, *nanotribology*, whose aim is the study of tribological properties of sliding systems in terms of fundamental atomistic dissipative mechanisms. Far from being a mere academic problem, understanding and controlling friction at the nano-scales can have a great impact on many technological applications, from energy conversion and saving, to transportation and micro-machining. To reach this goal it is essential to develop theoretical tools able to tackle this problem. In absence of a general theory of friction, molecular dynamics (MD) simulations represent, at the moment, one of the most powerful approaches able to explain and predict the behaviour of nanoscale interfaces. Within the context of nanotribology, this thesis deals with some fundamental aspects of friction between dry crystalline surfaces. Anticipating experiments, it reports results obtained by means of realistic MD simulations of artificial model-systems currently under experimental investigation for application in nanotribology.

Qualitatively, the sliding properties of crystalline interfaces can be interpreted based on the mutual interaction between the potential energy landscapes generated by the two touching lattices. These may be described as periodic, two dimensional sequences of wells and hills, corresponding to repulsive and attractive regions of the surfaces. Commensurate geometries correspond to atomically locked configurations, where the atoms of each interacting plane adapt into the wells of the potential landscape generated by the other one. When driven out of equilibrium by an applied shear force, this kind of atomic locking, or interdigitation, generally determines mechanical instabilities, which in turn lead to violent depinning events and high dissipation. Atomic locking may still occur, but may also be avoided in incommensurate interfaces, in which case friction shows more smooth and gentle sliding regimes. The ordered atomic arrangement of crystalline surfaces therefore offers a peculiar way to reduce friction, that is by controlling the geometry of the interface, e.g., by rotating relative to each other two originally aligned and commensurate surfaces.

The above picture applies to clean, chemically inert, and atomically flat crystal surfaces. To describe in a quantitative way real systems, one has to take into account many other effects whose interplay determine the overall tribological response. They include elasticity of the surfaces, plastic deformations, and the presence of steps, defects and impurities, not counting chemical interactions and other processes involving the direct excitations of electronic degrees of freedom. From the experimental point of view, the fine features of the interface are hardly accessible because buried. Usually only macroscopic average values of some arising physical quantities are measured, which hinders the possibility to keep track of each distinct mechanism at play. From the theoretical point of view, developing a general theory different from brute-force with

quantitative predictive power is also difficult, and phenomenological models are usually adopted which apply only to a reduced number of cases. However, there exist a class of real systems where these complications are absent or mitigated, allowing for detailed experimental and theoretical investigations. On one hand, one (1D) and two dimensional (2D) artificial crystals of charged particles trapped inside optical lattices offer the possibility to study the dynamics of ideal crystalline interfaces with all interface parameters under control, including commensurability and substrate interaction strength. On the other hand, surface science and ultra high vacuum techniques supply clean and atomically flat substrates, suitable for the study of the sliding properties of two dimensional monolayers of adsorbate atoms. Both these systems are very well characterized, and allow for accurate realistic MD simulations where geometrical effects, and interface elastic and plastic deformations effects are investigated in great details.

In view of future experiments, this thesis reports results of MD investigations of some fundamental tribological aspects in low dimensional incommensurate interfaces formed by: (i) 1D cold-ion chains trapped in optical lattices, (ii) 2D charged colloids monolayers interacting with laser-induced periodic potentials, (iii) 2D islands of rare gas atoms physisorbed on clean metallic substrates. These simulations show that incommensurate linear chains of trapped cold ions display a rich dynamics when forced to slide over a periodic corrugated potential. That suggests that they can be adopted to investigate in detail the external-load dependent transition between the intermittent stick-slip motion and the smooth sliding regime, as well as the precursor dynamics preceding the onset of motion. Both of them are shown to display paradigmatic behaviours observed in sliding contacts at any length scales. Incommensurate two dimensional interfaces realized by colloidal crystals in periodic fields have been simulated to study the pinning transition from the locked (finite static friction) state, to the "superlubric" – zero static friction – free-sliding state, which is predicted to occur as a function of decreasing substrate potential strength. In a range of parameters compatible with recent experiments, that is a first order (structural) phase transition of the colloid monolayer, showing analogies with the superlubric to pinned "Aubry transition" extensively studied in the one dimensional discrete Frenkel-Kontorova model of dry friction. Moreover, realistic simulations show that relative misfit rotations between the colloidal slider and substrate may significantly affect the dissipation under steady sliding even in genuinely incommensurate geometries, by changing the degree to which the soft deformable slider interdigitates within the hard, non deformable optical substrate. This is a result of more general validity, since a similar mechanism must be at play in any incommensurate 2D crystalline interface. Finally, in order to understand the persistent static friction force observed in quartz crystal microbalance experiments on highly clean surfaces, extensive numerical simulations of substrate-incommensurate model rare-gas islands have been performed, which, in absence of any other sources of pinning, describe how the island edges alone may play the ultimate role in determining the overall barrier preventing the onset of global sliding.

CHAPTER 1

Introduction and Motivations

Tribology is the branch of physical science dealing with adhesion, friction and interface rheology. Nanotribology is the branch of tribology concerning the study of nanometer size contacts, where atomic details start playing a relevant role in determining the sliding properties of the interface. This thesis is devoted to the investigation of some fundamental aspects of sliding friction between dry crystalline surfaces. To this aim we report theoretical investigations based on realistic molecular dynamics simulations of artificial "toy-models", recently proposed as tools for applications in nanotribology.

1.1   Background

Frictional interaction between sliding bodies is an old problem in physics, and one of the most important from a practical point of view. When two bodies slide against each other non-conservative forces arise resisting their motion, which transform – *dissipate* – kinetic energy into internal energy, sometimes causing irreversible damages to the surfaces. Large friction is important in many practical applications, e.g., car tires. On the other hand, reducing dissipation and wear is of primary concern in many human activities. It has been estimated that improvement in tribology would allow to save about $1.6\,\%$ of the gross national product in developed countries [1]. However, friction is a complex problem, and despite its great technological relevance, we are still far from a general theory of friction able to give quantitative predictions.

 The basic laws of dry frictional sliding, i.e., without lubrication, between macroscopic bodies are almost five centuries old [2], and can be summarized as follows. A force F_s – the *static friction force* – is needed to start the motion of a rigid body initially at rest. When sliding is initiated, steady state motion may be maintained by applying a force F_D – the *dynamic friction force* – whose work is dissipated via Joule heating both inside the slider and the substrate, or converted into plastic deformations of the interface. The well known (Amontons-Coulomb) macroscopic friction laws state that:

1. F_s and F_d are independent on the apparent area of contact between the objects;

2. Both static and dynamic friction are proportional to the applied load N: $F_s = \mu_s N$, $F_d = \mu_d N$. The friction coefficients $\mu_{d,s}$ depend only on specific material properties, and usually $\mu_d < \mu_s$.

A third law is usually attributed to Coulomb and states that μ_d does not depend on the sliding velocity, at least for ordinary sliding speeds. From everyday life experience we are all quite familiar with these phenomenological statements, which are reasonably well obeyed for a wide variety of materials, but when one tries to justify them from a microscopic point of view the problem shows up to be one of great complexity. The first attempt to describe the origin of dissipative sliding starting from general principles dates back to the work of Coulomb. Without a proper knowledge of the atomic structure of matter he considered whether dissipation could arise from the interlocking of macroscopic *rigid* asperities. In his model he assumed that dissipation amounts to the energy needed to lift up the two surfaces in order to allow asperities to slide past each other. However, he was forced to rule out this hypothesis as the work done against the loading force in order to separate the sliding bodies can be in principle completely regained once the interface reaches a new interlocked configuration. After that, energy dissipation was for long correlated only to the presence of wear, even though the obvious idea that increased surface roughness will always lead to an increase in friction persisted.

A lack of experimental apparatuses with the required sensitivity and with atomistic characterization is the main reason why for long there have not been many progresses in the field of tribology. The first step towards this goal coincided with the improvement in ultra high vacuum techniques (UHV) and surface science occurred between 1950 and 1970 [3]. This made possible for the first time the routine preparation of crystalline surfaces in controlled conditions where they could be characterized using electron spectroscopy techniques [4–7]. Fundamental advances in understanding friction were made in the same years thanks to the development of the surface force apparatus [8] (SFA), which allowed the measurement of forces between atomically flat surfaces only few nanometers apart. The work of Bowden and Tabor [9] constitutes a major contribution in clarifying the origin of macroscopic friction. They documented that when two bodies touch each other the actual area of contact can be several orders of magnitude smaller than the apparent macroscopic area. The surfaces of extended bodies are far from being atomically flat but rather consist of many protruding asperities exhibiting high yield stress. As a result, macroscopic friction is independent on the apparent area of contact, but it is in fact proportional to the true contact area A_c, given by the sum of all microscopic junctions formed by those asperities. Macroscopic friction is easily related to the real contact area assuming that, under sliding, microscopic contacts continuously break and reform. Dynamic friction is therefore set equal to the "adhesive" forces of such junctions. Considering A_c to be approximately constant during sliding, the friction force can be written as $F_d = sA_c$, where s is the shear stress of the material, i.e., the shear force per unit area needed to sustain motion. Further assuming the pressure P to be equally distributed over all the microscopic junctions, one can write $P = N/A_c$, yielding $\mu_d = s/P$. In many systems adhesive forces are much larger than externally applied loads, and s does not depend on N. For a wide range of materials and surface topologies it is also well established that the area of contact is proportional to the applied load, $A_c \propto N$. In these cases both s and P can be directly related to the macroscopic yield stress of the softer material, then μ_d is effectively unaffected by changes of the load, and becomes a material dependent constant. Deviations from Amontons' law are in fact quite evident in layered materials such as graphite, where the interlayer interaction is relatively weak and the friction coefficient does become load-dependent. The velocity dependence of the macroscopic dynamic friction coefficient is also evident, as shown, e.g., in Ref. [10].

While describing changes in friction due to load variations, the analysis of Bowden and Tabor does not give any clue on the mechanisms behind energy dissipation. Early SFA experiments definitely ruled out interlocking between microscopic asperities. Substantial changes in friction
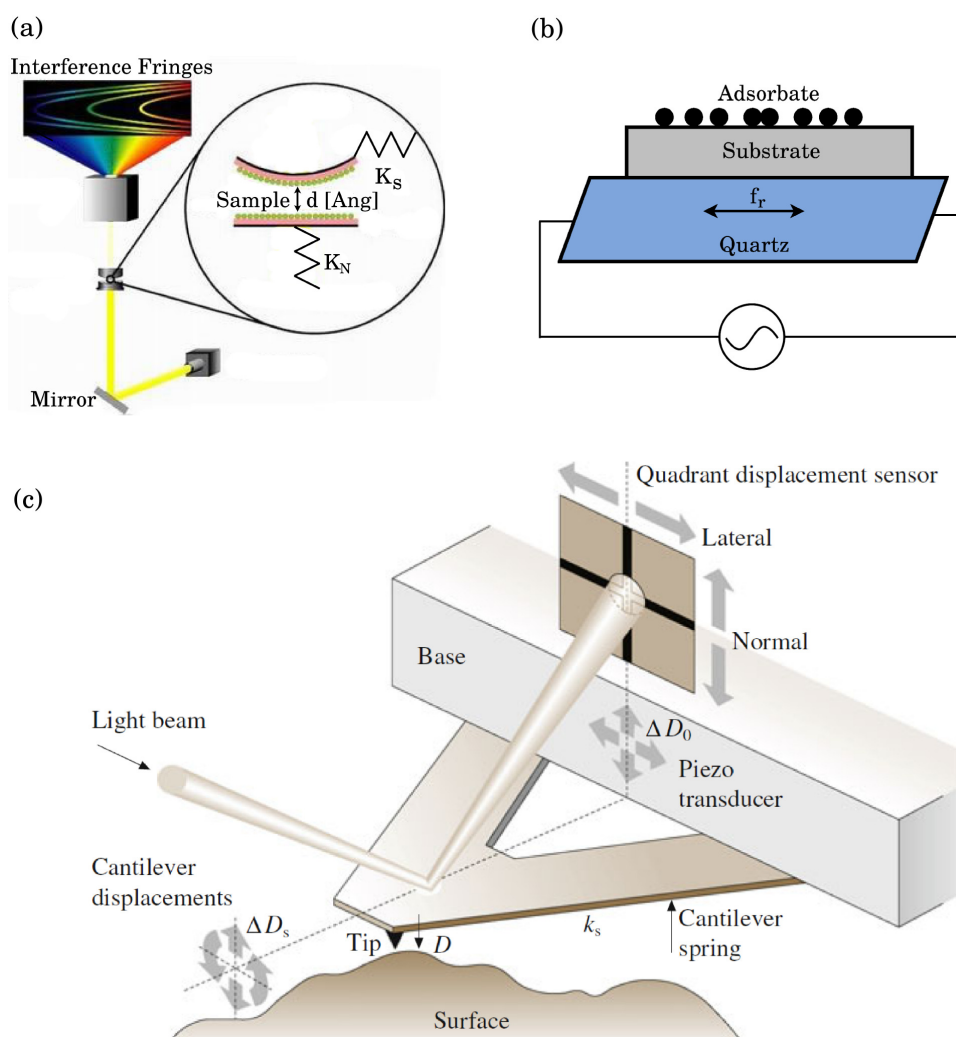
Figure 1.1: (a) Schematics of a surface force apparatus. Two springs K_n and K_s are used to measure normal and shear forces of a sample squeezed between two hard and molecularly flat surfaces. The distance d between the two supports is constantly monitored using the interference fringes of a light beam passing through the molecularly narrow slit formed by the interface. (b) In quartz crystal microbalance experiments, full monolayers, or islands of rare gas atoms are physisorbed over an atomically flat and clean substrate, fixed to the surface of a quartz oscillator. Shifts in the resonant frequency f_r, and the damping of the quartz crystal oscillations are used to study the dissipative inertial sliding of the adsorbate film. (c) A detailed scheme of an atomic force microscopy experiment, in which a nanoscopic tip is dragged over a surface. Lateral and vertical displacements are measured with atomic resolution by the deflections of a laser beam shone on the moving cantilever. Knowing the effective stiffness of the cantilever allow for the measurements of shear and normal frictional forces with sensitivity down to the bond strength of single molecules.

were in fact measured after coating the sliding surfaces with single molecular layers, which leave surface roughness basically unaffected. Moreover, the existence of friction in complete absence of wear was demonstrated by measuring shear forces between atomically flat mica surfaces. To explain these observations new fundamental mechanisms of wear-free friction involving phonons

and – for conducting materials – electronic excitations need to be considered, which ultimately require the study of processes intimately related to the atomic structure of the interfaces. Studying these phenomena is a possibility only recently achieved in experiments, and which has brought fresh interest in the field of friction [11]. New experimental techniques are now capable to study the problem of dissipation in systems with well defined contact geometries. Among them the SFA (see Fig. 1.1a) is used to measure adhesion and force laws of lubricant layers squeezed between two curved, molecularly smooth surfaces. The shape of interference fringes is used to measure the surface separation with high sensitivity, below 1 nm. From the shape of the interference fringes one also obtains the radius of the surfaces, and any deformation induced by their mutual interaction [12–14]. Different materials are used to form the surfaces in the SFA, including mica [15, 16], silica [17], sapphire [18], and polymer sheets [19]. Coating of the two rigid surfaces enables the study of boundary lubricated friction between adsorbed or chemically bound polymer layers [20–26], surfactant and lipid monolayers and bilayers [27–30], metal and metal-oxide layers [31–38]. The range of liquids and vapours that can be used include aqueous solutions, organic liquids and solvents, polymer melts, various petroleum oils and lubricant liquids, dyes, and liquid crystals. Improved techniques [39] allow for the two surfaces to be sheared laterally past each other at varying sliding speeds or oscillating frequencies, while simultaneously measuring both the transverse force and the normal force between them. The ranges of friction forces and sliding speeds that can be studied with such methods are currently 10^{-7}-10^{-1} N and 10^{-13}-10^{-2} m/s, respectively. The externally applied load N can be varied continuously, and both positive and negative loads can be applied. The distance between the surfaces D, their true molecular contact area, their elastic or viscoelastic deformation, and their lateral motion can all be monitored simultaneously by recording the moving interference-fringe pattern.

In 1959 Sauerbrey [40] recognized the extremely sensitive nature of piezoelectric devices based on quartz resonators. Later, quartz crystal microbalance (QCM) experiments were adapted to friction measurements by Krim and Widom [41]. A QCM consists of a single crystal of quartz that oscillates in transverse shear motion, at typical frequencies of 5-10 MHz, and with very little internal dissipation. The oscillations are driven by an alternating voltage applied to metal electrodes deposited on the surface of the quartz (see Fig. 1.1b). The figure of merit of the oscillator is the quality factor $Q = f_r/\omega$, given by the ratio between the resonant frequency f_r and the linewidth ω. Atomically thin films adsorbed onto the QCM electrodes produce shifts in both the frequency and the quality factor Q, which are indicative of the degree to which the films are able to follow the oscillatory motion of the underlying substrate. Shifts in the resonant frequency, δf, are associated with changes of the oscillating mass, while inverse quality factor shifts, $\delta(Q^{-1})$, generally manifested as decreases in the amplitude of vibration. For submonolayer clusters and monolayer adsorbates, dissipation due to viscoelasticity of the oscillating mass can be neglected, and shifts in the quality factor arise only from frictional losses associated with the dissipative sliding of the adsorbate. In this case the sliding friction F_d is well described by a viscous law [42–44]:

$$F_d = \eta v = \frac{mv}{\tau}, \tag{1.1}$$

where m is the sliding mass, η is the frictional damping coefficient, and τ is the characteristic "slip-time" in which the velocity of the slider decays by a factor $1/e$ of its initial value, when given an initial velocity and then released. The frequency and quality factor shifts are related to the slip time by [41]

$$\delta(Q^{-1}) = -4\pi\tau\delta f. \tag{1.2}$$

Given the two dimensional density ρ of the adsorbate, one can extract the frictional damping

coefficient $\eta = \rho A/\tau$, where A is the coverage area. Quality factors are relatively high in shear-mode oscillations, typically 10^6. Common equipment allows resolution down to 1 Hz for the resonant frequency. Because of its high frequency stability and high Q, a QCM can detect mass changes as small as 1 pg/cm^2. This technique can be employed up to 573° C, above which crystalline quartz loses its piezoelectric properties. The high sensitivity of the QCM resonant frequency f_r to changes in the physisorbed inertial mass, enables the controlled deposition of fixed amount of adsorbate corresponding to single and multiple layers, or sub monolayers, where the atoms are likely to form separated islands of different sizes. Once the target amount of atoms have been deposited, slowly increasing the oscillations' amplitude induces changes in the inertial mass as soon as the adsorbed atoms are no more able to track the substrate oscillations, and therefore slip, driven by their own inertial force. The subsequent abrupt shift of f_r signals the depinning of the adsorbate, allowing to estimate the static friction force of the interface. QCM measurements yielded the first definitive experimental evidence for existence of both phononic [45] and electronic [46, 47] friction mechanisms in sliding adsorbed layers, and are routinely applied to study the adsorbate depinning transition, and sliding friction as a function of temperature [48–50] and substrate coverage [51, 52].

In atomic force microscopy [53, 54] (AFM) a submicrometer tip is mounted on a soft cantilever and it is dragged over a crystalline surface, as depicted in Fig. 1.1c. Keeping the tip in contact with the surface, lateral forces are measured monitoring the deflection of the cantilever. Distances can be inferred with an accuracy of about 1 nm, and changes in distance can be measured to about 0.1 nm, allowing to obtain images with atomic resolution. The normal stiffness of the cantilever can be as small as 1 pN, enabling measurements of adhesion forces corresponding to the bond strength of single molecules [55–58]. AFM techniques have proved to be very flexible. Phononic and electronic contributions to dissipation have been probed successfully [59, 60]. Measurements can be carried out in different conditions, including in a vapour or liquid [61]. Using the tip as a "rake" one can study nanoscale friction by dragging nano-particles [62]. Weak interaction forces and larger microscopic interaction areas can be investigated by replacing the tip with a micrometer-sized sphere to form a colloidal probe [63]. Particularly interesting is the possibility to probe the effects of tip-substrate coupling mediated by long range interactions. The extreme sensitivity of this non-contact mode experiments recently allowed to discriminate, in a single experiment, between the phononic and electronic contributions to dissipation across the superconducting transition of a Nb film [64].

Thanks to these breakthroughs, experimentalists can now address friction at single, well defined interfaces where surfaces are in full contact, rather than characterizing the global properties of extended contacts in which many different interfaces are hidden. While experiments are giving unprecedented information on the sliding dynamics of real crystalline contacts, accurate theoretical modeling is mandatory for a deeper understanding of friction, aiming at controlling dissipation and designing efficient interfaces. The amount of fresh experimental data gathered in the last two decades has inspired much theoretical work on atomistic fundamentals of friction based on phononic and electronic energy dissipation mechanisms. From the theoretical point of view, describing frictional sliding is a challenging problem. The main difficulty comes from the highly non-linear nature of the phenomena taking place at the interface. Dissipation is usually related to mechanical instabilities involving the fast motion of microscopic degrees of freedom, a regime where standard techniques such as linear-response fail. On one hand many efforts have been made in order to construct theoretically tractable models able to encompass the complexity of actual systems while retaining the important features of friction. On the other hand advances in computational science allow theorists to simulate more complex systems. Beside its funda-
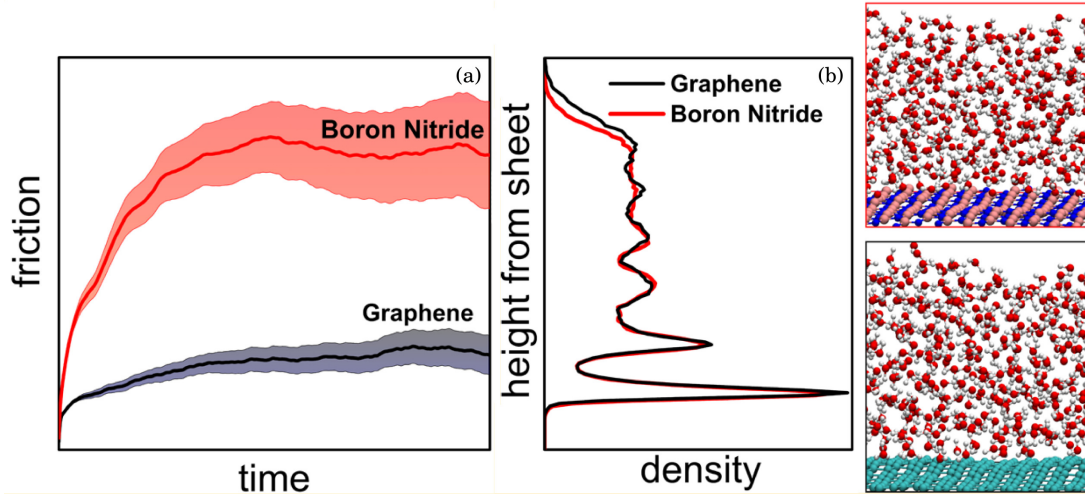
Figure 1.2: (a) The friction force of water flowing in contact with boron nitride (hBN) and graphene, calculated applying Eq. (1.9) to equilibrium ab-initio MD simulations. Despite water at equilibrium shows the same structure, as seen from the density profile of panel (b), friction is higher in contact with hBN. On the right the simulation supercells used in the simulations by Tocci and coworkers [65] are shown: top box for hBN, bottom box for graphene. (Adapted from Ref. [65])

mental importance, characterizing the physics of ideal atomistic nano-contacts is impelling also from a practical point of view. Novel applications in nanotechnologies involve the miniaturization of mechanical components, where the increased surface/volume ratio greatly enhances surface effects, and calls for a detailed investigation of the interface dynamics down to molecular length scales.

In Section 1.2 we briefly review some general theoretical results on viscous frictional sliding. In Section 1.3 and Section 1.4 we discuss two topics of interest in nanotribology, that are *stick-slip motion* and *structural lubricity*, elucidating basic concepts of relevance for the investigations presented in this thesis. In Section 1.5 we describe how MD simulations are used to investigate nanoscale tribology. Section 1.6 is devoted to the description of the artificial models we choose as our prototypical frictional systems, where dissipation can be studied experimentally in highly controlled conditions, and which allow for accurate theoretical investigations in realistic molecular dynamics simulations. Finally, Section 1.7 outlines the organization of this thesis.

1.2 Linear response friction

In the limit of small sliding speeds and in a regime of gentle motion, when violent slip events are absent and the slider is weakly perturbed by the external forces, dissipation is usually of viscous type and the damping coefficient can be calculated using theoretical approaches based on linear response.

A general formulation of linear response theory in liquid systems out of equilibrium is readily developed in the framework of statistical mechanics. A detailed treatment can be found, e.g., in Ref. [66], here we only give the general results. The basic assumptions are as follows. A system of N particles is taken to be at equilibrium at times $t \leq 0$ and described, e.g., by a canonical

distribution function at some given temperature T

$$f_c(\mathbf{\Gamma}) = \frac{\exp(-\beta H_0(\mathbf{\Gamma}))}{\int d\mathbf{\Gamma} \exp(-\beta H_0(\mathbf{\Gamma}))}, \tag{1.3}$$

where

$$H_0(\mathbf{\Gamma}) = \sum_{i=1}^{N} \frac{p_i^2}{2m} + \Phi(\{\mathbf{q}_i\}) \tag{1.4}$$

is the unperturbed Hamiltonian of the system, $\beta = 1/k_B T$, and $\mathbf{\Gamma} = (\{\mathbf{q}_i\}, \{\mathbf{p}_i\})$ indicates the collection of all phase space variables. At $t = 0$ an external field $F_{\text{ext}}(t)$ is switched on which couples to the internal degrees of freedom. We assume that the time evolution of the system is governed by the following equations of motion

$$\begin{aligned} \dot{\mathbf{q}}_i &= \frac{\mathbf{p}_i}{m_i} + \mathbf{C}_i F_{\text{ext}}(t) \\ \dot{\mathbf{p}}_i &= \mathbf{F}_i + \mathbf{D}_i F_{\text{ext}}(t) \end{aligned} \tag{1.5}$$

where $\mathbf{F}_i$ is the total force acting on the *i-th* particle due to (internal) interactions with all the other particles, while $\mathbf{C}_i(\mathbf{\Gamma})$ and $\mathbf{D}_i(\mathbf{\Gamma})$ describe the coupling of the system to the external field. Since the external field performs work on the system, the starting distribution function will change in time from $f_c(\mathbf{\Gamma})$ to some $f(\mathbf{\Gamma}, t)$, assumed to differ from the $t = 0$ equilibrium distribution by a small perturbation $\Delta f(\mathbf{\Gamma}, t) = f(\mathbf{\Gamma}, t) - f_c(\mathbf{\Gamma})$, which in turn can be computed performing a Taylor expansion of the Liouville equation of motion governing the time evolution of $f(\mathbf{\Gamma}, t)$. The response of the system to the external field can be assessed by monitoring the average response of any observable $B(\mathbf{\Gamma}, t)$. The final result is [66]

$$\langle B(t) \rangle - \langle B(0) \rangle = -\int_0^t ds \chi_{BJ}(t-s) F_{\text{ext}}(s), \tag{1.6}$$

where $\chi_{BJ} = \beta \langle B(t) J(0) \rangle$ is the linear susceptibility corresponding to the *equilibrium* time correlation function of B and the dissipative flux J, and the expression is valid in the limit of small F_{ext}. The dissipative flux J is related to the rate of change of the internal energy once the external field is switched on, and it is defined in the following equation

$$\frac{dH_0}{dt} = \sum_{i=1}^{N} \left[-\frac{\mathbf{D}_i \cdot \mathbf{p}_i}{m} + \mathbf{C}_i \cdot \mathbf{F}_i \right] F_{\text{ext}}(t) = -J(\mathbf{\Gamma}) F_{\text{ext}}(t). \tag{1.7}$$

As an example one may consider a Brownian particle (say particle 1) of mass $M_1 \gg m_i$ driven at constant velocity $v_{\text{ext}}\hat{i}$ along x. In this case $\mathbf{D}_i = 0$, $\mathbf{C}_i F_{\text{ext}}(t) = \delta_{i,1} v_{\text{ext}}\hat{i}$, and the average force acting on the particle is given by

$$\lim_{v_{\text{ext}} \to 0} \frac{\langle F_1^x(t) \rangle}{v_{\text{ext}}} = -\beta \int_0^t ds \langle F_1^x(s) F_1^x(0) \rangle. \tag{1.8}$$

Assuming that the long time limit of the integral of the force auto-correlation function is finite [1],

---

[1]Care must be taken when dealing with the statistical treatment of the motion of a single heavy Brownian particle immersed in a solvent of much lighter particles. The brief discussion presented in the section is only aimed at giving a sketch of the way friction can be computed in linear response theory, rather than a mathematically firm procedure for this specific case. An accurate analysis of the problem is found in Ref. [67], which in the end
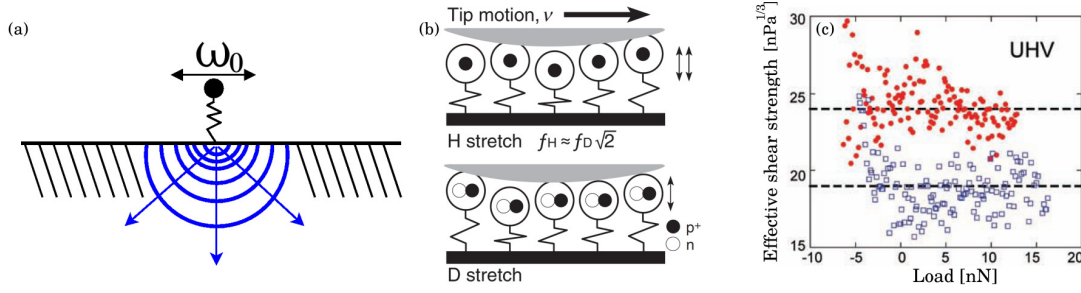
Figure 1.3: (a) An adsorbate molecule vibrating at frequency ω_0 dissipates energy by exciting bulk and surface phonons within the substrate. (b) A tip sliding at velocity v over a hydrogen- (C-H) or deuterium-terminated (C-D) diamond surface. The resonance frequency f_H of hydrogen adsorbates is roughly $\sqrt{2}$ times larger than that of deuterium, f_D. Black filled and open circles indicates protons, $p+$, and neutrons, n. (c) The effective shear strength measured in UHV conditions for C-H (red dots) and C-D (blue squares) demonstrates the increase in friction in the case of lighter adsorbates. (Adapted from Ref. [59])

Eq. (1.8) allows to calculate the damping coefficient $\eta = \lim_{t\to\infty, v_{\text{ext}}\to 0}\langle F_1^x(t)\rangle/v_{\text{ext}}$ starting from equilibrium properties of the system. The above treatment naturally applies to liquid systems. Generalizations to solid/liquid interfaces, of higher interest in tribology, yield similar results. In particular the viscous drag exerted by a confined fluid flowing at small constant velocity in contact with a wall of area A can be computed in linear response from the equilibrium auto-correlation function of the total force acting on the wall [68, 69]

$$\eta = \lim_{t\to\infty} \frac{1}{2Ak_BT} \int_0^t \mathrm{d}t' \langle \mathbf{F}(t') \cdot \mathbf{F}(0)\rangle. \tag{1.9}$$

This gives a prescription to calculate the friction coefficient, which can be readily applied in MD simulations, provided the integral of the auto-correlation function reaches a plateau within the –always finite– simulation time. In a recent work, Tocci and coworkers [65] applied Eq. (1.9) to ab-initio MD simulations of water in contact either with graphene or hexagonal boron nitride (hBN). They found an increase by a factor ≈ 3 in the friction force exerted on hBN, as shown in Fig. 1.2, which is due to a larger effective corrugation of the potential landscape on hBN felt by water molecules with respect to that on graphene.

A general statistical treatment of solid/solid sliding interfaces of the kind commonly encountered in nanotribology experiments is impossible, nevertheless theoretical models can be formulated case by case. Consider for example adsorbate atoms vibrating over a crystalline surface, as depicted in Fig. 1.3a. These frustrated translational modes are of fundamental interest in dynamical processes such as diffusion, surface reactions, and, ultimately, sliding friction. One would like to characterize how the oscillations of the adsorbates are damped due to coupling with the substrate. When the resonance frequency of the adsorbate is small, within the linear region of the bulk phonon spectrum, and when electronic excitations are negligible, the damping of the oscillation can be accurately calculated using the continuum elastic model [70], which assumes a linear relation between the surface stress and the displacement field in the bulk. If the adsorbate is described by a harmonic oscillator of frequency ω_0, coupling to the elastic semi-infinite substrate leads to a renormalization of the resonance frequency $\omega_0 \to \tilde\omega_0$ and introduces a damping

---

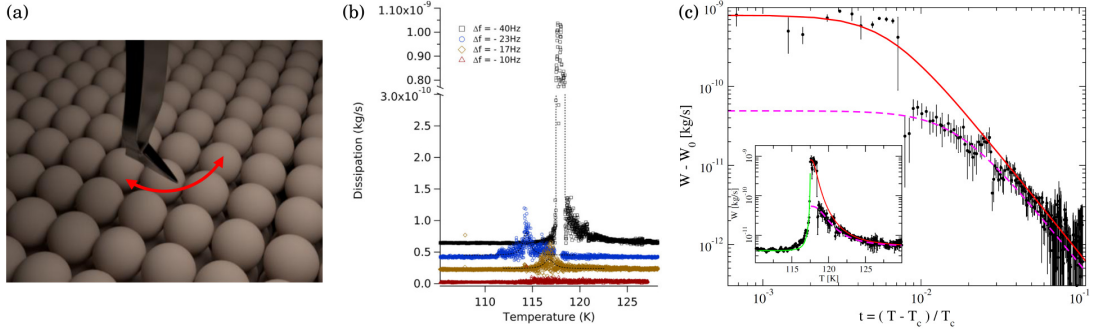yields a similar formula for the damping coefficient.

Figure 1.4: (a) Schematics of the experiment by Kisiel and coworkers [71]. An AFM tip in pendulum-mode slowly oscillating several nanometers above a $SrTiO_3$ sample. (b) Experimental dissipation versus temperature curves at increasing tip-substrate distances (from top to bottom), as measured by the shift Δf of the cantilever resonance frequency. At small distances the curves display a clear peak in the range $T = 114 - 118$ K (data are taken at different substrate spots), corresponding to the critical region of the antiferrodistortive structural phase transition of $SrTiO_3$. (c) Experimental dissipation $W - W_0$ above T_c as a function of temperature (black dots). The inset reports the same data in a linear temperature scale, including values below T_c. Lines are theoretical fit according to linear response theory, Eq. (1.12). Details on different fitting procedures are discussed in Ref. [71]. (Adapted from Ref. [71])

coefficient, which, apart from a factor of order unity, is given by [70]

$$\eta = \frac{m\tilde{\omega}_0^4}{2\pi\rho c_T^3}, \tag{1.10}$$

where ρ, c_T, m are respectively the density of the substrate, the transverse bulk sound velocity and the adsorbate mass. A simple argument can be used to obtain Eq. (1.10). Assuming that the adsorbate carries a total energy E and that collisions with the substrate are elastic, the energy transmitted to the substrate is given approximately by $E(m/m_s)$, where m_s is an effective substrate mass involved in the collision. During a characteristic collision time $\tau \sim 1/\tilde{\omega}_0$, the resulting displacement field extends a distance $c_T\tau = c_T/\tilde{\omega}_0$ inside the substrate, and the effective mass is estimated as $m_s \sim \rho(c_T/\tilde{\omega}_0)^3$. Assuming that collisions occur at a rate $\nu = \tilde{\omega}_0/2\pi$, the net rate of energy transfer can be written as $dE/dt \approx -\nu(m/m_s)E$, which gives an exponential decrease characterized by a damping constant $(\tilde{\omega}_0/2\pi)(m/m_s) = m\tilde{\omega}_0^4/(2\pi\rho c_T^3)$. An interesting consequence of Eq. (1.10) is the overall dependency of the damping coefficient η on the adsorbate mass m. Since the resonance frequency $\omega_0 \sim m^{-1/2}$ one has $\eta \propto 1/m$. Following the argument given above, this trend reflects the increase in the net rate of energy dissipation allowed by the higher vibration frequency of light adsorbates with respect to heavy ones. Cannara and coworkers [59] were able to observe the isotopic shifting of the friction coefficient by performing sliding experiments with a tip moving over hydrogen- and deuterium-terminated diamond(001) surfaces, as shown in Fig. 1.3b,c.

Numerical investigations [72] suggested that the critical fluctuations of second order structural transitions should leave a footprint in the frictional dissipation of external probes. In a recent experiment, the mechanical dissipation of an AFM silicon tip hovering in non-contact mode over a $SrTiO_3$ sample was found to show a sharp peak at a temperature T just above 100 K (see Fig. 1.4a,b), a clear signature of the well known antiferrodistortive structural phase

transition of this material [73]. Non-contact mode AFM experiments operate at small oscillation frequencies, $f \sim 11$ kHz, and at large tip-sample distances, $z \sim 2$-10 nm, where the tip-substrate interaction is dominated by weak dispersive van der Waals forces. This regime justifies a perturbative theoretical approach. In particular, the dissipated energy per cycle W is, in linear response, proportional to the imaginary part of the bulk lattice susceptibility [71]

$$W(\omega, T) = W_0 + \alpha k_B T \mathrm{Im}\chi(\omega, T), \tag{1.11}$$

where W_0 is the internal dissipation of the free cantilever, α is a distance dependent constant, and $\chi(\omega, T)$ is an appropriate momentum average of the lattice susceptibility $\chi(\mathbf{q}, \omega, T)$. Using a phenomenological ansatz [74] for $\chi(\omega, T)$ near the critical point, the following expression is obtained for the overall critical form of the low frequency AFM dissipation [71]:

$$W - W_0 = \frac{U}{1 + Vt^{2\gamma}}, \tag{1.12}$$

where $t = (T - T_c)/T_c$, U and V are positive constants used as fitting parameters, and $\gamma \approx 1.24$. Figure 1.4c demonstrates the good agreement between experimental data and theoretical fit to Eq. (1.12).

The friction force observed in QCM experiments of incommensurate rare gas monolayers usually displays a viscous friction law. Also in this case a perturbative approach can be used to describe the average energy dissipated during sliding [75]. The power dissipated under steady state sliding at velocity $\mathbf{v}$ is given by $P = \mathbf{v} \cdot \mathbf{F}$, where $\mathbf{F}$ is the force applied by the substrate. In linear response one assumes that there is a simple relation $\mathbf{u}(\mathbf{q}, \omega) = \chi(\mathbf{q}, \omega)\mathbf{F}(\mathbf{q}, \omega)$ between the adsorbate displacement $\mathbf{u}$ and the force, for given wave vector and frequency $(\mathbf{q}, \omega)$. For a periodic substrate potential of triangular symmetry $V(\mathbf{r}) \sim U \sum_{i=1}^{3} \cos(\mathbf{G}_i \cdot \mathbf{r})$, the force has a frequency $\omega = \mathbf{v} \cdot \mathbf{G}_i$. The average power dissipated is easily computed, giving

$$P = \sum_{\mathbf{q}} -i\omega\chi(\mathbf{q}, \omega)|\mathbf{F}(\mathbf{q}, \omega)|^2 \propto U^2. \tag{1.13}$$

Indeed a quadratic increase of dissipation as a function of the substrate corrugation strength U has been observed in a number of experiments [76, 77] and MD simulations [75, 78] of nano-sliders.

Viscous dissipation is encountered in lubricated systems at small sliding speeds, and more generally in weakly interacting incommensurate solid surfaces. Actually, many experimental conditions fall within this category. These situations allow for perturbative theoretical approaches, where the ensuing tribological behaviours are understood based on few global properties of the interface. In liquid/solid interfaces linear response theory is not applicable at high flow rate, when turbulence sets in. Dry and even lubricated solid/solid sliding more generally involve violent events, resulting in highly non-linear responses of the slider to external solicitations. The formulation of a general theoretical framework able to account for these cases is still today the biggest challenge in tribology.

1.3 Stick-slip sliding

Stick-slip motion is a paradigmatic behaviour of any sliding interface. It corresponds to a discontinuous advancement made of subsequent jumps separated by intervals of time in which the slider remains substantially stuck. Stick-slip can be regular (periodic) or irregular (chaotic), and
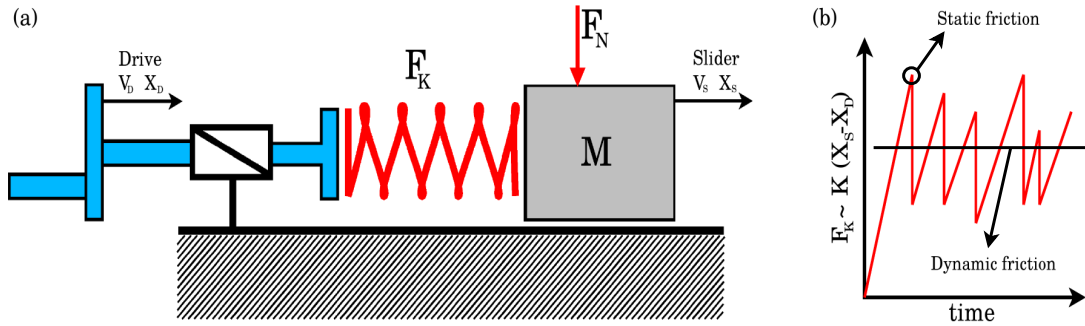
Figure 1.5: (a) Schematics of a macroscopic frictional experiment. A spring of stiffness K is loaded at a constant rate by a driving apparatus at position X_D, moving at constant velocity V_D. The spring pushes a slider of mass M, position X_S, and velocity V_S, on which a normal force F_N is applied. The friction force at the interface is measured by the elastic force $F_K \sim K(X_D - X_{rms})$ of the spring. (b) During stick-slip, a simple input of constant loading velocity V_D results in a complex response of the interface which moves in an intermittent way, which is evinced from the sawtooth behaviour of the frictional force F_K. The first peak in the friction trace measures the static friction force needed for the onset of sliding. Dynamic friction is given by the average value of F_K.

it is encountered in systems at any length scale, from the motion of tectonic plates, down to the sliding of an AFM tip. In frictional sliding it represents the main source of dissipation, wear, and components failure. Figure 1.5a shows a schematic set up for a macroscopic sliding experiment: a slider of mass M, subject to a normal force F_N is pushed by a spring of stiffness K, which is loaded at constant rate by a driving support moving at velocity V_D. The spring elongation measures the frictional force acting at the slider-substrate interface. Concerning the properties of the interface, a sufficient condition for the appearance of stick-slip is that the static friction force must be larger than the dynamic friction force. As the driving apparatus starts its motion, the spring accumulates elastic energy until the static friction force is overcome, triggering the onset of global sliding. If dynamic friction is lower than static friction, the slider will rapidly accelerate to a velocity $V_S > V_D$ and the spring will extend back to – or, in systems with large inertial effects, beyond – its free length. At this point the slider will decelerate to a stop, and the whole process will repeat as long as the driving apparatus is maintained in motion. A schematic experimental outcome is depicted in Fig. 1.5b, showing the typical sawtooth behaviour of the friction trace. This analysis suggests a simple way to get rid of stick-slip, that is reducing static friction at the interface, as it is done in everyday life when oiling the hinges of a creaking door. Stick-slip motion also depends on external conditions: inertia of the slider, normal force, and spring stiffness. The dynamical behaviour of an interface is usually characterized in terms of a "phase diagram" in the space of the external parameters (M, V_D, K, F_K), identifying transitions between different sliding regimes. Useful rules-of-thumb of general validity in macroscopic and microscopic systems are that a transition from the highly dissipative stick-slip motion to a more gentle smooth sliding (where $V_S \approx V_D$) occurs by increasing the driving velocity V_D, or the stiffness K of the system, or by decreasing the normal load F_N.

In an effort to understand how macroscopic and microscopic features act together to determine the interface motion, several models have been developed [79] that take into account various surface properties, such as the effects of molecular or asperities size, sliding velocity, and
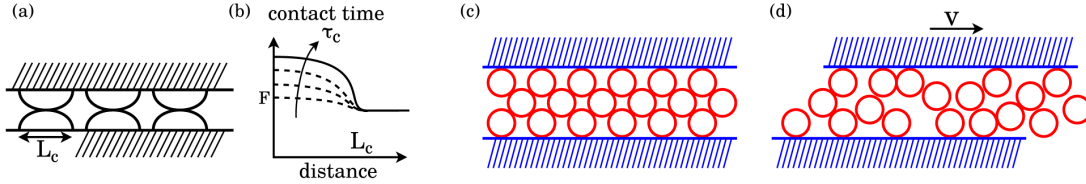
Figure 1.6: (a) Distance dependent model of stick-slip between dry surfaces. The interface is modeled by a sequence of asperities forming junctions of characteristic size L_c. (b) The adhesive static friction force between touching asperities is assumed to increase with time, reaching saturation after a characteristic time τ_c. At small enough loading velocities the friction force decreases after the interface creeps a distance equal to L_c, as the old junctions are broken. Sliding then takes place at a lower kinetic friction value, the interface reaches a stop, and a new stick-slip cycle begins as adhesion builds up in the sticking transient. (c) A solidified, molecularly thin liquid film confined in a nanoscopic interface under high pressure. (d) Slipping of the interface is induced by shearing one of the two surfaces with velocity v. The kinetic friction in the sliding molten phase is usually lower than the static friction value of the solid-like configuration. Stick-slip motion in lubricated systems corresponds to the periodic switching between the sticking solid phase (s) and the sliding liquid phase (d).

characteristic relaxation times. Distance dependent models were proposed in the 1950s in order to explain dry friction between solid bodies. They are based on the assumption that surfaces of macroscopic bodies adhere to each other at touching asperities which are describe by a characteristic size L_c. During shearing the interface must first creep over a distance L_c in order to win the "adhesive", static friction force of the asperity-asperity junctions. The strength of the adhesion between asperities is assumed to be time dependent, reaching saturation in a characteristic time τ_c, so that even though new junctions are formed as soon as the old ones are broken, the shear strength of the newly born ones is reduced with respect to the initial value. The interface will then continue to slide but with a lower kinetic friction force. As discussed in the previous paragraph a sufficient condition for stick slip motion is a lower dynamic friction with respect to static friction. The dynamics of the interface is strongly dependent on the loading conditions. As the surfaces slide past each other a distance equal to L_c, the friction force drops (see Fig. 1.6). In constant loading rate experiments (see Fig. 1.5) regular stick slip occurs at small enough driving velocities V_D and stiffness K, where, after each slip, adhesion does have time to build up. On the other hand stick-slip disappears at high V_D, K, when the junctions are severed at a high rate, preventing adhesion. In paper-on-paper experiments [10], for example, the measured stick-slip amplitude $\Delta F = (F_s - F_k)$ decreases rapidly with velocity and vanishes at a critical value $V_c \sim e^{-CK/M}$ in the creep dominated regime (high K, small V_D) and at $V_c \sim K^{-2}$ in the inertial regime (high V_D, low K). This kind of models have been applied to study a variety of dry solid-solid interfaces, including rock-on-rock sliding of interest in earthquake dynamics [80]. Notably, similar models are able to describe also the motion of molecularly smooth surfaces, for example in boundary lubricated friction with surface polymers, where the adhesive forces are expected to increase with time. In this case τ_c is given by the characteristic molecular entanglement time, while L_c is the chain-chain entanglement length.

Stick-slip motion is not restricted to dry frictional sliding, but it also occur in presence of thin liquid films at the interface. Stick-slip sliding is associated in this case to successive melting-freezing cycles induced by the applied shear force, as shown in Fig. 1.6c,d. Under high pressure confined molecularly thin films solidify, and are able to support high values of shear
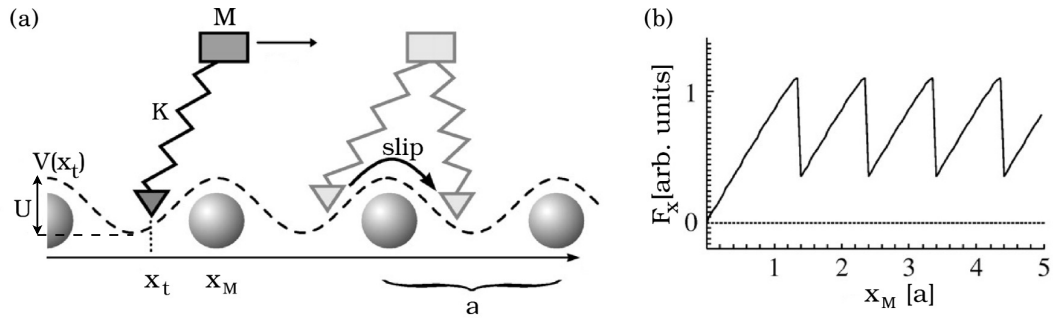
Figure 1.7: (a) The Prandtl-Tomlinson model. A mass M is connected to a spring of constant K and is dragged at constant velocity v while interacting with a sinusoidal periodic potential $V(x)$ of amplitude U and periodicity a, mimicking the sliding of an AFM tip over a one dimensional periodic arrangements of atoms. (b) For sufficiently soft spring or strong substrate interaction strength U, the trajectory of the mass displays stick-slip motion, where the particle remains stuck in one minimum of the periodic potential until the increasing elastic force F_x induces a fast slip towards an adjacent minimum.

stress. Once the external force exceeds the static friction threshold, the surface slides with a lower kinetic friction as the liquid turns in the molten state. If the shear rate is sufficiently high the film is not able to solidify and stick-slip motion is replaced by smooth sliding. The simplest phenomenological model able to describe this situation assumes the dynamic friction F_d to be linearly dependent on the sliding velocity v, $F_d(v) = Av$, while static friction is assumed to be constant, $F_s = B$. Stick-slip is observed at low shear rates, as long as $F_d(v)$ stays below the static friction threshold, and disappears as soon as $Av > F_s$.

In surface roughness models, adhesion is neglected, and sliding is simply assumed to be impeded any time two asperities collide. When two asperities touch, the ensuing force experienced by the slider will generally have both a component normal to the interface, and a component parallel to the interface, and opposing the slider motion. In order to advance, the slider must first climb up the substrate asperity – corresponding to sticking – before slipping in an adjacent valley. The regularity of stick-slip motion is directly correlated with the regularity of the surface roughness. The controlling factors of this type of stick-slip are the surface topology, i.e., the periodicity and amplitude of the protrusions, and the elastic and inertial properties of the slider, which determine the rate of slip. Stiffer materials, corresponding to high K, will generally show shorter slip at a high rate because of the shorter "effective-spring" recoil to elastic equilibrium. This also allows sticking to smaller asperities, resulting in a richer stick-slip spectrum. In the limiting case of infinite stiffness, plastic deformations disappear, and the frictional trace approaches a contour-trace of the surface topology, with a sensitivity limited by the characteristic size of the protrusions. Surface roughness induced stick-slip is observed in the sliding of macroscopic rough surfaces as well as in AFM experiments. In the latter case the tip simulates a single nanoscopic asperity, and stick-slip results in a periodic trace with a spacing set by the lattice periodicity of the substrate. The simplest model to describe the sliding of an atomically sharp tip over a crystalline surface is the Prandtl-Tomlinson [81] (PT) model, shown in Fig. 1.7a. The PT model consists of a mass M connected to a spring of stiffness K, moving at constant velocity v, and subject to a sinusoidal periodic potential of amplitude U. The dynamical behaviour at fixed sliding speed is determined by the ratio $\eta = U/K$, and by a phenomenological viscous term which
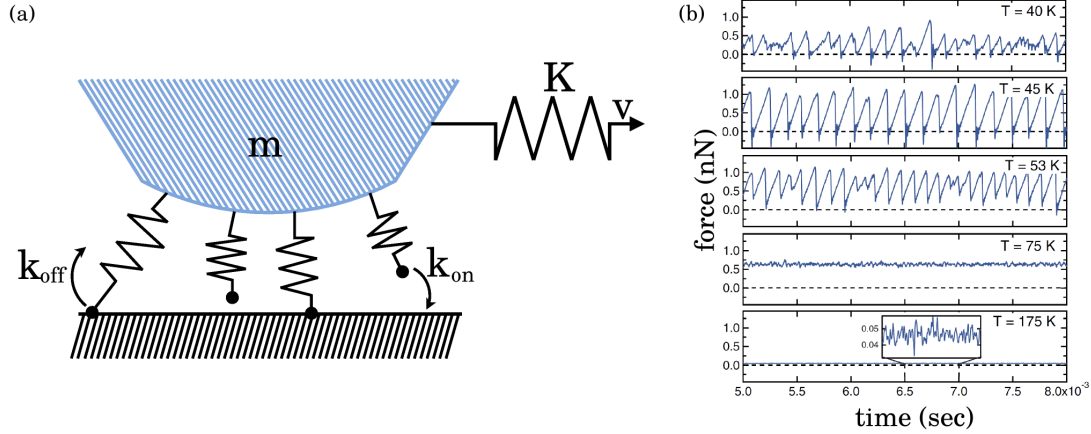
Figure 1.8: (a) Model to simulate multiple contacts between a slider of mass m and a substrate. The slider is dragged by a spring of stiffness K, moving at velocity v. Junctions representing chemical bonds, interlocking asperities, or capillary bridges, are replaced by springs. Each contact is characterized by temperature dependent detachment rate k_{off} and formation rate k_{on}. (b) Results from numerical simulations of a multicontact model for the sliding of an amorphous tip. (Adapted from Ref. [85]). Increasing temperature, the friction versus time curves show a transition from an highly dissipative periodic sequential stick-slip behavior at low temperatures, to the stochastic smooth-sliding behavior of simultaneous multiple bonds formation and breaking processes at higher temperatures.

accounts for dissipation, mimicking the coupling to an external bath. For large enough values of η the PT model dynamics embodies the mechanical instability leading to stick-slip motion (see Fig. 1.7b). Despite its simplicity, numerical simulations of the PT model have been used to explain a number of friction force microscopy results [82–84].

During sticking the interface is not in equilibrium and several processes occur, from *slow* plastic relaxations, to *fast* propagation of local rupture fronts [86, 87]. Even slow macroscopic creep motion usually underlies fast local, microscopic rupture and relaxation processes that in general cannot be described as the sum of single asperities response, but are influenced by temporal and spatial correlations mediated by elastic interactions across the whole ensemble of contacts that form the interface [88, 89]. These effects are particularly relevant in mesoscopic systems, where local junctions are formed by dry asperities, capillary bridges, or small patches of solidified lubricants. Simulations [90] revealed that even in AFM experiments the tip may form a number of atomic contacts with the crystalline substrate. Phenomenological mechanokinetic models have been proposed to describe these multicontact interfaces. Basically each contact is modeled by a spring connecting the slider to the substrate, as shown in Fig. 1.8a. As the slider moves, each spring elongates, increasing the friction force opposing the slider motion, until a rupture point is reached, the bond is removed, and a new, relaxed one is formed. The physical nature of the contacts depends on the system under investigation. For atomic-scale contacts, capillary bridges and patches of solidified lubricants, the formation and rupture of contacts are thermally activated, and lead to a complex dependence of friction on slider velocity and temperature [85, 91–94]. In dry asperity contacts temperature plays a minor role and threshold rupture forces are taken from probability distributions related to the structure of the interface. At the nanoscale, the rates of bond formation and rupture, k_{on} and k_{off}, are determined by the corresponding activation energy barriers ΔE_{on}, and ΔE_{off}. In particular ΔE_{off} is force

dependent and decreases with increasing stretching of the bond/spring. One can identify four competing rates in the system: (i) the rate of spontaneous bond rupture k_{off}^0, (ii) the rate k_{on} of bond formation, (iii) the rate Kv/f_s of forced unbinding, (iv) the rate $\omega_m = max(K/\gamma m, \sqrt{K/m})$ of the pulling force relaxation. Here f_s is the average contact rupture force, K is the stiffness of the pulling spring, m is the slider mass, and γ is the dissipation constant. Depending on the hierarchy between the different rates, different sliding regimes are observed. Smooth sliding is observed (i) at high velocities and low temperatures, where forced unbinding dominates over bond formation $Kv/f_s \gg k_{on}$, (ii) at high temperatures, where spontaneous, thermally activated bond rupture dominates, $k_{off} \gg> Kv/f_s, k_{on}$, (iii) at very small velocities, corresponding to a quasi-stationary regime where forced unbinding rarely occurs and all thermally activated processes are basically at equilibrium, resulting in a constant friction force acting on the slider. At intermediate velocities and temperatures, k_{on} increases bond formation during sliding, and stick-slip emerges, characterized by a cooperative behaviour of contacts. Transition from periodic to irregular stick-slip occurs in this regime as k_{on} becomes greater than ω_m, at which point the slider may stop before the pulling spring is completely relaxed (see Fig. 1.8b). Simulations show that the friction force peaks at temperatures where $k_{on} \sim \omega_m$, and then decreases, first by thermal reduction of contact rupture forces, and then, going in the smooth sliding regime, because spontaneous unbinding processes dominate the interface dynamics.

From a fundamental point of view the variety of conditions under which intermittent motion is observed makes it difficult to formulate a general theory. Many mechanical and physical mechanisms remain unclear, and are hardly accessible experimentally. As a consequence most theoretical models must rely on phenomenological assumptions, and usually apply only to specific experimental conditions. For these reasons, any real system in which stick-slip and the transition to smooth sliding can be characterized and modeled down to fine details would represent an invaluable tool to get the theoretical insights required in order to achieve a better frictional control in sliding (nano)machineries.

1.4   Structural lubricity

The great progress of nanotechnologies of the last decades has enabled increasing insight into the microscopic nature of friction [11, 96, 97]. In particular, sliding between contacting crystalline surfaces has become of higher interest after the manipulation of nanoscale-sized objects revealed how the atomistic features of an interface may play the ultimate role in determining its tribological properties. The most evident frictional signature of the periodic nature of a crystalline plane is the observation of atomic stick-slip, where the period of the stick-slip trace equals the lattice spacing of the substrate. This is routinely probed in AFM experiments [98], and easily explained with simple PT-like models. When studying the tribological properties of extended, atomically flat surfaces, crystalline order is responsible for the appearance of more exotic phenomena. In dry frictional systems static and dynamic friction are found to be strongly dependent on the interface commensuration. One of the most intriguing effect is the possibility to eliminate the atomic instabilities responsible for the highly dissipative stick-slip sliding by changing the geometry of the interface. This kind of structural lubricity is expected to occur in hard incommensurate interfaces. In this case frictional forces arise mainly due to interlocking between atomic asperities. In incommensurate systems one expects that there should be the same amount of asperities pushing the slider in any directions within the contact plane, envisaging the possibility of perfect annihilation of lateral forces, and thus of friction.

The one dimensional Frenkel Kontorova (FK) model [99] provides a general theoretical frame-
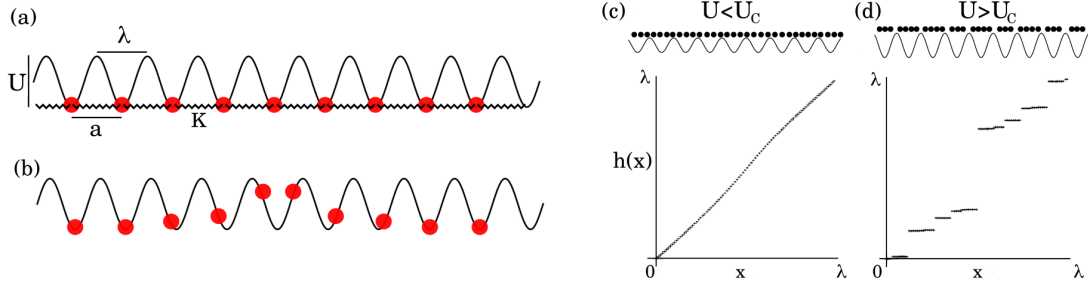
Figure 1.9: (a) The Frenkel-Kontorova model: an infinite chain of masses of equilibrium spacing a are connected by springs of constant K and are subject to a sinusoidal potential of strength U and periodicity λ. The model mimics the interface between a soft crystalline slider and a hard non-deformable periodic substrate. The ground state of a perfectly commensurate interface $(a = \lambda)$ is realized by putting each mass in one potential minima. (b) Introducing one extra particle results in the creation of a topological defect or kink. Kinks are responsible for mass and energy transport along the chain as the barrier for the motion of a defect is much lower than the substrate strength U. (c-d) Increasing the substrate potential amplitude U the ground state of incommensurate chains undergoes a transition by breaking-of-analyticity, signaled by the change in behaviour of the periodic part of the hull function $h(x)$, which maps the positions of the particles of the undistorted chain, at $U = 0$, to the final positions in the ground state at $U \neq 0$. (c) Below the transition $h(x)$ is analytic, while for $U > U_c$ (d) it increases only via discontinuities. (Adapted from Ref. [95])

work for the study of dry crystalline interfaces, and it is sketched in Fig.1.9a. The slider is described by an infinite linear chain of masses with spacing a, coupled by springs of stiffness K. The harmonic crystal interacts with a sinusoidal potential $V(x) = -U/2(1 + \cos(2\pi x/\lambda))$ of amplitude U and period λ, mimicking a hard, non-deformable substrate. Commensurate chains are characterized by a rational value of $\rho = \lambda/a = p/q$, with integers p, q. In the simplest case $\rho = 1$, the ground state configuration is obtained by putting each particle in one minimum of the substrate periodic potential. The chain dynamics is usually studied by applying an uniform force to all the particles. At zero temperature and for perfect commensuration $\rho = 1$, each particle must overcome the full barrier set by U before reaching an adjacent well, and the normalized static friction force equals the maximum (single particle) value $F_{s1} = U\pi/\lambda$. The tribological properties of the FK model are strictly connected with topological defects, excitations corresponding to local compressions (*kinks*) or dilations (*antikinks*) of the chain. Starting from a commensurate chain, a topological defect is created by adding (removing) one extra atom: the resulting configuration after energy minimization corresponds to one kink (antikink) in the chain, as shown in Fig. 1.9b. The importance of topological defects stems from the fact that they can move easily along the chain. The potential barrier for the motion of a kink is always much smaller than the substrate potential amplitude U. In commensurate conditions sliding is therefore generally realized first by – thermal – generation of one defect, whose propagation along the chain triggers the creation of several others [100], eventually leading to global sliding. Less trivial commensurate geometries correspond to $\rho = p/q \neq 1$, in these cases the ground state is described by an elementary cell consisting of p atoms, and the chain generally shows lower friction forces than the $\rho = 1$ case. The limit of large p, q approximates an incommensurate chain, where friction can vanish, as discussed below.

Irrational values of ρ define incommensurate configurations, characterized by a competition
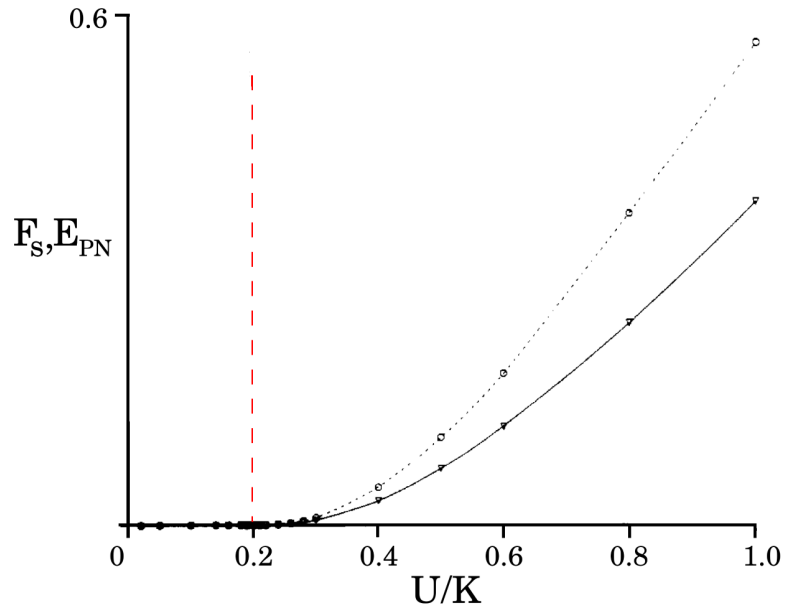
Figure 1.10: The static friction force F_s (dotted line) and the Peierls-Nabarro potential barrier E_{PN} (continuous line) in the infinite golden-mean incommensurate Frenkel-Kontorova model, $\rho = \lambda/a = (1 + \sqrt{5})/2$. The red dashed line indicates the critical point of the transition by breaking-of-analyticity. Both F_s, and E_{PN} are zero below the transition and then grow continuously as $\sim (U/U_c - 1)^\nu$, with $2.8 < \nu < 3$. (Adapted from Ref. [95]).

between the two length-scales a, λ. Indeed, the inter-atomic spring interaction favors an equidistant mass separation a, while the substrate potential tends to force the particles into a periodic configuration of spacing λ. Exact analytical results show that the ground state of incommensurate chains can be described by a function $f_H(x)$ (the hull function), mapping the position $x_l^0 = la$ of the l-th particle in the regularly spaced, undistorted chain, to the corresponding position x_l^{GS} in the ground state, which differs from x_l^0 because of the modulations induced by the periodic substrate. In particular x_l^{GS} is given by [95]:

$$x_l^{GS} = f_H(la + \alpha) = la + \alpha + h(la + \alpha) \tag{1.14}$$

where α is an arbitrary phase, and $h(x)$ is a periodic function with the same period λ as the substrate potential $V(x)$. The relative strength $\eta = U/K$ of the external potential with respect to the internal elastic chain stiffness plays the key role in determining the tribological properties of the chain. The structure of incommensurate chains roughly corresponds to a sequence of nearly commensurate domains separated by regions of compressions (if $\rho < 1$), or dilations (if $\rho > 1$), whose width decreases with increasing η. In analogy to the topological excitations of commensurate structures, these "preformed" topological defects, naturally present in incommensurate configurations, display an enhanced mobility compared to the nearly commensurate regions. In 1983 Aubry [101] demonstrated that the ground state of the incommensurate FK model undergoes a phase transition occurring – at fixed spring stiffness K – increasing the potential strength above a critical threshold U_c. The transition is signaled by the behaviour of the hull function, which is analytic below U_c, and becomes a sum of step functions above the critical point (see Fig. 1.9c,d). Below the critical point a continuous set of ground states exists that can be reached

adiabatically by plastic deformations of the chain at no energy cost, static friction is zero, and sliding can be achieved ideally by applying even the smallest external force. Above the transition the solitons become pinned, and static friction becomes finite. One can define different quantities that display a critical behaviour across the Aubry transition [95]. In Fig. 1.10 we report the trend of the static friction force F_s and the Peierls-Nabarro (PN) barrier E_{PN}. The PN barrier is the smallest energy barrier that must be overcome to move continuously the chain on the periodic potential. For $U < U_c$ the advancement of the incommensurate structure is obtained by shifting continuously the phase α of Eq. (1.14). Due to the continuity of the hull function, the motion of each atom is continuous, moreover, since the energy of the whole system is independent of α, the PN barrier is zero, and so it is the static friction force. Above the transition, for $U > U_c$, the incommensurate structure is described by a discontinuous hull function, and the resulting structure is physically interpreted as an array of discommensurations – with respect to some neighbouring commensurate structure – locked to the lattice (see Fig. 1.9c). Thus, when the structure is translated by shifting the phase of the hull function, the atoms have to cross each discontinuity, corresponding to move all the locked discommensurations, which requires to pass an energy barrier E_{PN}, eventually resulting in a finite static friction force F_s. A characteristic signature of the Aubry transition is obtained by studying the so-called disorder parameter Ψ [99], corresponding to the amplitude of the largest gap in the hull function. As shown schematically in Fig. 1.9c,d below the critical value, continuity of the hull function implies that the particles sample all possible values of the periodic potential, in particular they can be found arbitrarily close to the maxima of the substrate. For $U > U_c$, maxima are strictly avoided over a region of width Ψ, which is measured by the largest central gap of $h(x)$. All the critical quantities are zero below U_c, and grow continuously as $\sim (U/U_c - 1)^\nu$ above the transition, with characteristic exponents obeying simple scaling laws [95]. It is important to note that the critical value U_c is an erratic function of ρ, being maximum for the "most irrational", golden mean value $\rho = (1+\sqrt{5})/2$.

The above analysis of the FK model demonstrates the possibility to attain zero static friction in infinite incommensurate systems. In the limit of very small sliding velocities (or driving forces) it also indicates that dissipationless sliding is achievable, below the Aubry transition, as the chain can move continuously through the adiabatically connected ground states. The problem whether sliding without dissipation would occur or not at arbitrary sliding speeds has been addressed theoretically by Shinjo [102], using the same one dimensional FK model, and studying how the center-of-mass kinetic energy decays in time, given an initial momentum P_0 of the chain, equally distributed to all the atoms. Indeed, they found and characterized a frictionless sliding state, which they called *superlubric*, where the kinetic energy of the chain is periodically and reversibly transferred to excitations of the internal modes of the chain, and then back into translational kinetic energy. In this regime the chain would slide indefinitely. Interestingly they found these recurrence phenomena to occur, for large enough values of P_0, at any values of the substrate potential amplitude, even above the critical threshold U_c signaling the Aubry transition of the static chain. Similar results were also found in two dimensional models [103]. Successive detailed investigations [104] showed that such superlubric state is in fact only temporary. The onset of friction occurs in two steps: the resonant coupling of the center-of-mass to modes with the wave vector $q = 2\pi/\rho\lambda$ leads to long wave-length oscillations, these in turn drive a complex parametric resonance involving several resonant modes, which eventually absorb all the kinetic energy in an irreversible way. The superlubric regime, where recurrence phenomena occur, is one in which coupling to these resonant modes is very weak and the chain slides with negligible kinetic friction for relatively long times.

The term superlubricity has been criticized since it suggests that the transition to zero friction
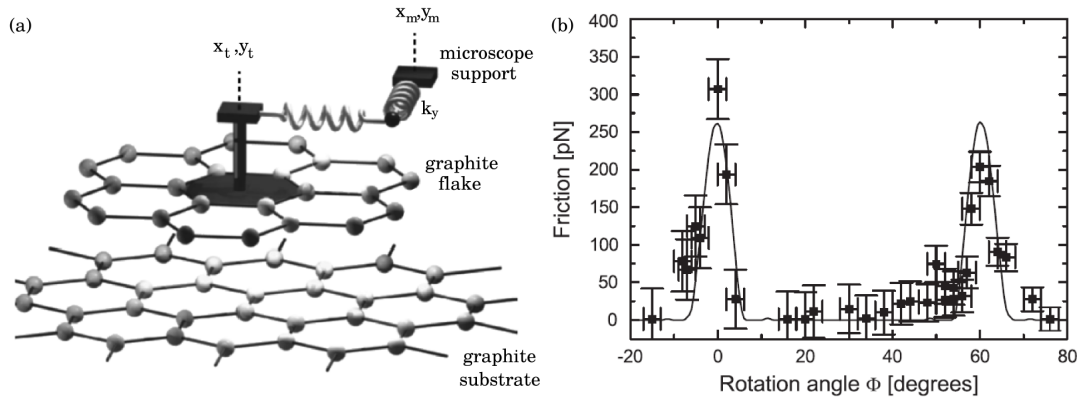
Figure 1.11: (a) A modified PT-model used to simulate superlubricity of a graphite flake sliding over graphite. (b) Static friction force as a function of the flake relative angular orientation Φ with the substrate. Points show the experimental data. The continuous line corresponds to numerical results obtained from the generalized PT-model. (Adapted from Ref. [111])

can be compared to superfluidity or superconductivity. Even if there is some correlated motion of the atoms, no pair formation occurs as in the case of superfluids or superconductors. Moreover, as discussed in the previous paragraph, incommensurability only cancels one channel of dissipation, which comes from the mechanical instabilities leading to stick-slip motion. Other processes such as the emission of phonons are always present, and therefore kinetic friction is always finite. In the case of superconductivity, electric resistance does become zero, so that the prefix "super" is not appropriate in this case. However, the term superlubricity is quite appropriate from a tribological standpoint in the sense that the prefix is only indicative of the extremely low friction observed in superlubric systems, when compared to the values one obtains in similar but commensurate cases.

Experimentally, the easiest way to induce a transition to the superlubric state is to exploit relative rotations between hard commensurate surfaces having the same lattice symmetry and spacing. Controlling the angle of rotation enables to change the geometry of the interface from aligned and commensurate to misaligned and incommensurate. One then expects to observe a transition from a highly dissipative stick-slip regime, typical of commensurate "atomically-locked" systems, to the smooth sliding regime of incommensurate geometries. Indeed, the first evidences of superlubric sliding were observed in SFA experiments between muscovite mica surfaces [105], and in STM experiments between a crystalline Si tip and a clean W crystalline substrate [106], where a frictional reduction of one order of magnitude was registered by rotating the substrate away from commensuration. Since its discovery, superlubricity has attracted a lot of interest because of its potential practical applications. In particular the properties of solid lubricants are currently object of investigations [107–110] as they represent the only way to reduce friction and wear in cases where the use of liquid lubricants is either impractical or inadequate, as in vacuum, space technology or automotive transport. Lamellar materials such as graphite and metal dichalcogenides seem to be the best candidates. Thanks to their layered structure with weak inter-layer forces, interfacial slipping between different layers allow for easy, low-strength shearing, necessary to achieve persistent low friction sliding and resistance to wear.

In early experiments Martin and coworkers [112] found that, under high vacuum conditions, MoS_2 film coatings can show extremely low friction coefficients. The origin of superlubricity

is due to a friction induced orientation of MoS_2 two dimensional grains parallel to the sliding direction, which then serve as easy-shear basal planes for sliding of superimposed crystallites. High resolution TEM images showed the presence of moiré patterns, indicating the presence of rotational disorder between such crystallites, the ensuing frictional anisotropy of the basal planes has been proposed to be the main cause for the observed superlubricity. More recently, detailed experimental studies of superlubricity were performed adopting a graphite flake attached to an FFM tip sliding over an atomically flat graphite surface [111, 113, 114]. Extremely low friction forces, < 50 pN, have been measured at relative orientations between the flake and the substrate for which the contacting surfaces form an incommensurate interfaces, while for narrow ranges of orientation angles, corresponding to commensurate contacts, stick-slip motion was observed and friction was high, typically 250 pN. These results can be described with the generalized PT model shown in Fig. 1.11a, consisting of a rigid and symmetric graphite flake. Each atom of the slider interacts with the atoms of the substrate graphite surface, and the total interaction potential $U_{\text{flake}}(x_c, y_c, \phi)$ of the flake depends only on its center-of-mass position (x_c, y_c) and on the misfit orientation angle ϕ relative to the substrate lattice. Assuming that the flake orientation ϕ is locked, the frictional force obtained in numerical simulations agrees with the experimental observation, as shown in Fig. 1.11b. Moreover, simulations showed that the width $\Delta\phi$ of the friction force maxima around commensurate orientations depends on the flake diameter D as $\tan(\Delta\phi) = 1/D$, so that $\Delta\phi$ can be used in experiments to estimate the flake size.

Structural lubricity between crystalline interfaces can provide the desired low friction for applications in nano-mechanichal devices. However, experiments demonstrated that the superlubric state may be easily destroyed. Friction experiments between MoS_2 surfaces showed that superlubricity can be achieved only under UHV conditions or in inert ambient [115]. In natural conditions impurity oxygen atoms can replace sulfur at the interface leading to a substantial increase in friction, as they impede the formation of the highly oriented low-shear basal planes. Even in the case of graphite flakes sliding over graphite, superlubricity has been shown to have a finite life, as the torque acting on the slider can easily rotate it into the – energetically favoured – aligned configuration, resulting in stick-slip motion [116]. There are on the other hand promising results showing that extremely robust low values of friction can be attained. Recently, Liu et al. [110] demonstrated the superlubric behaviour of extended sliders (10 μm $\times$10 μm) observing the misfit angle dependent self-retracting behaviour of suspended graphite mesa. Even if hindered by the large size of the flakes, rotations do occur also in this case [117], causing high-friction transients as the flakes rotate through successive crystallographic alignments with the substrate. Nevertheless recent theoretical investigations [117] based on molecular dynamics simulations have suggested clever mechanisms in order to constrain the rotation of square flakes. Substrates made by nanoribbonds with width slightly smaller than the sliding flake diameter can effectively impede rotations of the flake, since exposing suspended parts outside the nanoribbond is energetically unfavoured. Biaxial stretching of the graphitic substrate can also be used to suppress the rotation induced frictional scattering. These observations may serve as a guide to persistent nanoscale superlubricity in graphitic systems, even in ambient condition.

Several fundamental and practical aspects of structural lubricity are still to be understood. In QCM experiments for example, when the adsorbate is incommensurate and hard, solitons exist already in the ground state and their free motion should in principle permit superlubric sliding. However, significant values of the static friction force are usually observed. The origin of pinning in hard incommensurate systems is one open question in nanotribology. Possible explanations have been proposed including pinning defects in the substrates, the presence of third bodies which can lock the slider [118], or finite size effects [119], but the mechanism remains

debated. Another issue regards the possibility to observe the superlubric to pinned transition in genuinely one dimensional incommensurate systems at fixed interface geometry. Experimental signatures of the Aubry transition have not been observed yet due to the difficulty in realizing one dimensional interfaces. From a fundamental point of view even more interesting would be the possibility to investigate this transition in realistic two dimensional interfaces. So far experimental techniques have not allowed detailed study of this particular aspect because the details of the interface are neither directly accessible or controllable. However, these questions may be soon addressed in recently proposed highly tunable experimental set up based on charged particles interacting with laser-generated fields [120, 121], or at the interface between surfaces coated with thin ferromagnetic films [122].

1.5   Molecular dynamics simulations of nanofriction

Linear response theory works well only in weak dissipation cases. Minimalistic and phenomenological models are powerful interpretative tools for understanding and explaining general frictional behaviours. However, they usually allow only for qualitative interpretations of experiments. A more quantitative approach is provided by atomistic molecular dynamics (MD) simulations.

Recent advances in computer science enable simulation and real-time visualization of atomic-scale friction in real systems. MD simulations represent controlled computational experiments, where the dynamics of all atoms is obtained by numerically solving Newtonian equations of motion based on suitable interparticle interaction potentials. Usual approaches rely on the use of large simulation supercells which allow to study different interface geometries, with appropriate boundary conditions, chosen to explore friction, adhesion, and wear. Restricting here to classical molecular dynamics, which neglect the electronic degrees of freedom, once the functional form $E(\{\mathbf{R}_i\})$ of the total energy – depending on all the atomic coordinates $\{\mathbf{R}_i\}$ – is given, the forces $-\nabla_{\mathbf{R}}E$ acting on the atoms can be calculated, and the trajectories of each particle are obtained by solving numerically Newton equations of motion for given initial atomic positions and velocities. Following the time evolution of all the degrees of freedom allow to evaluate instantaneous and average values of all macroscopic quantities of physical interest, such as frictional forces, slider velocity and the dissipated power, giving many insights on the intimate processes going on. Frictional simulations are generally performed out of equilibrium, with external forces acting on the slider. In order to avoid overheating and achieve steady state, the mechanical energy pumped inside the system is eliminated by adopting thermostatting algorithms which must not affect too much the real conservative trajectories of the atoms of the tribologically relevant region of the system [123–125].

The major problems affecting MD simulations are represented on one side by the choice of appropriate force-fields between atoms, and on the other side by the limits on the time- and size-scales effectively explorable given state-of-the-art machines and softwares. In principles, the exact interatomic forces of real materials must be computed solving the quantum mechanical dynamical problem taking into account all the electrons. This is a formidable problem which is treated, at least in an approximate way, in modern ab-initio MD techniques [126]. The computational cost of these approaches allow to simulate small systems and for very short time intervals (typically less than 1 ns), at the end making them not particularly suited for tribological studies. Typical MD simulations are therefore based on empirical force fields fitted to reproduce experimental results obtained in different conditions and for different material combinations. The violent nature of many frictional processes, however, often involve drastic changes in the environment of interfacial atoms, affecting, e.g., their coordination and chemical behaviour,
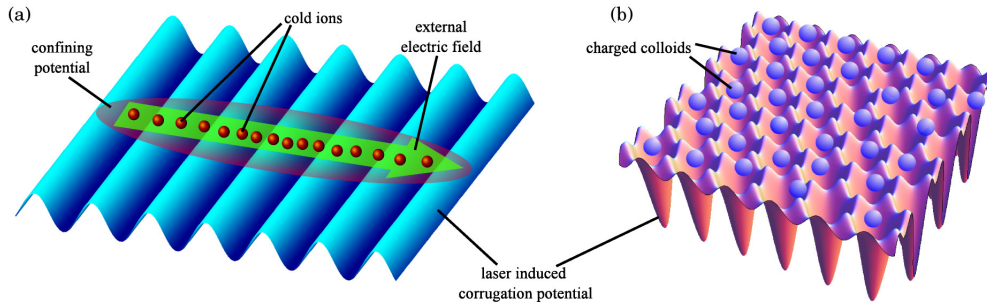
Figure 1.12: Artificial systems of charged particles interacting with optical lattices represent powerful tools to investigate frictional properties of ideal crystalline interfaces where all relevant parameters are under control. (a) Linear chain of cold ions interacting with a periodic, laser-induced "corrugation" potential realize a finite-size version of the Frenkel-Kontorova model, whose tribology is studied by applying an external electric field. (b) Two dimensional crystals of charged colloids immersed in water are promising candidates for fundamental studies of the friction between extended sliding ordered surfaces.

which may result in configurations where the adopted force-field ceases to be reliable. Where available, this problem can be solved using reactive potentials [127–129] developed in order to describe chemical reactions and wear. Limitations on the simulation duration and systems size represent another important issue. Considering the performance of modern CPUs, and classical MD based on empirical potentials, affordable sizes and simulation durations usually correspond to thousands of atoms and few μs. Typical sliding velocities of, e.g., AFM experiments are in the range of $\approx 1 \, \mu/sec$, so that a fully 3D simulation would be able to follow the tip just for $1 \, pm$, far too short to observe even a single atomic slip. Nevertheless the amount of useful information one can extract from MD simulations make it worth to run them at larger velocities. One can simplify the situation as follows. In fact, nanofriction may be smooth and viscous, or it may be of the stick-slip type. Viscous friction being proportional to velocity, it can be linearly extrapolated from large to small speed. Stick-slip friction being roughly independent on velocity may well be approached at large speed. Thus, despite the above limitations, nowadays MD simulations have become an essential tool for nanotribologists, as they can provide unique insights on the relevant dissipative mechanisms of sliding interfaces, allowing scientists to not only more accurately predict the frictional properties of real systems but also to identify the materials and conditions that determine specific tribological behaviors.

1.6 Artificial toy-systems for application in nanotribology

Charged particles trapped inside optical lattices have been recently proposed as novel candidates for studies in nanotribology [78, 120, 121, 130, 131]. The first model system we will investigate is realized by cold ions trapped inside an optical cavity (see Fig. 1.12a). Cold-atoms techniques allow to confine several tens of ions by means of quadrupolar fields in so-called Paul-traps [132], where they are forced to form linear chains, thus constituting finite size 1D Coulomb "crystals". When positioned inside an optical cavity the ions interact with the standing light wave provided by a laser beam. The maxima and the minima of the interference pattern result in a sinusoidal periodic potential felt by the ionized atoms, whose motion can be studied applying an external electric field. The overall configuration is to all effects similar to a finite-size realization of an

FK-like model, allowing to study in real experiments fundamental tribological aspects of this discrete one dimensional model [78, 121, 130]. The second system we will consider consists of charged colloidal particles suspended in water, which are pushed by the light pressure of laser beams to form a two dimensional triangular crystal, as shown in Fig. 1.12b. In a similar way to cold-ion traps, the interference pattern of the lasers can be adapted to produce a 2D substrate potential, which is felt by the charged colloids as a periodic sequence of wells and hills, mimicking the attractive and repulsive regions of a crystalline arrangement of atoms. Both these systems have been recently proved experimentally to be potential tools for understanding fundamental properties of sliding interfaces at the nanoscale. Bohlein and collaborators [120] observed for the first time the propagation of topological defects in sliding colloidal monolayers. More recently Byilinski et al. [133], and Gangloff et al. [134] demonstrated the effects of interface geometric incommensuration using very small chains of cold ions, and investigated the evolution of dynamic friction over a broad range of sliding speeds. These toy-models correspond to defect-free, ideal systems, mimicking the motion of a soft crystalline slider – the repulsive particles' crystal – interacting with a rigid non-deformable crystalline substrate – the optical lattice. Unlike conventional sliding surfaces, interfaces with different symmetries, lattice spacings, and corrugation amplitudes can be constructed at will, realizing, for example, commensurate or incommensurate matchings, quasicrystal substrate geometries, and possibly "disordered" geometries too. Experimentally all the relevant parameters are under control. The interface geometry, set by the ratio between the slider and substrate lattice spacings, can be tuned by changing the ions and colloidal density. The slider-substrate interaction strength is also under control, as it is fixed by the adjustable intensity of the laser beams. Most important, using advanced optical techniques in both cases the positions of the particles can be resolved in real time with resolution below the substrate periodicity, a unique possibility out of reach of any other "standard" tribological experiments.

A third class of experimental set up enabling the study of the atomic origin of friction is represented by QCM experiments. The cleanliness achieved under controlled UHV conditions allows to investigate *ideal* crystalline interfaces formed by films of rare gas atoms physisorbed on metallic surfaces. Depending on the temperature, coverage and ultimately on the system interactions at play, the equilibrium properties of the adsorbate may lead to different kind of interfaces, from commensurate or incommensurate solid-solid interfaces to liquid-solid interfaces [135–137], all characterized by distinct dynamical responses.

From the theoretical point of view, these model systems can be described by relatively simple effective hamiltonians. In typical experimental conditions cold ions are separated by few μm and cooled down below 1 μK, in a regime where quantum effects are negligible [130] and the ions dynamics is described by the classical motion of repulsive point masses moving in one dimension. Real colloidal crystal experiments as well are modeled by means of point like particles mutually interacting via a screened Coulomb potential, and undergoing an overdamped dynamics subject to a constant and homogeneous external force. Experimentally, the interfaces investigated in QCM are very well characterized, and allow for accurate modelization. Interactions between rare gas atoms are well described by appropriate reparametrizations of Lennard-Jones like potentials. Since the compressibility of metals is generally much lower than those for rare gases, deformations of the substrate are negligible. Realistic MD simulations of QCM experiments are therefore carried out modeling the periodic potential generated by the rigid substrate assuming that the interaction between a rare gas atom and the substrate can be represented as a sum of pairwise terms. In all three cases the low dimensionality, and the simple force fields involved, allow for extensive and systematic investigation of tribological properties with relatively small computational efforts.

1.7   Thesis outline

This thesis is a compilation of results presented or submitted to scientific journals. It addresses some fundamental issues regarding the sliding of dry crystalline interfaces. In particular we used the technique of molecular dynamics simulations to study the tribological properties of incommensurate 1D and 2D interfaces, as realized by charged particles trapped in optical lattices, and monolayers of rare gas atoms adsorbed on the metallic substrate of a QCM.

In Chapter 2 we consider 1D interfaces formed by cold-ions chain interacting with a laser-induced periodic potential. The aim of the chapter is to demonstrate how this artificial systems can be used to study (i) the transition from stick-slip to smooth-sliding regime, (ii) the details of the mechanisms at the onset of motion, and (iii) the change in the dissipative response across a parameter driven structural phase transition of the slider. These topics are all relevant with respect the general issue of controlling dissipation in nano-scale systems.
This Chapter is based on the following publication:
D. Mandelli, A. Vanossi, and E. Tosatti, "*Stick-slip nanofriction in trapped cold ion chains*", Phys. Rev. B **87**, 195418 (2013).

In Chapter 3 we present MD simulations of incommensurate colloidal monolayers sliding in presence of a periodic 2D optical lattice. The first question we address concerns the effects on dissipation of relative misfit rotations in genuinely incommensurate interfaces. We then present simulation results aimed at the characterization of the superlubric to pinned transition driven by increasing the particle-substrate interaction strength, a 2D equivalent of the Aubry transition extensively studied in the 1D FK model. The results obtained for the case study of colloidal monolayers are of more general validity. The mechanisms investigated in the simulations should in fact be at play in any clean incommensurate interface.
This Chapter is based on the following publications:
D. Mandelli, A. Vanossi, N. Manini, E. Tosatti, "*Friction Boosted by Equilibrium Misalignment of Incommensurate Two-Dimensional Colloid Monolayers*", Phys. Rev. Lett. **114**, 108302 (2015).
D. Mandelli, A. Vanossi, N. Manini, E. Tosatti, "*Superlubric-Pinned Transition in Sliding Incommensurate Colloidal Monolayers*", arXiv:1508.00147 [cond-mat.mes-hall]. To appear in Phys. Rev. B.

In Chapter 4 we focus on the problem of static friction. Here we consider the case study of hard incommensurate rare gas submonolayers physisorbed on a metallic substrate, which are realized in QCM experiments. We present results of realistic simulations concerning the scaling of static friction as a function of the adsorbed island size, highlighting the role played by the slider edges in determining the pinning barrier. We also investigate the effects of temperature and edge geometry.
This Chapter is based on the following publication:
N. Varini, and A. Vanossi, and R. Guerra, and D. Mandelli, and R. Capozza, and E. Tosatti, "*Static friction scaling of physisorbed islands: the key is in the edge*", Nanoscale **7**, 2093 (2015).

CHAPTER 2

Stick-Slip Nanofriction in Trapped Cold Ion Chains

The key feature of friction between solid bodies is hysteresis, that is the difference between to and fro motion. In time-periodic sliding motion for example, hysteresis is responsible for the finite area enclosed by the force-displacement cycle, which exactly equals the frictional heat per cycle. Smallest when the sliding regime is smooth, friction turns large when sliding occurs by stick-slip – a discontinuous stop and go which constitutes the largest and commonest source of frictional hysteresis. Generally triggered by mechanical instabilities, stick-slip takes place at geological, ordinary, and at nanometer length scales alike [9, 96, 97]. Restricting here to the nano and microscale, which is the focus of much current work, we are naturally interested in microscopical systems exhibiting a controlled transition between smooth and stick-slip sliding regimes. Anticipating experiments we will present molecular dynamics (MD) simulations of linear chains of cold ions sliding over a laser-induced periodic potential. In particular we suggest that they can be used to study stick-slip as well as the effects on friction of parameter-driven structural phase transitions occurring inside the slider, another issue of interest in tribology as it may provide a way to control dissipation.

The Chapter is organized as follows. Section 2.1 contains the motivations for this study, a brief description of the system, and a discussion of previous investigations. In Section 2.2 we describe the model and the protocols used in our MD simulations. Section 2.3 is devoted to the resulting smooth to stick-slip frictional switch. In Section 2.4 we describe the change of the frictional behavior across the linear-zigzag structural transition of the ion chain. Finally Section 2.5 contains our discussion and conclusions.

2.1 Introduction

Recently chains of cold ions trapped inside optical lattices have been proposed as novel candidates for studies in the field of friction [78, 130]. One of the motivations has been the possibility to observe, thanks to their exceptional parameter tunability, the long theorized Aubry transition, namely the switch between a regular frictional state and the "superlubric" state of vanishing static friction between idealized incommensurate one dimensional (1D) "crystals". One dimensional periodic sliding models, although highly simplified, have long been used to illustrate frictional phenomena between periodic lattices [138]. In the so-called Frenkel Kontorova (FK) model [99], a harmonic chain of classical masses with average spacing a_o interacts with a sinusoidal periodic potential of amplitude U_0 and wavelength λ, leading to a commensuration
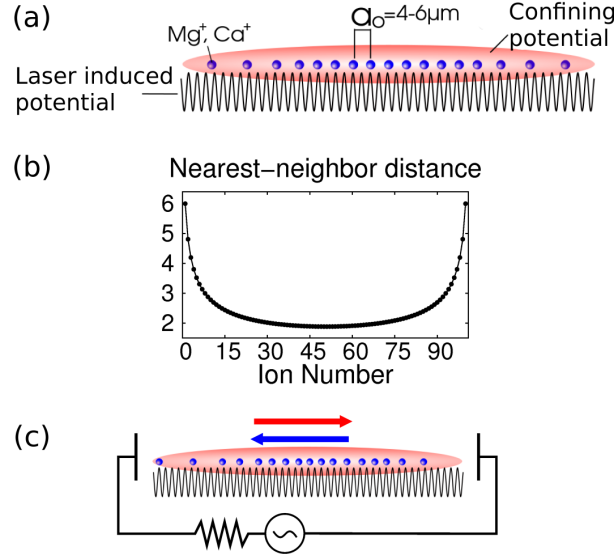
Figure 2.1: (a)Schematic of a linear ion chain trapped by an anisotropic confining potential. Typical ions used in experiments are Ca^+ or Mg^+, the ion-ion distance at the center of the chain is of the order of few μm. (b)Nearest-neighbor distance (in dimensionless units, see Section 2.2) between the ions of a 101-ions chain at rest and in absence of the corrugation potential. (c)A possible experimental set-up for the study of the dynamics of the chain using an external oscillating electric field.

ratio $\rho = a_o/\lambda$ between the two. Such system idealizes the sliding of two crystalline surfaces. Irrational values of ρ characterize the most interesting incommensurate case between slider and substrate. Aubry [95, 101] proved long ago that a transition occurs for increasing U_0, from what is now known as a superlubric state where the static friction F_s – the minimal force capable of initiating sliding – is exactly zero, to a *pinned* state where F_s is finite. While exceptionally low friction between incommensurate 3D surfaces has indeed been observed experimentally [111], there had not been so far experimental demonstrations of the Aubry transition in genuinely 1D systems. Cold ion traps were recently invoked as possible candidates to display the Aubry transition, thereby surprisingly entering the field of nanotribology [78]. Although not identical to the FK model, the physics of repulsive particles confined in 1D is expected to be essentially the same as each ion can still be seen as occupying the center of some overall harmonic potential. Experimentally [121], chains of up to several tens of positive ions such as Ca^+ or Yb^+ can be stabilized using rf quadrupolar fields and cooled down to temperatures below 1 μK. By tuning the confining cigar-shaped potential to a sufficiently elongated form, the ions can be forced to form linear chains, while the periodic lattice potential for the ions is provided by a laser standing wave (see Fig. 2.1a). The position of each single ions can be monitored using advanced optical techniques with a space resolution below the optical lattice wavelength λ. This allows to study in details both the ion crystal static structural properties and its dynamics under forced sliding [133, 134]. The confined ion chains do constitute 1D crystal segments, but are not really homogeneous. The nearest neighbor ion-ion distance, fairly constant at the center, increases at the periphery and diverges near the extremities, as shown in Fig. 2.1b. Still, the chain center is a reasonable realization of an FK-like model, and some of the properties of an ideal infinite system can be in principle realized and observed there [78, 130]. In particular, when λ is incommensurate with
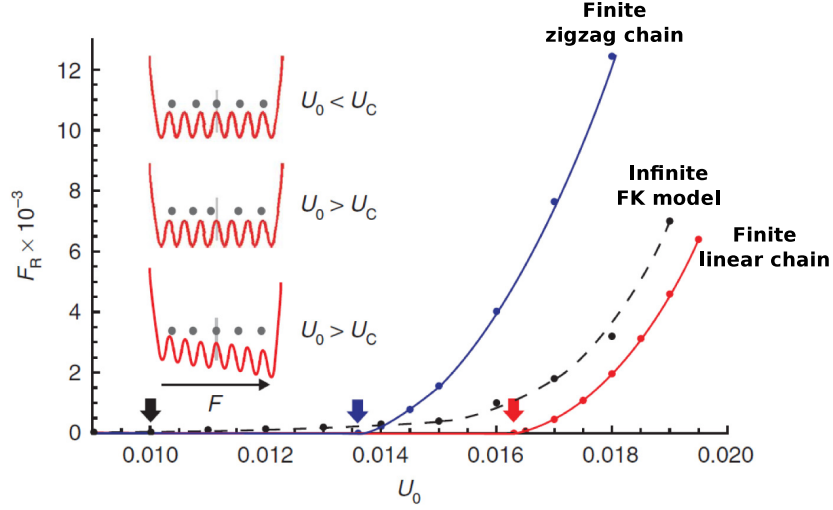
Figure 2.2: Effective static friction of a 101-ions chain in the linear (red) and zigzag (blue) configuration plotted against the corrugation potential amplitude U_0. The black dashed line is the static friction of the ideal FK model. (Results taken from Ref. [78])

respect to the central ion-ion spacing a_o one can achieve, according to recent predictions [78], a strong and observable remnant of the Aubry transition. In the confined ion chain, the standard Aubry transition, which in the infinite chain occurs when the periodic potential ("corrugation") amplitude U_0 exceeds some critical threshold U_c, is replaced by a static, symmetry breaking transition of the ground state configuration and geometry. Benassi and coworkers [78] proposed to observe this transition by measuring the external uniform force F_R needed to restore the symmetry. Simulations indeed showed that the effective static friction force F_R behaves and grows as a function of $U_0 > U_c$ very closely like the static friction force F_s of the ideal infinite chain thus demonstrating the connection between the two (see Fig. 2.2).

In the present work we move from static friction to the dynamical sliding properties of the ion chain. In anticipation of future experiments, we have performed classical molecular dynamics simulations of a 101-ions chain sliding in a golden ratio incommensurate corrugated potential, with a view to predict and discuss the basic dynamic frictional phenomena of an electric field solicited trapped ion chain (see Fig. 2.1c). The first question we address is how the chain sliding is affected as a function of increasing periodic corrugation amplitude U_0. Drawing an analogy with macroscopic frictional experiments, the corrugation plays here the role of the load in ordinary sliding friction. We show that the trapped cold ions can slide either smoothly or by stick-slip, with a parameter-controlled transition and a correspondingly strong frictional rise between the former and the latter. As expected, we find and characterize the transition from a poorly dissipative smooth sliding regime to a highly dissipative stick-slip regime as U_0 is increased. The second question we address regards the effects on sliding friction of a phase transition occurring inside the chain, another issue of current interest [78]. As it is known both theoretically [139, 140] and experimentally [141], a change of aspect ratio in the confining trap effective potential causes the ion chain to cross a series of structural transitions, from a linear to a planar zig-zag configuration, further transforming into a fully 3D helix structure. If and when for a sufficiently long chain these transitions can be considered continuous, the frictional behavior near the transition point could show remnants of the chain's critical behavior, as recently suggested theoretically [78].
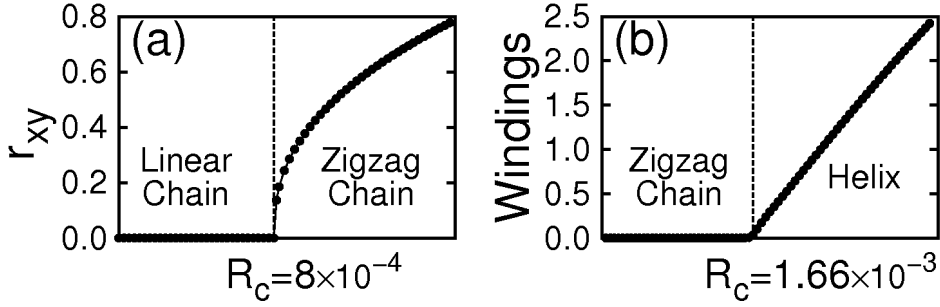
Figure 2.3: (a)Linear-zigzag structural transition of a 101-ions chain. r_{xy} is the maximum displacement of the ions from the z axis. (b)Zigzag-helix transition. The order parameter is the number of windings of the ions around the z axis.

2.2   Model and simulation protocols

The effective potential of an ion of charge q in a linear anisotropic (Paul) trap can be written as [132]:

$$V_{eff}(x, y, z) = \frac{m}{2} \left[\omega_\perp^2 (x^2 + y^2) + \omega_\parallel^2 z^2 \right], \qquad (2.1)$$

where m is the mass of the ion and $\omega_\perp^2$ and $\omega_\parallel^2$ are the strengths of the confining effective potential, supposed to be harmonic, in the transverse and longitudinal directions. In order to work in dimensionless units we define the length unit d:

$$d = \left(\frac{q^2}{4\pi\epsilon_0 m \omega_\perp^2} \right)^{1/3}. \qquad (2.2)$$

We then measure masses in units of m, charges in units of q, energy in units of $q^2/(4\pi\epsilon_0 d)$, forces in units of $q^2/(4\pi\epsilon_0 d^2)$ and time in units of $1/\omega_\perp$. The effective Hamiltonian of N trapped ions is then [142, 143]

$$H_{eff} = \sum_{i=1}^{N} \left\{ \frac{\mathbf{p}_i^2}{2} + \frac{1}{2} \left[\omega_\perp^2 \left(x_i^2 + y_i^2 \right) + \omega_\parallel^2 z_i^2 \right] + U_0 \cos\left(\frac{2\pi}{\lambda} z_i \right) + \sum_{j\neq i} \frac{1}{|\mathbf{r}_i - \mathbf{r}_j|} \right\}, \qquad (2.3)$$

where the sinusoidal term represents a laser induced periodic potential, mimicking the corrugation of a hypothetical crystalline substrate lattice.

The ground state geometry of the ions at $T = 0$ depends on the aspect ratio $R = (\omega_\parallel/\omega_\perp)^2$ of the anisotropic harmonic confining potential. For small enough R the potential is cigar-like, and ions are forced to form a linear chain along the trap symmetry axis, z. As R is increased there is a sequence of shape transitions: first from a straight chain to a planar zigzag chain; next, a second transition where planarity is lost, and the planar zigzag turns into a helix. Still at $T = 0$, and for an infinite chain, both classical transitions are continuous [1]. as shown in Fig. 2.3

Following Benassi et al. [78], the main results have been obtained simulating a chain of 101 positive ions choosing $\omega_\parallel^2 = 0.0005$, $R = 0.0005$ and a golden mean incommensurate ratio

---

[1]Note that strictly speaking at $T = 0$ we should not ignore quantum effects and treat this transition as a quantum critical point, as developed for example in Ref. [144].
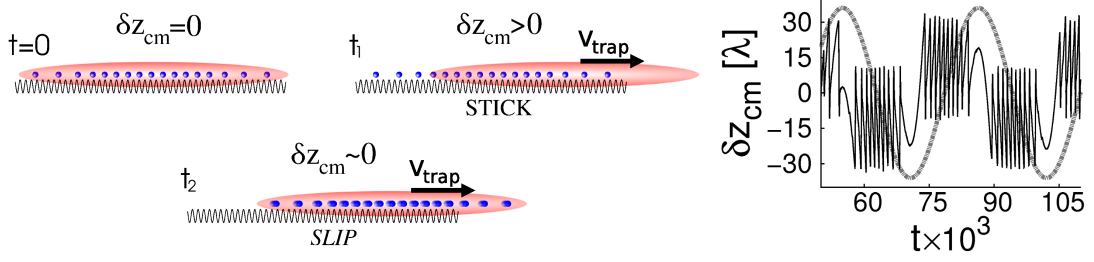
Figure 2.4: Dynamics of δz_{cm} (see text) under periodic sliding. At t=0 the chain is almost symmetric with respect to the vertex of the confining parabola and $\delta z_{cm} \approx 0$; if the chain is locked to the substrate δz_{cm} increases as the confining potential moves until a slip event occurs, which corresponds to a sudden drop to zero of δz_{cm}. The plot shows a result from a simulation where many slip events are observed during each oscillation back and forth of the chain over the substrate. The grey dashed line corresponds to the external electric field.

$\rho = \lambda/a_o = 2/(1+\sqrt{5})$, where a_o is the center ion-ion spacing. A more practical parameter choice, closer to typical experimental set-up, is considered and discussed in Appendix A. Chain sliding is caused by an external slowly oscillating electric field $\mathbf{E}(t) = \hat{\mathbf{z}}E_0 \sin(\Omega t)$ acting on each ion in the longitudinal direction, z. We carried out classical damped molecular dynamics integrating the equations of motion using a standard velocity-Verlet algorithm with time step $\Delta t = 0.005$. At each time the total force acting on the ith ion is given by:

$$\ddot{\mathbf{r}}_i = \mathbf{F}_i^{Coul} + \mathbf{F}_i^{trap} + \mathbf{F}_i^{sub} - \gamma\mathbf{v}_i, \tag{2.4}$$

where we have respectively the force due to the ion-ion Coulomb repulsion, the confining potential force, the corrugation force and a velocity dependent dissipative force controlled by a damping parameter γ. There is no random force, corresponding to our "$T = 0$" background assumption. The trap confinement plus oscillating potential is given by

$$V_{ext}(z) = \frac{\omega_\parallel^2}{2}z^2 - zE_0 \sin(\Omega t), \tag{2.5}$$

which is a confining parabola of vertex $z_{trap} = E_0 \sin(\Omega t)/\omega_\parallel^2$ moving at velocity $v_{trap} = E_0\Omega \cos(\Omega t)/\omega_\parallel^2$. In order to follow stick-slip, when present, we monitored the distance of the center of mass of the chain from the minimum of the moving parabola:

$$\delta z_{cm}(t) = z_{trap}(t) - z_{cm}(t). \tag{2.6}$$

Figure 2.4 shows an example of the time evolution of δz_{cm} corresponding to a sequence of external electric field oscillations.

The dynamic friction of the system is computed as the work W done by the oscillating electric field on all the particles:

$$W_k = \frac{1}{N}\sum_{i=1}^{N}\int_k dt[\mathbf{v}_i \cdot \hat{\mathbf{z}}E_0 \sin(\Omega t)]. \tag{2.7}$$

Where the integral is calculated over the kth period corresponding to the electric field going from its minimum value $-E_0$ to its maximum value $+E_0$ and back. The final estimate of the dynamic
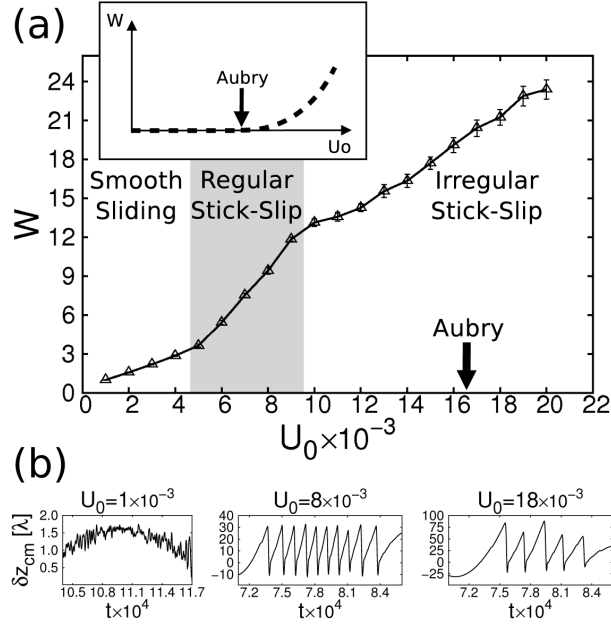
Figure 2.5: (a) Dynamic friction W of the oscillating ion chain as a function of the corrugation amplitude U_0. The values of $E_0 = 0.1625$, $\Omega = 0.0002$, $\gamma = 0.01$ were chosen so as to yield 4-5 slip events during each oscillation in correspondence of the highest values of U_0 investigated. (b) Dynamics of δz_{cm} in the three different regimes of smooth-sliding, regular and irregular stick-slip. The time interval plotted corresponds approximately to half a period of the oscillating electric field which increases from $-E_0$ to $+E_0$.

friction is obtained from the average of the M samples W_k measured during the whole trajectory:

$$W = \frac{1}{M} \sum_{k=1}^{M} W_k. \tag{2.8}$$

2.3   Dynamic friction, stick-slip and precursor events

Figure 2.5a shows the frictional work W done by the external electric field on the trapped ion chain as a function of the corrugation amplitude U_0. The inset depicts schematically the expected behavior in the infinite incommensurate FK model, where for $U_0 < U_c$, below the Aubry transition, motion takes place without static friction, and kinetic friction vanishes in the limit of infinitely slow sliding. In the chain of trapped ions, finite and inhomogeneous, the static friction force needed for overall chain motion is nonzero for all corrugations, since the two extremities are always locked to the corrugation potential. Correspondingly, there is upon sliding a finite frictional dissipation W for all values of U_0. For the chosen external field frequency $\Omega = 0.0002$ and amplitude $E_0 = 0.1625$ friction grows steadily with corrugation U_0 and nothing significant happens to the dynamic friction W across the nominal [78] Aubry value $U_c = 0.01628$. In fact the dynamics of the chain does not change appreciably above $U_0 \approx 0.01$.

We can resolve, based on the detailed nature of the sliding trajectories, three different dynamical regimes. Figure 2.5b shows the dynamics of δz_{cm} for three representative values of U_0.
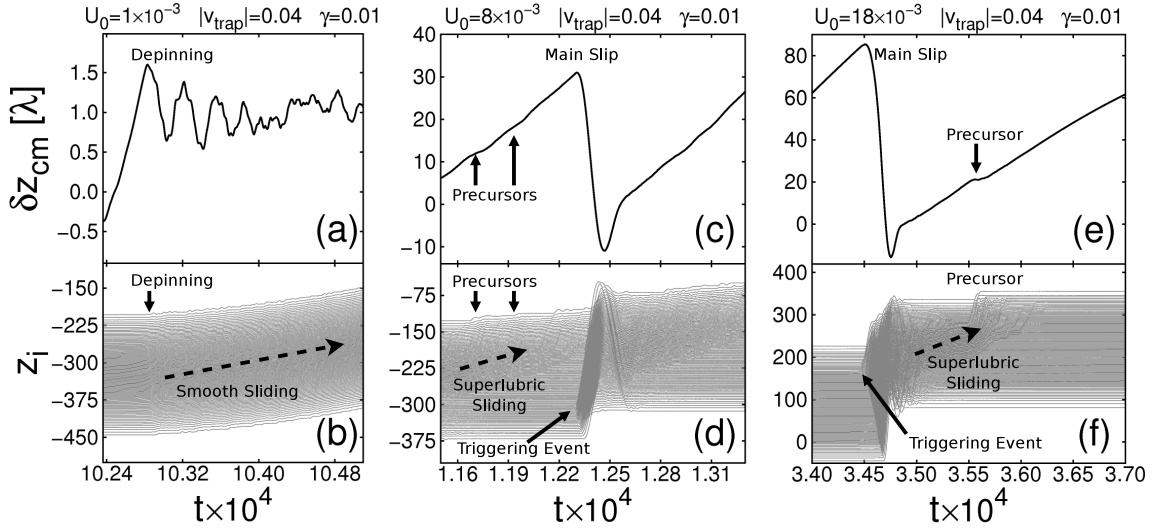
Figure 2.6: (a)Dynamics of δz_{cm} in the smooth sliding regime; panel (b) shows the corresponding trajectories of each ion. (c)Dynamics of δz_{cm} in the regular stick-slip regime; panel (d) shows the corresponding trajectories of each ion. (e)Dynamics of δz_{cm} in the irregular stick-slip regime; panel (f) shows the corresponding trajectories of each ion.
The features highlighted in the figure are discussed in Section 2.3.

For small corrugations $U_0 \leqslant U_{01} = 0.005$ the chain follows smoothly the external force and the friction is modest (with a value determined by, and growing with, the sliding velocity, in turn proportional to Ω). As U_0 is increased further, the smooth sliding dynamics is replaced by a regular, time-periodic stick-slip regime with accompanying increase of dissipation. So long as $U_{01} \leqslant U_0 \leqslant U_{02} = 0.01$ the slip magnitude is fairly constant during each oscillation. For larger corrugations finally, $U_0 \geqslant U_{02}$ the chain enters a chaotic regime of irregular stick-slip.

Figure 2.6 shows details of the trajectories of the chain center of mass and of all individual ions in the three regimes. For $U_0 \leqslant U_{01}$ the chain is weakly pinned at the inversions of motion occurring for $E(t) = \pm E_0$. After the depinning the chain follows smoothly the external force; small oscillations of δz_{cm} are due to internal motion of the chain (see Fig. 2.6a,b). A number of interesting features appear at the onset of stick-slip $U_0 \geqslant U_{01}$, and they are shown in Fig. 2.6c-f. The head and the tail of the ion crystal are locked to the corrugation potential (see top and bottom parts of Fig. 2.6d, initial times) while the truly incommensurate central part is free to slide, thus increasing the ion density of the head, reducing that of the tail and inducing partial depinning of the chain. The precursor events appear in the head part (see top part of Fig. 2.6d, times between $t = 1.16$ and $t = 1.22$). Although different and connected with inhomogeneity of stress rather than of contact, partial precursors were also shown to precede the onset of macroscopic sliding by Fineberg's group [86, 87]. Partial slips of the chain always start within the central superlubric region and proceed moving in the direction of the external force. They are present only in the stick-slip regime and disappear by increasing the average pulling velocity $|v_{trap}| = 2E_0\Omega/\pi\omega_\parallel^2$ of the trapping potential (see Fig. 2.7).

Following the precursors, as stress accumulates more and more in time, the system undergoes a mechanical instability typical of stick-slip [97]. The ensuing main slip of the whole system is triggered by the creation of a kink-antikink pair (see Fig. 2.8). In the regular stick-slip regime $U_{01} \leqslant U_0 \leqslant U_{02}$ the tail drives the sliding onset, and the triggering pair forms in the tail region,
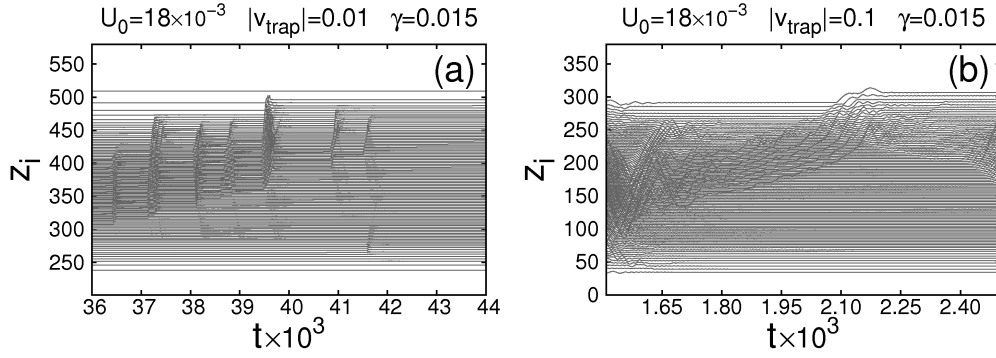
Figure 2.7: Precursor events observed between two main slip events for (a) $|v_{trap}| = 10^{-2}$ and (b) $|v_{trap}| = 10^{-1}$. As the pulling velocity is increased the precursor events disappear signaling the transition from stick-slip motion to smooth sliding.
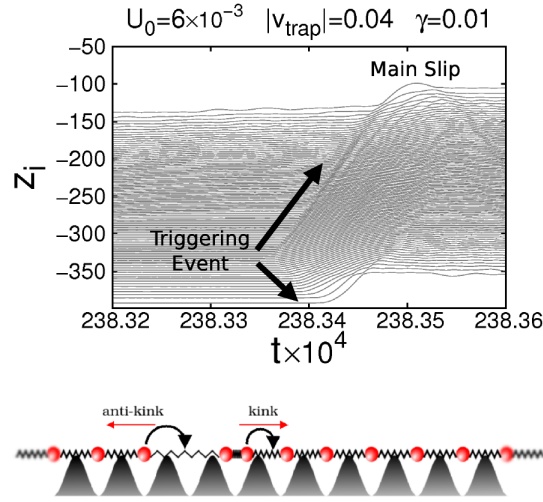

Figure 2.8: Example of a triggering event inducing the main slip.

while the chain center and front are still free to slide (see Fig. 2.6d, times between $t = 1.22$ and $t = 1.25$). In the chaotic stick-slip regime $U_0 \geqslant U_{02}$ instead, the onset of sliding is different. The central superlubric flow and partial slips of the front ions first bring the chain into a metastable state where each ion is locked to the corrugation (see Fig. 2.6f, times between $t = 3.5$ and $t = 3.6$). The generation of a kink-antikink pair forming now in the chain head, as opposed to the chain tail of the previous regime, eventually leads to global sliding, as shown by the main slip event at the initial times of Fig. 2.6f. This tail-to-head switch of the triggering event is a characteristic signature always accompanying the passage from regular to chaotic stick-slip. On the other hand, neither the sliding onset dynamics nor the dynamical friction magnitude finally display any particular feature or singularity when the corrugation grows across the Aubry transition. This result underlines a substantial difference between the frictional behavior of this short and inhomogeneous chain, and that expected of an ideally infinite and uniform FK-like chain. In the latter and ideal system there is no other transition than Aubry, and in the limit of zero sliding speed stick-slip sliding can only take place when static friction turns nonzero, which
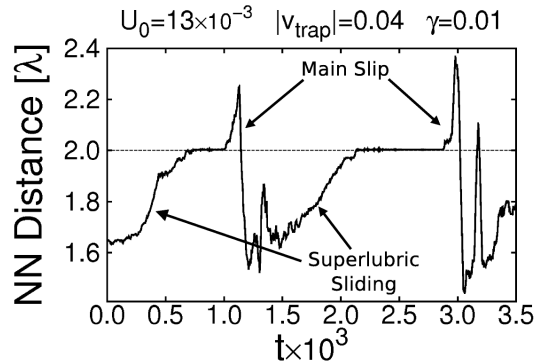
Figure 2.9: Average ion-ion distance (in units of λ) versus time; we considered only the central 31 ions of the chain. After the passage of the superlubric front the center of the chain is left in a commensurate configuration with ions equally spaced by 2 λ. The same kind of dynamics occurs at the onset of motion at each values of U_0 in the stick-slip region.

is above the Aubry transition. Figure 2.9 shows details of the sliding dynamics in the strongly corrugated, chaotic stick-slip regime. The average nearest neighbor distance between the central 31-ions portion is displayed as a function of time between two main slips of the crystal. The initial passage of the "superlubric" front brings the central part to a commensurate configuration with ions spaced exactly by 2 λ (instead of the original golden ratio spacing 1.618 λ) from one another. This dynamically induced commensuration brings the whole chain to a temporarily locked state thus increasing the static friction force needed for the onset of overall motion [2]. Subsequent depinning of the chain off this locked state only occurs as the external force grows further, and is sudden. This two-stage nature of sliding, and the relative abruptness of the depinning is at the origin of the chaotic behaviour of stick-slip in this regime.

2.4 Friction singularity across a structural transition

Benassi et al. recently proposed that interesting frictional changes or anomalies could be observed in presence of structural phase transitions [72]. In finite size systems near second order phase transitions divergences are replaced by broad peaks, which are the signature of the critical behaviour expected in the thermodynamic limit. It is therefore still interesting to find out what "singularities" would friction develop upon an overall, collective shape change of our trapped ion chains. To study that we used a 101-ions chain golden mean incommensurate with respect to the substrate corrugation potential. We carried out simulations at values of the trapping potential aspect ratio R straddling the critical value $R_c = 0.0008$ for the linear-zigzag transition (see Fig. 2.3a). Although this kind of effect should be quite general, the expected delicacy of this frictional feature should best become apparent under sliding conditions with limited noise, such as those expected at weak corrugations. Setting $U_0 = 0.0008$ and also γ, Ω and E_0 values which lead to a smooth and gentle sliding dynamics (disturbing the chain to a minimal extent) we obtained the dynamic friction of Figure 2.10a. Deep enough in the linear chain regime ($R \leq 0.00064$) the ions remains in a strictly 1D configuration during the whole dynamics. Here, only longitudinal internal vibration degrees of freedom of the chain are excited and W is small and essentially

---

[2]A similar behavior has been observed in MD simulations of 2D mesoscopic colloidal monolayers driven over an incommensurate optical lattice [131].
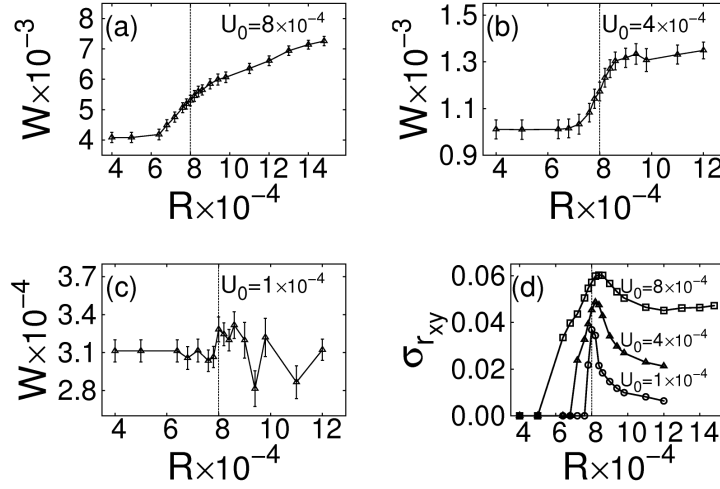
Figure 2.10: (a)Dynamic friction across the linear-zigzag transition for U_0=0.0008. Parameters used are: γ=0.0005, E_0=0.005078125, Ω=0.0032. Without corrugation potential the chain moves as a rigid body at a very low dissipation rate independent on R (not shown). As U_0 is switched on, the internal degrees of freedom of the chain begin to dissipate. In this set of simulations the transverse modes begin to be excited at $R \approx 0.00064$. (b) Dynamic friction across the linear-zigzag transition for U_0=0.0004 and (c) U_0=0.0001, using E_0=0.002539063, Ω=0.0032, γ=0.0005. By lowering the external electric field and the amplitude of the substrate potential the onset of the excitation of the transverse modes is shifted towards the static critical value R_c=0.0008. In this set of simulations the transverse modes begin to be excited at $R \approx 0.00072$ and $R \approx 0.00078$ respectively for U_0=0.0004 and U_0=0.0001. (d)Standard deviation $\sigma_{r_{xy}}$ of the maximum displacement r_{xy} of the ions from the z axis plotted as a function of R and measured using the whole trajectories of the simulations of panels (a),(b),(c). $\sigma_{r_{xy}}$ is zero until the transverse modes begin to be excited and it shows a clear maximum near R_c, which becomes sharper as U_0 is decreased.

independent of R. As the critical anisotropy R_c is approached the transverse vibration modes of the chain soften and become rather suddenly excitable, a new dissipative channel opens and W rises anticipating the linear-zigzag transition. In a hypothetical infinite chain, where the transition occurs continuously and critically, the frictional behavior will presumably also exhibit a critical singularity. Given the finite chain size, the frictional rise is smooth, although it can still be sharpened by reducing the corrugation amplitude. Figures 2.10b,c show results of simulations with U_0 reduced down to 0.0004, 0.0001 and a lower value of E_0. The transverse mode excitation onset occurs nearer to R_c. That result is made clearer in Fig. 2.10d where the standard deviation $\sigma_{r_{xy}}$ of the maximum displacement of the ions away from the z axis is plotted against the aspect ratio R. Denoting with $< \dots >$ the time average over the whole trajectory, $\sigma_{r_{xy}}$ and r_{xy} are defined as:

$$\sigma_{r_{xy}} = \sqrt{< (r_{xy}- < r_{xy} >)^2 >} \tag{2.9}$$

$$r_{xy} = \text{Max}_{\{i=1, N_{ions}\}}(\sqrt{x_i^2 + y_i^2}) \tag{2.10}$$

$\sigma_{r_{xy}}$ is zero until the transverse modes begin to be excited and it displays a maximum near the critical point R_c. A further increase of R drives a subsequent transition of the trapped ion geometry from zigzag to helix, but not much happens here. In this case in fact, on both side of

the critical point the chain is already in a 3D configuration and its dissipative properties are not significantly affected by the weaker helical distortion.

2.5   Final remarks

Stick-slip motion is a paradigmatic behavior of any sliding systems, observed from nano to geological scales. Here we have suggested that trapped cold ions in an optical lattice can be of help in understanding stick-slip friction, and also the way friction changes when one of the sliders undergoes structural transitions. For that scope, we simulated the dynamical properties of a 101-ions chain, driven to slide back and forth by a slowly oscillating electric field in a golden mean incommensurate periodic "corrugation" potential of increasing magnitude U_0. Summing up the results, as U_0 is increased the system turn from smooth sliding to a stick-slip sliding regime, first regular and then chaotic. Accompanying the transition there is an increase in the dissipation rate, as is also observed in macroscopic dry friction when the loading force is increased. Three separate frictional regimes have been identified. A smooth sliding one for weak corrugation, followed by time-periodic stick-slip sliding at larger corrugation, eventually leading to chaotic stick-slip for even larger corrugation. Due to the inhomogeneity of the ion crystal the frictional dynamics of the ion chain shows several novel features reflected in the ion trajectories. The two chain extremities are always pinned while the incommensurate central part is free to slide following the external force. The onset of motion in the stick-slip regime is characterized by the presence of precursor events, i.e. partial slips of side chain portions induced by the superlubric flow of the truly incommensurate central part. The chaotic stick-slip at large corrugation is connected by an interesting two-stage process. First, superlubric sliding of the central portion bring the chain to a temporary commensurate state, locked to the periodic corrugation. Subsequently, as force grows, a kink-antikink pair is generated and propagates toward the extremities eventually inducing the slip of the whole system. We also studied the possible anomalies of friction dissipation across the structural phase transformations of the trapped ions obtained by varying the aspect ratio $R = (\omega_\parallel/\omega_\perp)^2$ of the harmonic trapping potential. At fixed $\omega_\parallel$, as R is increased, the ion chain transforms first from a linear configuration to a planar zigzag and then to a helix. The energy dissipation increases characteristically at the linear to zigzag transition as the softening of the transverse modes opens new dissipative channels. Conversely, the zigzag to helix transition does not yield significant frictional changes.

Recently the first frictional experiments [133, 134] were performed using chains of up to six cold ions. In particular the effects of incommensuration were demonstrated – quite surprisingly – to emerge already in the limiting case of just three ions, with some hints suggesting that the Aubry transition could be accessible even in this tiny crystals [145, 146]. The experimental conditions adopted in those studies are far from our simulation set-up considering 101 ions, where one should be able to observe a strong stick-slip regime. However, numerical investigations performed in a range of experimentally accessible parameters (see Appendix A) reveal that the more relevant dynamical features should become observable in future experiments.

CHAPTER 3

Sliding Friction in Incommensurate Colloidal Monolayers

Bohlein and collaborators [120] showed that the sliding of a 2D crystalline monolayer of colloidal particles in an optical lattice provides unexpected information on elementary tribological processes in sliding crystalline interfaces with ideally controlled commensurabilities. Given the scarcity of reliable and controllable frictional systems, it is hard to overestimate the importance of such artificial interfaces with full external control over all parameters including periodicity, coupling strengths, and applied forces. For this reason 2D monolayers in periodic lattices require a close theoretical study. In this Chapter we consider the general case of incommensurate interfaces by studying the static and dynamic properties of 2D colloidal monolayers via realistic MD simulations, in principle directly comparable with experiments in the set-up of Ref. [120]. We first show that the ground state configuration usually corresponds to a monolayer slightly misaligned with respect to the substrate periodic potential. This small misalignment, so far overlooked, have significant consequences on the dissipative sliding of the interface, when compared to the aligned case. Second, we focus on the static friction force F_s of the monolayer and we describe the transition from the free sliding ($F_s \approx 0$) to the pinned regime ($F_s > 0$) as a function of the monolayer-substrate interaction strength, which we find to coincide with a first order structural transition of the colloidal crystal.

The Chapter is organized as follows. Section 3.1 introduces the system under study, discusses the motivations for the present investigation and outlines the main questions addressed in the Chapter. In Section 3.2 we describe the model and the protocols adopted for the simulations. Section 3.3 is devoted to the description of the misaligned ground state configuration of the interface and its dissipative properties under sliding, while in Section 3.4 we describe the free-sliding to pinned transition. Section 3.5 contains our final remarks and conclusions.

3.1 Introduction

Our reference is the experiment by Bohlein [120] and co-workers, which uses repulsive colloidal particles suspended in water. Colloids are confined by the light pressure of laser beams and forced to reside in a 2D region, where they form a periodic triangular lattice whose mean spacing a_c – of the order of few μm – is set by the adjustable 2D particle density (see Fig. 3.1). The interference fringes of the same laser beams also provide a periodic substrate "corrugation" potential of
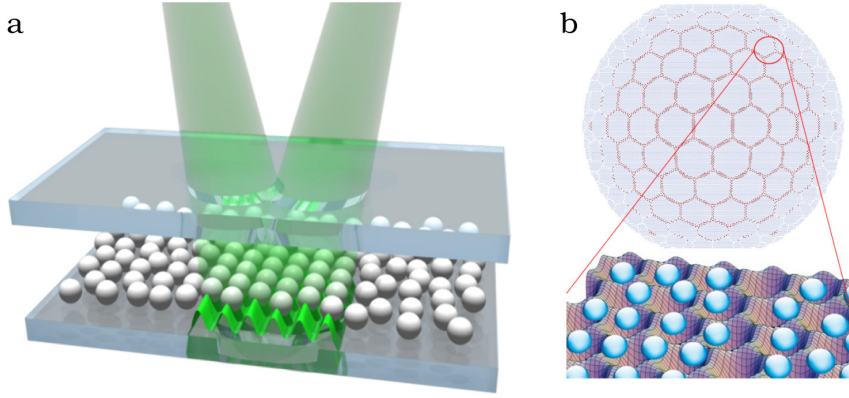
Figure 3.1: (a) Charged colloidal particles suspended in water are pushed towards the bottom of the experimental cell by the pressure applied using interfering laser beams. They reside in a 2D region forming a triangular crystal, whose mean lattice spacing is of the order of 4-5 μm, tuned by controlling the particle density inside the cell. (b) Colloids form an extended 2D island displaying density modulations (the moiré solitonic pattern) as they interact with the periodic substrate "corrugation" potential generated by the lasers interference, as depicted schematically in the inset.

spacing a_l felt by the charged colloids, mimicking the periodic potential of an atomically ordered surface (an optical lattice of triangular symmetry would correspond, e.g., to the (111) plane of an fcc crystal), and whose strength U_0 is controlled by the laser intensity. Sliding is achieved by applying a driving force F_d to all particles via the viscous drag induced by moving back and forth, inside the optical cavity, the experimental cell containing the colloidal suspension. These experiments represent a realization at the micrometer length scale of the ideal sliding between a mobile "atomic" monolayer (the sliding colloidal crystal) over a rigid crystalline substrate (the optical lattice). The really innovative feature introduced by this set-up relies on the possibility to follow in real time the particles' positions and velocities, allowing one to investigate in full details the ongoing dynamical mechanisms, hitherto restricted to the ideal world of MD simulations.

Two atomically flat and perfect crystal surfaces in contact are commensurate when the mismatch ratio $\rho = a_l/a_c$ between their lattice parameters is rational. Perfect matching ($\rho = 1$) between two lattices of same symmetry represents the simplest situation, where the atoms of one crystal lattice (the slider) perfectly fit the minima of the two-dimensional "corrugation" periodic potential landscape generated by the other lattice (see Fig. 3.2a). Both experiments [120] and theory [131, 147] indicated that commensurate ($\rho = 1$) friction is large. Also, in this case a finite and large external force is required to dislodge the slider atoms from the potential minima, so as to nucleate, at finite temperature [148, 149], the onset of sliding. A situation far more common in nature corresponds to a mismatch between the periodicities of the two contacting lattices usually realized by a value $\rho \neq 1$, as shown schematically in Fig. 3.2b. Incommensurate interfaces also naturally exhibits more interesting tribological features than commensurate ones [131]. In this case friction is much smaller than the one observed in commensurate geometries, the drop reflecting the great mobility of pre-existing misfit dislocations, also called kinks or "solitons".

Here we focus on colloidal crystals sliding over a triangular periodic potential at fixed geometry (fixed ρ), and we investigate the frictional properties of incommensurate interfaces. At zero temperature, a systematic study of the tribological features of the colloidal monolayer requires first of all to look for the lowest total energy configuration at each given value of the
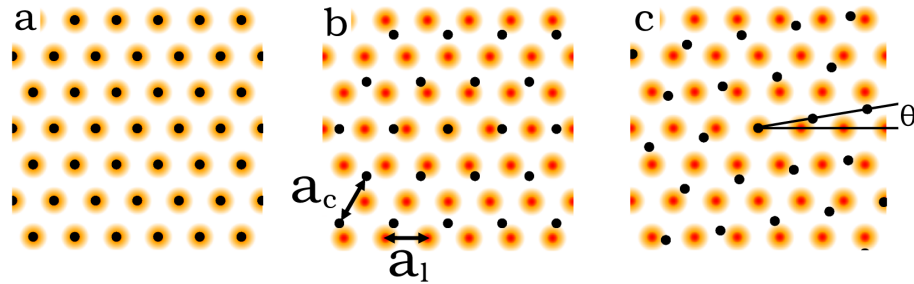
Figure 3.2: (a) Schematics of a $\rho = 1$ commensurate interface between a colloidal monolayer (black dots) and a triangular optical lattice potential (light spots correspond to the minima). (b) A colloidal monolayer of lattice spacing a_c with a mismatched triangular potential of periodicity $a_l = \rho a_c$. The two lattices are mismatched but aligned. (c) Colloidal monolayer with a small misfit angle θ with respect to the mismatched substrate. This kind of rotation generally lowers the energy and is a likely equilibrium feature [150].

corrugation parameter U_0. For a perfectly commensurate ($\rho = 1$) interface the global minimum of the total energy corresponds to the trivially aligned case where each particle sits in one well of the substrate potential. However for incommensurate interfaces one has to keep in mind that the aligned case shown in Fig. 3.2b is not necessarily energetically favourable. It is known [151], for example, that a harmonic monolayer subject to a weak incommensurate periodic potential may gain energy by an equilibrium geometric misalignment θ of the monolayer (see Fig. 3.2c). So far unnoticed, even if present in some published experimental results, we will show that this misalignment occurs also in incommensurate 2D colloidal monolayers.

Relative rotations between slider and substrate are known to affect the frictional properties of the interface. A paradigmatic example is that of a graphene flake sliding over graphite [111], where friction turns from high values in the aligned, and therefore commensurate and pinned case, to very small values when the flake is rotated away from commensuration. In genuinely incommensurate geometries one may be led to think that relative rotations should not be important in determining the dissipative properties of the sliding interface. Our simulations show instead that the dynamic friction can increase by a significant factor at the energetically favourable misalignment θ_{opt} with respect to the aligned case $\theta = 0$, considered for example in Ref. [131].

The second main issue we address in this Chapter is the nature of static friction against sliding of a 2D lattice onto a 2D incommensurate corrugation. An interesting experimental observation was the reduction by one order of magnitude of the static friction force F_s in incommensurate monolayers with respect to commensurate ones (see Fig. 3.3). This aspect was further investigated in realistic numerical simulations by Vanossi [131] and co-workers, who found a "superlubric" state with vanishingly small values of F_s for small values of U_0, which changed into a pinned state of the monolayer, where F_s becomes finite, above a certain threshold substrate corrugation. However they did not perform a detailed investigation of the transition. The reference point for our understanding is the 1D case, epitomized by the so-called Frenkel-Kontorova (FK) model, consisting of a harmonic chain of classical point particles in a static sinusoidal potential, an idealized system whose physics has been very widely studied and understood [99]. In 1D, the incommensurability between interparticle spacing and sinusoidal potential wavelength gives rise to a potential-induced deformation of the chain particle position, that can be described by a deformation of the chain's phase $\Phi(x)$ relative to that of the potential, from the non-interacting straight line of slope $(\rho - 1)$ to a staircase with the same mean slope but formed by nearly
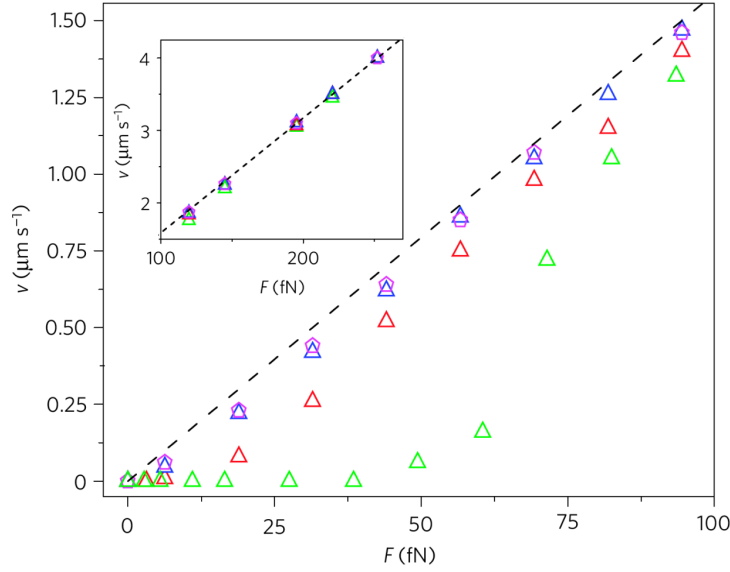
Figure 3.3: Colloidal monolayer center-of-mass velocity v as a function of the external driving F obtained in the experiment by Bohlein et al. [120]. Different colors correspond to different interface geometries: commensurate $\rho = 1$ (green triangles), incommensurate $\rho = 0.912, 0.842$ (red and blue triangles), and for a quasiperiodic substrate (magenta pentagons). The depinning force at which the monolayer is set into motion is below the experimental resolution incommensurate conditions.

horizontal, approximately constant phase terraces. These commensurate domains are separated by steps in the relative phase, often called solitons (or kinks) and antisolitons (or antikinks), where most of the misfit stress is concentrated. This 1D system is known to display a remarkable dynamical phase transition, first described by Aubry [101]. When the corrugation is weak, below a critical magnitude, when the soliton widths are comparable to or larger than that of terraces and the overall phase modulation is small, the FK chain exhibits no pinning, the static friction is zero. In this regime one finds particles at all potential values, and all possible phases of the chain particles are accessible in dynamics. Since the total potential energy is independent of the phase, $\delta E / \delta \Phi = 0$, the chain as a whole can be displaced by any infinitesimal force, a state that has been dubbed "superlubric" [102]. However, above a critical corrugation magnitude, whose value depends on precise parameters and incommensurability, the chain develops a nonzero static friction through the continuous "Aubry" phase transition. The essence of the Aubry transition is that the probability to find a particle exactly at a potential maximum drops mathematically to zero (of course at $T = 0$). Thus, even if $\delta E / \delta \Phi$ is still zero, this new dynamical constraint limits phase-space accessibility, breaking ergodicity in a way similar to a glass transition, with the onset of static friction and of chain pinning against free sliding. This transition is of a dynamical nature, so that even if the step-terrace deformation of the chain's phase $\Phi(x)$ becomes more marked in the pinned state, it still remains similar in nature to the superlubric one. Although suggestive, the static structure difference between the two does not reveal the essence of the transition. A more relevant signature is provided by the sliding friction. In the superlubric state, sliding of the chain occurs under any applied force however small, and can be envisaged as a state of flow of the solitons. Soliton motion causes dissipation, increasing with speed in correspondence with increasing emission of phonons. In the pinned state, chain sliding occurs only once the static

friction force is overcome, at which point the sliding dynamics becomes generally quite different from the superlubric state.

In view of this well-known 1D case, it is physically clear that a qualitatively similar state of affairs should also occur in 2D incommensurate sliders. That is actually a case much more relevant in practice, where one expects free, superlubric sliding for weak corrugation, and pinning with stick-slip for strong corrugation. Superlubricity is documented in several real 2D systems. Very small values of the static friction force F_s were observed for a rotationally misaligned graphene flake sliding over graphite [111], the pinned configuration corresponding to the aligned, commensurate case. Superlubricity and consequent ultra-low dynamic friction has also been demonstrated or implied in a number of cases, such as also telescopic sliding among carbon nanotubes [152, 153], in cluster nanomanipulation studies [154, 155], and in the sliding of rare-gas adsorbates [156, 157]. However, there is no experimental case so far exhibiting a clear superlubric-pinned transition among 2D incommensurate sliders under fixed geometrical conditions. Experiments [120] and simulations [131] however indicated that the study of the transition from the superlubric to the pinned state, done at constant lattice mismatch, and at constant mutual alignment is potentially feasible for sliding colloid monolayers. The question we address here, only marginally touched upon so far [99] is whether at constant mismatch the weak- and the strong-corrugation regimes will again or will not be separated by a well-defined superlubric-pinned phase transition of the same type as that described by Aubry in 1D, the only case where a mathematical treatment has been worked out. Colloid monolayers offers the ideal chance to verify this point if not analytically at least numerically in a realistic and relevant case. For a 2D triangular crystal monolayer interacting with a mismatched rigid corrugation periodic potential the 1D soliton-terrace staircase is replaced by a 2D superlattice of nearly commensurate domains. The domains are separated by soliton (antisoliton) misfit dislocation lines, depending on the specific value of ρ, and of the misalignment angle. In triangular symmetry, three families of soliton lines, oriented at ± 120 degrees from one another, will generally coexist. The coincidence plot between the two lattices (monolayer and periodic corrugation) realizes a moiré pattern, consisting of a patchwork of nearly commensurate, roughly hexagonal domains separated by the soliton lines, which concentrate the mismatch of the two lattices [158]. Like in 1D, the sliding of the 2D monolayer enacts a "flow" of the solitons in the moiré pattern. The main questions which we will address are: (a) Is there a sharp superlubric-pinned transition in the sliding of incommensurate colloid monolayers for increasing corrugation strength? (b) Is this 2D transition continuous (as in 1D), or first order? (c) Does the spontaneous misalignment of the ground state affect the transition, and when so, to what effect? We will present simulations for a model incommensurate monolayer which show that: (a) Superlubricity is replaced by pinning through a sharp transition. (b) That transition is, at least for the set of parameters used, of first order rather than continuous. (c) Spontaneous rotations very definitely affect the transition point, decreasing its critical value of corrugation U_0.

3.2   Model and simulation protocols

The 2D colloidal layer is represented by classical particles interacting via a screened-Coulomb potential

$$U(r) = Q^2 \exp(-r/\lambda_d)/r, \tag{3.1}$$

where Q is the effective charge and λ_d is the Debye screening length. Typical experimental interparticle separation is $a_c \approx 5.7 \mu m \approx 30\lambda_d$, safely larger than the colloid radius $r \approx 2 \ \mu m$,

Model Expression	Typical Value
Viscous coefficient γ	6.3×10^{-8} kg/s
Length a_c	5.7 μm
Force $F = Qe^{-a_c/\lambda_D}/(\lambda_D a_c)$	20 fN
Energy $E = Fa_c$	1.1×10^{-19} J
Velocity $V = F/\gamma$	0.3 μm/s
Power $P = F^2/\gamma$	6.3×10^{-21} W
Time $t_0 = \gamma a_c/F$	18 s
Mass $m = \gamma^2 a_c/F$	1.1×10^{-6} kg

Table 3.1: Basic units for various quantities in our model and typical values mimicking the setup of Ref. [120].

defining the distance at which an additional hard-core repulsive term sets in. Due to the violent increase of the Coulomb interaction, colloids never approach very closely, allowing to treat the particles as point-like objects. The experimental laser-induced "corrugation" potential is modeled via a periodic function of amplitude U_0, periodicity a_l, and triangular symmetry

$$W(x,y) = -U_0 \frac{2}{9} \left[\frac{3}{2} + 2\cos\left(\frac{2\pi x}{a_l}\right)\cos\left(\frac{2\pi y}{\sqrt{3}a_l}\right) + \cos\left(\frac{4\pi y}{\sqrt{3}a_l}\right) \right].$$

We performed simulations both at fixed density, periodic boundary conditions (*pbc*), and in open boundary conditions (*obc*). In the latter case confinement of the purely repulsive particles is achieved by adding a global Gaussian force field of intensity A_G and large width σ_G, mimicking the profile of the laser spot. The resulting overall external potential is

$$V_{\text{ext}}(\mathbf{r}) = \exp(-r^2/\sigma_G^2)\left(-A_G + W(\mathbf{r})\right). \tag{3.2}$$

As suggested by experiments [120], both the confining amplitude A_G and the corrugation potential $W(\mathbf{r})$ are controlled by the same gaussian modulation. Simulations in *pbc* are performed by setting $A_G = 0$ and choosing a very large value of σ_G, so that $e^{-r^2/\sigma_G^2} \approx 1$ inside the supercell, effectively leading to $V_{\text{ext}} \approx W$. With these definitions the static Hamiltonian of a system of N_p particles reads:

$$H = \sum_{i=1}^{N_p} \left[V_{\text{ext}}(\mathbf{r}_i) + \frac{1}{2}\sum_{j\neq i} U(r_{ij}) \right]. \tag{3.3}$$

Neglecting the gaussian force field, it is useful to split the total energy per particle $\langle E_{\text{tot}} \rangle = E_{\text{tot}}/N_p$ into two contributions:

$$\langle E_{\text{tot}} \rangle = \langle W \rangle + \langle U_{\text{pp}} \rangle, \tag{3.4}$$

namely the periodic lattice energy part

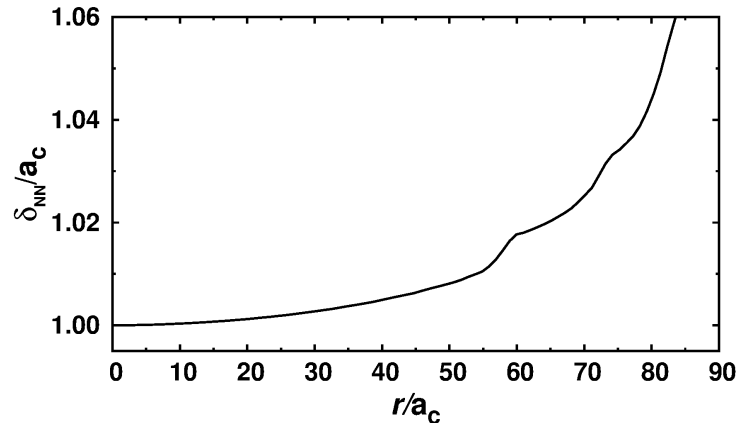$$\langle W \rangle = \frac{1}{N_p}\sum_{i=1}^{N_p} W(\mathbf{r}_i), \tag{3.5}$$

Figure 3.4: The average nearest-neighbor distance δ_{NN} scaled with respect to the central colloid-colloid mean spacing a_{c} of the circular island in *obc*, plotted as a function of the distance from the island center. The particle density slightly decreases towards the periphery as a result from the balance between the interparticle repulsion and the gaussian confining force-field.

controlled by the corrugation amplitude U_0, and the particle-particle repulsive interaction

$$\langle U_{\mathrm{pp}} \rangle = \frac{1}{2N_p} \sum_{i \neq j} U(r_{ij}). \tag{3.6}$$

The equation of motion for the j-th particle displacement $\mathbf{r}_j$ is

$$m\ddot{\mathbf{r}}_j + \gamma(\dot{\mathbf{r}}_j - \mathbf{v}_d) = -\nabla_{\mathbf{r}_j} \left[\sum_{i \neq j} U(r_{ij}) + V_{\mathrm{ext}}(\mathbf{r}_j) \right]. \tag{3.7}$$

In sliding simulations $\mathbf{v}_d$ represents the drift velocity of the experimental cell, giving rise to a Stokes' drag force $\mathbf{F}_{\mathrm{d}} = \gamma \mathbf{v}_{\mathrm{d}}$, experienced by each particle [131]. The overdamped dynamics typical of this system is achieved by adopting a sufficiently large value of the damping coefficient γ. We used $\gamma = 28$ in all simulations. Given the slow motion under study ($v_d \approx 1\ \mu\mathrm{m/s}$) and the relatively small volume fraction occupied by the particles, it is also appropriate to neglect hydrodynamic forces. We carried out mainly $T = 0$ simulations integrating the equations of motions using an adaptive Runge-Kutta algorithm. When needed, thermal (Brownian) motion is simulated by adding suitable random Gaussian forces in a Langevin approach. If not specified, all results are expressed in terms of the basic units defined in Table 3.1, where values are inspired by those in the experiment by Bohlein [120].

3.2.1 Open boundary conditions simulations

In *obc* equilibrium configurations were generated starting from a circular island cut out of a perfect triangular crystal at $a_{\mathrm{c}} = 1$ and fully relaxed inside the confining potential at zero corrugation $U_0 = 0$. We considered a large number of particles $N_p \approx 28,827$, fixing $Q^2 = 10^{13}$, $\lambda_{\mathrm{D}} = 0.03$, $\sigma_G = A_G = 1200$. With this choice, the colloidal monolayer's density, nearly constant in the central part, slowly decreases towards the periphery, as shown in Fig. 3.4. In order to fix ρ we considered as a reference the interparticle distance in the central homogeneous part of the

system $a_c \approx 0.983$. We then carried out damped-dynamics simulations at $T = 0$ increasing the corrugation U_0 in steps $\Delta U = 0.018$. We followed the same protocol starting from islands rotated at different initial misalignment angles θ_i, ranging between $0 \leq \theta_i \leq 30°$. From this procedure, we obtained energy curves, whose minima determined the optimal static configurations and equilibrium misalignment angle θ_{opt}. We note that in this process the final orientation θ_f of the island at the end of optimization is not identical to the initial angle θ_i; however, it usually remains very close. Results are then given as a function of $\theta = \theta_i$. All relaxed configurations with $\theta \neq \theta_{\mathrm{opt}}$ represent locally stable (and generally metastable) states of the system.

In real sliding experiments the driving force is the viscous drag exerted on each colloid by a slow fixed-amplitude oscillatory motion of the experimental cell. The slow time scale yields long time intervals with constant drag force. Our dynamical simulations were therefore carried out by applying to each particle the same driving force $F_d = \gamma v_d$, usually along the x axis. F_d was kept constant during a finite time t_F inversely proportional to the force value F_d itself (and thus the overall sliding speed). After this time, the force sign was reversed for the same time duration. The particle motion being overdamped, there are no effects of inertia. The product $F_d t_F$ was chosen so that an isolated unconfined particle would move by a few lattice spacings $F_d t_F / \gamma \approx 2 - 3 \, a_c$ typically.

When studying the sliding of the monolayer in *obc*, the Gaussian confining potential is kept fixed in time. Only the homogeneous central part of the island is sliding, whereas the boundary tends to remain pinned during the slow oscillatory cycle. In order to exclude undesired edge effects, we selected a square central region of size $80 \times 80 \, a_c^2$, containing $\sim 7,500$ particles. Aiming at describing steady-state sliding, we discarded an initial transient of approximately 30% of the simulation time and computed averages considering particles which at $t = 0$ were residing in this central block. Following Ref. [131], the dissipated friction power is calculated according to:

$$p_{\mathrm{fric}} = \mathbf{F_d} \cdot \langle \mathbf{v_{cm}} \rangle - \gamma |\langle \mathbf{v_{cm}} \rangle|^2 = (\gamma/N_p) \Sigma_i \langle |\mathbf{v_i} - \mathbf{v_{cm}}|^2 \rangle \tag{3.8}$$

where $\mathbf{v_{cm}}$ is the center-of-mass velocity, $\mathbf{v_i}$ is the velocity of particle i, and brackets denote steady-state averages. We obtained curves of p_{fric} versus θ by applying this procedure to each of the misaligned static configurations produced following the protocol described earlier. We verified that due to the relatively large size of the island and the short duration of the simulations the initial angular orientation of the island is preserved during the sliding trajectory (even at finite temperature).

3.2.2   Periodic boundary conditions simulations

Simulations in *pbc* were performed fixing $Q^2 = 10^{13}$, $\lambda_D = 0.03$, $A_G = 0$, and $\sigma_G = 10^{13}$, large enough to ensure $V_{\mathrm{ext}} = W$ inside the adopted supercells. The desired value of $\rho = a_l/a_c$ was set by choosing an appropriate value of a_l, while fixing a_c as our length unit. Any desired misalignment angle between the corrugation and the colloidal triangular lattices was implemented by means of a suitably chosen supercell, built using a standard procedure as follows [159]. The two lattices are defined by the pairs of primitive vectors $\mathbf{a}_1 = a_l(1,0)$, $\mathbf{a}_2 = a_l(0.5, \sqrt{3})$, and $\mathbf{b}_1 = a_c(\cos\theta, \sin\theta)$, $\mathbf{b}_2 = a_c(\cos(\theta+\pi/3), \sin(\theta+\pi/3))$. The overall supercell-periodic structure can be realized if four integers exist which satisfy the matching condition $n_1\mathbf{a}_1 + n_2\mathbf{a}_2 = m_1\mathbf{b}_1 + m_2\mathbf{b}_2$. The ensuing supercell is that of a triangular lattice of size $L = |m_1\mathbf{b}_1 + m_2\mathbf{b}_2|$, containing a total number of particles $N_p = m_1^2 + m_1 m_2 + m_2^2$. In practice we fixed $a_c = 1$ and varied $n_{1,2}$, $m_{1,2}$ in search of structures with a mismatch $\rho = a_l/a_c \approx 3/(1+\sqrt{5})$ – close to the experimental values of Ref. [120] – and θ near the desired value, with the obvious additional constraint that the

(n_1,n_2)	(m_1,m_2)	ρ	θ	N_p
(96,96)	(89,89)	0.92708333	0	7,921
(105,59)	(107,71)	0.92705245	2.54°	20,701
(96,72)	(100,54)	0.92705012	5.07°	18,316
(78,74)	(59,103)	0.92705113	9.78°	17,332

Table 3.2: Parameters of the four supercells adopted for the simulations in *pbc* (see text for definitions). The supercells are determined following the procedure outlined in the text. For $\theta = 0$, the adopted mismatch $\rho = a_\mathrm{l}/a_\mathrm{c} = 89/96$ corresponds to the sixth approximation in the continued fraction expansion of $3/(1 + \sqrt{5})$.

number of particles N_p should not be too large. We considered the aligned configuration $\theta = 0$, plus the following misaligned configurations: $\theta \simeq 5°$, $\theta \simeq 10°$ and $\theta_\mathrm{opt} \simeq 2.54°$. The latter chosen close to the Novaco-McTague (NM) equilibrium misalignment angle $\theta_\mathrm{NM} \simeq 2.58°$ predicted by weak-coupling elastic theory [150, 151]. Table 3.2 collects the adopted supercell parameters.

To identify the distorted colloid lattice configuration of lowest energy in presence of the corrugation we carried out $T = 0$ damped-dynamics simulations testing different protocols. In the first we increased the corrugation amplitude U_0 in steps $\Delta U = 0.018$ – eventually reduced near transition critical points – then reversing the sign of ΔU and decreasing U_0 back to zero in order to check for hysteresis across structural transitions. The maximum values of the corrugation considered is $U_\mathrm{max} = 1$. In the second protocol we switched on abruptly the corrugation at given values of U_0 with the monolayer initially either undistorted or in a configuration previously fully relaxed at U_max. Eventually the lowest energy configurations were always obtained using the first protocol described above.

The depinning of the monolayer was studied by applying to each colloid a driving force F_d, generally along a high-symmetry direction of the laser substrate potential. For a given value of U_0, the single particle barrier for the onset of motion is $F_{s1} = 8\pi U_0/9a_l$. The external force was then increased adiabatically in steps $\Delta F = 0.002$, much lower than the lowest value of F_{s1} considered. The simulations duration was fixed in such a way that a single free particle would slide by a total distance of $10\,a_c$. A colloid configuration was classified as sliding when the procedure produced a final center-of-mass displacement $\Delta x_\mathrm{cm} \gtrsim 2\,a_c$.

3.2.3 Moiré pattern geometry

Preliminary to presenting our results, it is useful to recall a few geometrical concepts. A given mismatch ρ and misalignment angle θ induce a specific moiré pattern of the colloidal crystal. The moiré superstructure of an undistorted monolayer is entirely described by its overall periodicity L and its orientation angle ψ relative to the substrate. Similar to the beats of two sinusoids in one dimension, the values of ψ and L are governed by the difference $\mathbf{G} - \mathbf{G}'$ between the smallest reciprocal lattice vectors of the monolayer and optical potential. The relations connecting ρ and θ to ψ is given by [160]

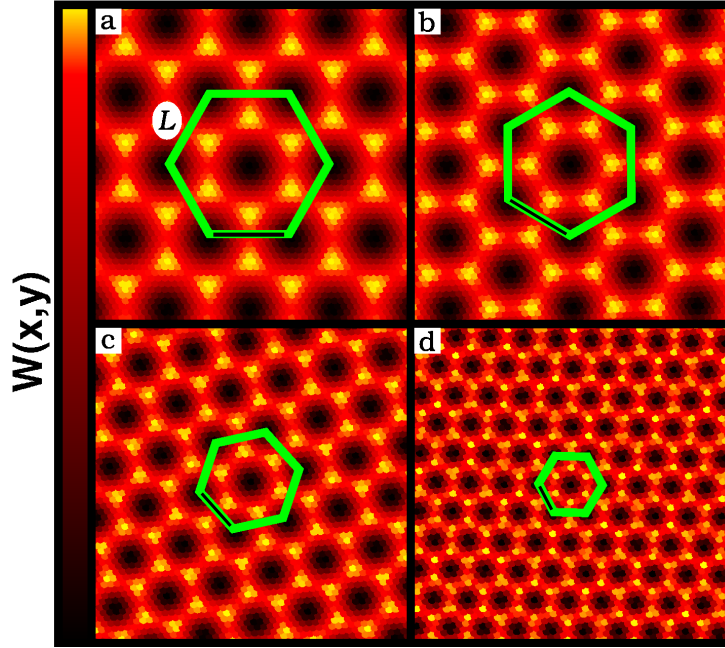$$\cos \theta = \rho^{-1} \sin^2 \psi + \cos \psi \sqrt{1 - \rho^{-2} \sin^2 \psi}, \tag{3.9}$$

Figure 3.5: Examples of the moiré patterns obtained at $\rho \approx 0.927$ for misfit angles (a) $\theta = 0$, (b) $\theta_{\mathrm{opt}} \approx 2.54°$, (c) $\theta \approx 5°$, and (d) $\theta \approx 10°$. A small portion of the simulation supercells in *obc* is displayed, containing an undistorted monolayer. The particles' colors reflect the underlying corrugation potential $W(x, y)$: dark for potential minima, bright for maxima. According to Eq. (3.9), at $\theta \simeq 2.54°$ the moiré orientation is $\psi \simeq 30°$. As θ increases the superstructure periodicity shrinks rapidly and rotates all the way to $\psi \simeq 60°$ (c).

which, for $\rho \simeq 1$ produces a rapid reorientation of the moiré pattern for small changes of $\theta \simeq 0$, as shown in Fig. 3.5, where the moiré of the incommensurate interface is visualized by coloring each colloids according to the local value of the underlying corrugation potential $W(x, y)$. As the moiré superlattice rotates by ψ, its spacing L also decreases [161] from the aligned value of about $L = a_{\mathrm{c}}\rho/(1 - \rho)$ to the rotated value $L' = a_{\mathrm{c}}/\sqrt{1 + \rho^{-2} - 2\rho^{-1}\cos\theta}$.

3.3   Frictional dissipation at equilibrium misalignment

A long-known theoretical result [151] suggests that a harmonic monolayer subject to an incommensurate periodic potential of weak amplitude U_0 may partly convert the misfit compressional stress to shear stress by an equilibrium geometric misalignment of the monolayer (see Fig. 3.2c) through a small rotation angle

$$\theta_{\mathrm{NM}} = \arccos\left(\frac{1 + \rho^2(1 + 2\delta)}{\rho[2 + \delta(1 + \rho^2)]}\right), \tag{3.10}$$

whose energy-lowering effect originates from a better interdigitation of the two lattices. Independent of U_0, the rotation angle is nonzero in this approximation provided the transverse 2D sound velocity c_T is sufficiently smaller than the longitudinal c_L, precisely if $\delta = (c_L/c_T)^2 - 1 > \rho^{-1}$. While this kind of rotated epitaxy has been addressed experimentally [163, 164] and theoretically [165] for adsorbed rare-gas monolayers, its possible presence in colloidal monolayers was
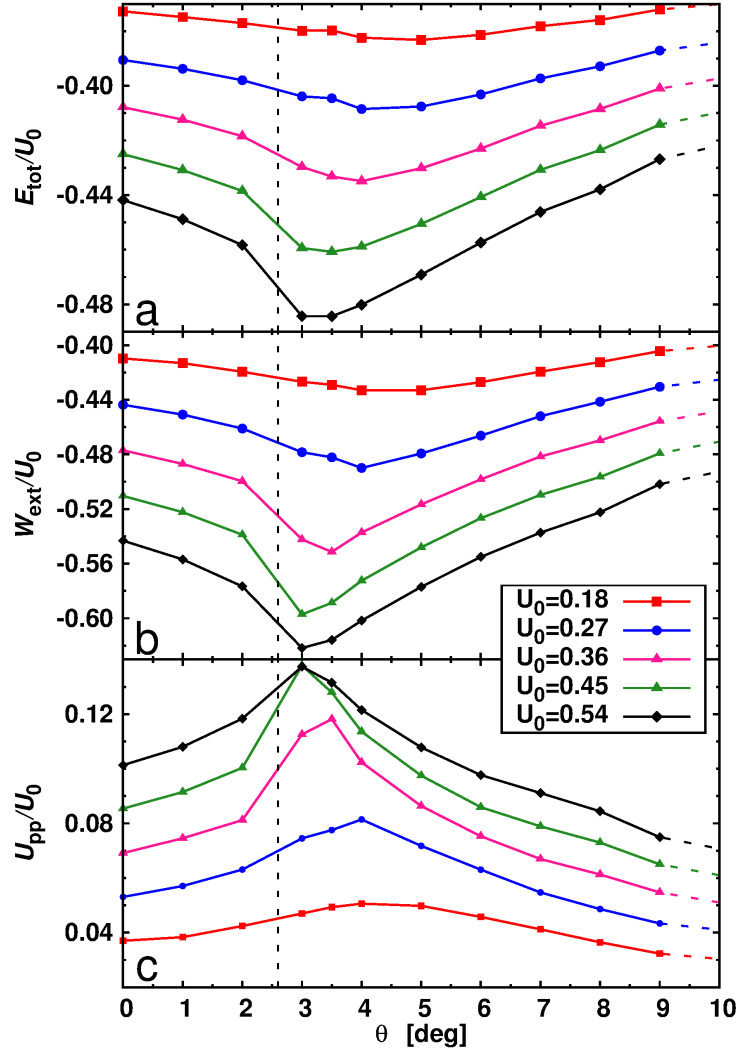
Figure 3.6: Relative static energy of structure-optimized colloid islands in *obc* as a function of the trial rotation angle θ. (a) Total energy per particle $\langle E_{\text{tot}} \rangle$. (b) Periodic-potential (corrugation) contribution $\langle W \rangle$ to $\langle E_{\text{tot}} \rangle$. (c) Interparticle interaction contribution $\langle U_{\text{pp}} \rangle$ to $\langle E_{\text{tot}} \rangle$. Curves correspond to increasing corrugation amplitude $U_0 = 0.18 - 0.54$. Energies are measured relative to that of the colloidal monolayer at rest and at $U_0 = 0$. Dashed line: ideal NM angle, Eq. (3.10), $\theta_{\text{NM}} \approx 2.6°$.

so far unsuspected. More importantly in the context of sliding friction, the tribological impact of an *equilibrium* geometrical misalignment is unexplored in any incommensurate system. The externally forced rotation turning a *commensurate* layer into incommensurate is well known to reduce friction, as exemplified by the sliding of graphene flakes on graphite [111, 116]. Different as these two cases are, a possible expectation might be that the equilibrium geometry, alignment of commensurate layers, or misalignment of incommensurate layers, should always exhibit a higher friction relative to forcedly rotated ones, since the optimal $T = 0$ geometry must in every case correspond to a closer interdigitation of the two lattices.

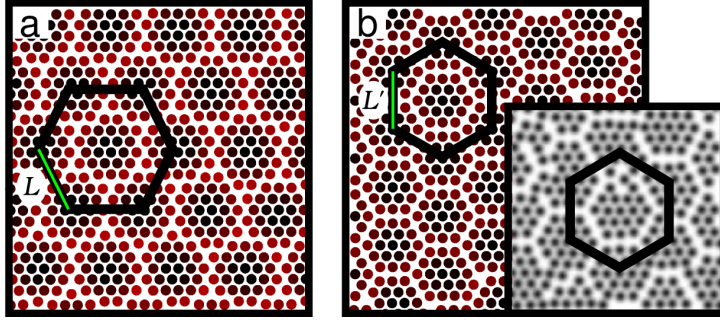First, let us consider structural alignment. Here we shall focus for specificity on the underdense

Figure 3.7: Equilibrium configurations obtained in *obc* for $\rho \simeq 0.83$ and $U_0 = 6.3$. (a) Unrotated $\theta = 0$; (b) optimally rotated $\theta_{\mathrm{opt}} = 7°$. Dark/light colloids enjoy best/worse W. Only the central part of the island, optimized in *obc*, is shown. (c) Experimental geometry for the same ρ, adapted from Ref. [162], where both the moiré angles and spacing compare directly with (b) rather than (a). The experimental setup corresponds to a softer colloidal crystal at a larger lattice spacing $a_c \simeq 6.5$ μm, with respect to Ref. [120]. In this case a more appropriate value for the basic energy unit is $E \simeq k_B T_{\mathrm{room}} = 4.1 \times 10^{-21}$ J.
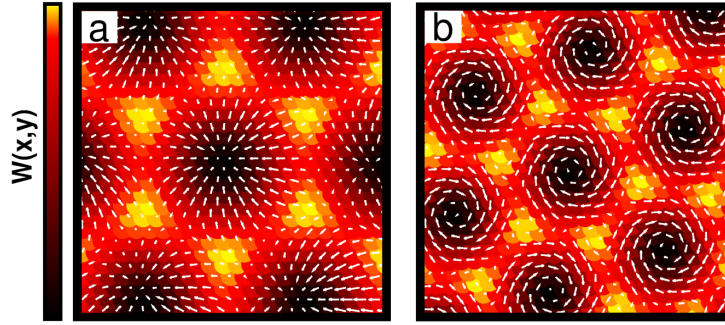

Figure 3.8: Moiré patterns of the particle monolayer's central region as obtained in *obc* for $\rho = 0.927$, $U_0 = 0.27$, (a) for $\theta = 0$ (moiré angle $\psi = 0$) and (b) for the optimal $\theta = 4°$ (moiré angle $\psi \approx 15°$). Each dot indicates a particle in the unrelaxed configuration, colored according to the local corrugation potential $W(\mathbf{r})$: dark for potential minima, bright for maxima. White arrows show the displacements of each particle from the ideal triangular lattice to the fully relaxed configuration, magnified 15 times. The compression-dilations at $\theta = 0$ are turned into largely shear, vortex-like displacements at $\theta_{\mathrm{opt}} = 4°$.

(less particles than substrate potential minima) incommensurate case $\rho = 3/(1 + \sqrt{5}) \simeq 0.927$, and consider simulations performed at zero temperature, since the results are clearer and require less statistics in this limit. In Appendix B we report both about finite temperature simulations, which are otherwise not essentially different, and we briefly discuss the physics with different values of $\rho \neq 1$ including $\rho > 1$, which is qualitatively similar. Figure 3.6a shows the total energy per particle of the colloidal monolayer in *obc* as a function of the misalignment angle θ, obtained for a range of corrugations $U_0 = 0.1 - 0.6$. The total energy minimum versus θ confirms the structural misalignment angle at equilibrium, with a magnitude in the range $3° < \theta_{\mathrm{opt}} < 5°$ (depending on the optical lattice strength U_0). Demonstrating the robustness of this small rotation, a similar result was obtained also in *pbc* simulations where a 2D colloid lattice initially aligned at $\theta = 0$ was found to be misaligned, with a small rotation angle $\theta_{\mathrm{opt}} \simeq 2.3°$ after an
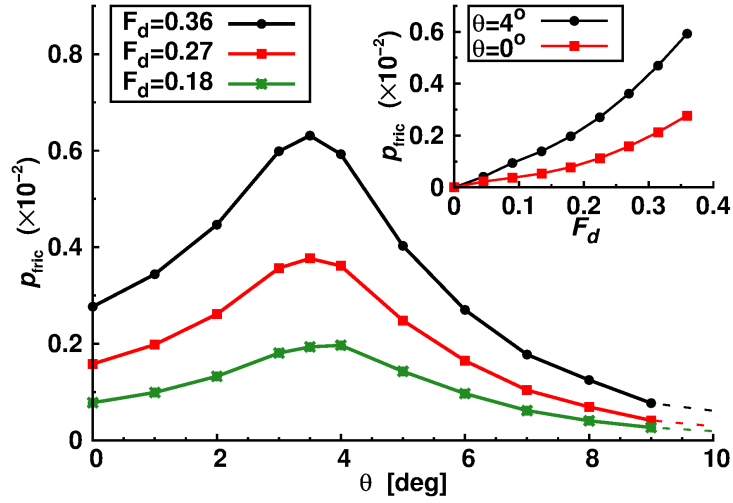
Figure 3.9: Dissipated friction power p_{fric} as a function of the trial misalignment angle θ ($U_0 = 0.27$). Three curves are reported corresponding to increasing values of the driving force $F_d = 0.18,\ 0.27,\ 0.36$. The inset shows p_{fric} as a function of F_d for two values of θ.

annealing procedure. This rotation occurred spontaneously during the simulation at the cost of creating the dislocations required by the *pbc* constraints (see Appendix B). These structural results compare instructively with those expected from the harmonic model [151]. In our case a 2D phonon calculation for the monolayer yields a sound velocity ratio $c_L/c_T = 1.806$, larger than the theoretical threshold value $(1 + \rho^{-1})^{1/2} \simeq 1.442$. The corresponding theoretical misalignment $\theta_{\text{NM}} \simeq 2.6°$ is in qualitative agreement with the more realistic simulation result. Figure 3.6b,c shows how the two pieces which compose the total energy per particle $\langle W \rangle$ and $\langle U_{\text{pp}} \rangle$ behave. Misalignment raises the interparticle energy, but that cost is overcompensated, by a factor 2, by a corrugation energy gain. The incommensurate colloid static equilibrium structure is misaligned because that permits a better interdigitation with the optical lattice.

Even if our predicted misalignments are small, their experimental existence is easily revealed, because the rotation angle θ between two lattices is highly amplified by the moiré pattern, which rotates relative to the periodic potential lattice by an angle ψ, given in Eq. (3.9). As an example, Fig. 3.7 reports the structures of the artificially unrotated and of the optimally rotated ($\theta_{\text{opt}} = 7°$) configurations calculated for $\rho \simeq 0.83$ and $U_0 = 6.3$ (parameters believed to be appropriate to experiments in Ref. [162]) in comparison with one another and with the corresponding experimental structural moiré. Both the orientation and spacing of Fig. 3.7c agree with the $\theta_{\text{opt}} = 7°$ but not with the $\theta_{\text{opt}} = 0$ pattern, proving that the misalignment was actually present in that experiment.

The particle static displacements associated with the optical lattice potential are also enlightening. Figure 3.8 shows the moiré pattern of a small portion of the monolayer island ($\rho = 0.927$, $U_0 = 0.27$) for $\theta = 0$ and for $\theta_{\text{opt}} = 4°$, corresponding to a moiré angle $\psi \approx 15°$. Particle displacements, designated by arrows, change from radial longitudinal compression-dilations to mixed shear-longitudinal, vortex-like displacements upon optimal misalignment. A large 2D bulk modulus and a weak shear rigidity of the crystalline monolayer are crucial factors increasing the extent of the shear distortions, therefore enhancing the lattice misalignment.

We now come to our second point, i.e., the forced sliding of the particle monolayer over the
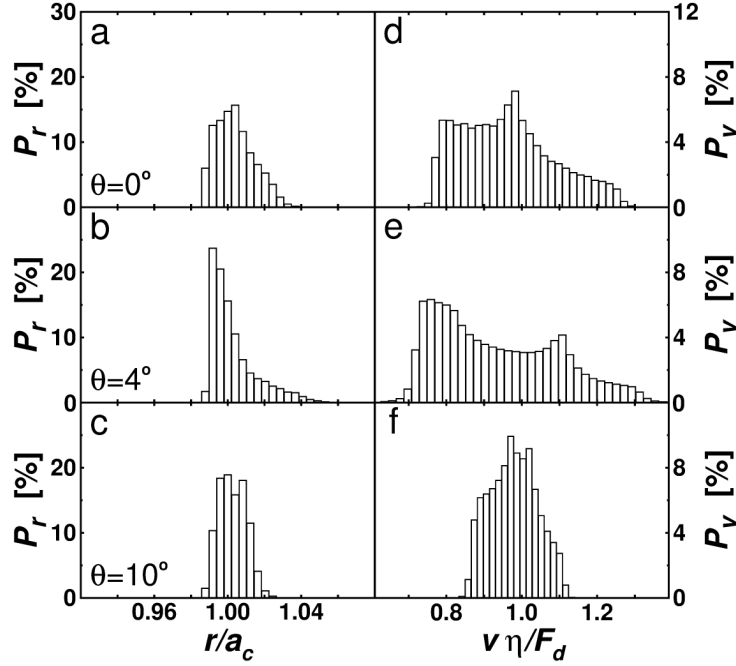
Figure 3.10: (a-c) The distribution P_r of nearest-neighbor distances in the static relaxed configurations ($F_d = 0$, $U_0 = 0.27$) at rotation angles $\theta = 0$, $\theta = \theta_{\mathrm{opt}} = 4°$, and $\theta = 10°$. (d-f) Corresponding velocity distribution P_v of particles sliding under a driving force $F_d = 0.36$.

periodic corrugation and the associated frictional losses. The shear distortions and the corresponding increased interdigitation at the optimal misalignment angle θ_{opt} are expected to affect the sliding of the particle lattice over the periodic potential. Sliding is realized by a flow of the soliton superstructure, accompanied by dissipation as part of the work goes into soliton-related time-dependent distortions of the 2D lattice. That work will change once the nature (longitudinal to shear), orientation (0 to ψ), periodicity (L to L') change with θ (0 to θ_{opt}). We determine the magnitude of the expected friction change by simulating the overdamped sliding dynamics of the *obc* island over a range of θ values, so as to assess the frictional effect of misalignment near its optimal value. We applied a driving force F_d acting on each particle, slowly varying to-and-fro as a function of time, mimicking the experimental drag force γv_d induced by a fluid of viscosity γ and slowly back and forth time-dependent speed v_d. Here we will consider F_d applied along the high symmetry direction of the substrate potential Eq. (3.2) coinciding with the x-axis of our reference frame. In Appendix B it is shown that the results are actually independent on the orientation φ of the driving force. We note that despite a nonzero torque, generally present for all preset angles that differ from θ_{opt} (and from zero) the misalignment angle did not have the time to change appreciably in the course of the simulation.

Figure 3.9, our main dynamical result, shows that friction is increased by a very substantial factor by misalignment relative to alignment, reaching a maximum of about two at the optimal angle θ_{opt}, subsequently dropping for larger angles where the energy gain and static distortion magnitude also drop. The physical reason for the frictional peak at θ_{opt} can be further appreciated by looking at the particles' steady state velocity distribution P_v and at the corresponding static interparticle spacing distribution (at zero velocity) P_r, both shown in Fig. 3.10 for increasing θ. The important points here are that small interparticle distances are energetically costly, and
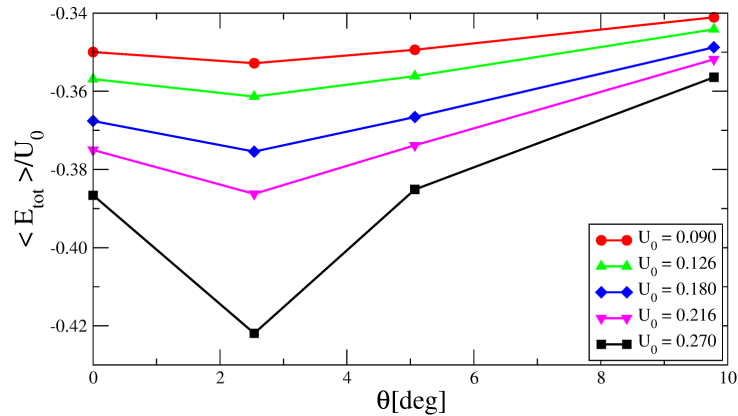
Figure 3.11: The total energy $\langle E_{\text{tot}} \rangle$ per particle of the colloidal monolayer optimized in *pbc* at $\rho = 0.927$, for a few misalignment angles θ. Curves correspond to increasing corrugation amplitude $U_0 \approx 0.1 - 0.3$. Energies are measured relative to that of the perfect crystal at $U_0 = 0$, and are scaled with respect to U_0 for better comparison.

that a large spread of velocities relative to the center-of-mass denotes larger frictional dissipation, according to the RHS of Eq. (3.8). At perfect alignment, short distances (colored column) are very frequent, which is energetically costly. At the same time the spread of velocities is moderate and so is friction. In the optimally misaligned case θ_{opt} instead, the shortest distance becomes less frequent, thus reducing energy as we already know. At the same time however P_v develops longer tails at lower and higher particle velocities, both of which increase friction. At $\theta > \theta_{\text{opt}}$ finally the velocity spread drops and so does friction, the monolayer sliding less and less affected by corrugation.

3.4   Pinning transition

Here we discuss the transition from the free-sliding, zero static friction state of incommensurate monolayers to the pinned, finite static friction state. We will begin by describing the evolution of the ground state configuration of our model underdense colloidal monolayer as a function of increasing corrugation strength U_0, where a first order structural transition occurs. In order to avoid complications introduced by the inhomogeneity of the circular island in *obc* we will consider simulations performed in *pbc* and at $T = 0$, obtained at fixed incommensurability $\rho \simeq 0.927$ and for a grid of angular misalignment angles θ, chosen guided by the more detailed angular dependence of the total colloid energy in the optical lattice investigated in the previous section. We will then discuss the implications of such structural phase transition on the static friction force of the monolayer. Finally we will consider the effects of different misfit orientation angles of the interface.

3.4.1   Corrugation driven structural phase transition at pinning

Figure 3.11 shows the total potential energy per particle $\langle E_{\text{tot}} \rangle$ as a function of U_0 and for small θ values. The lowest energy is seen to occur at a small but finite $\theta_{\text{opt}} = 2.54°$, in agreement to the theoretical, weak-coupling misalignment θ_{NM} suggested by the theory of orientational epitaxy [151, 166, 167]. We wish to understand now what happens to the colloid structure, energy,
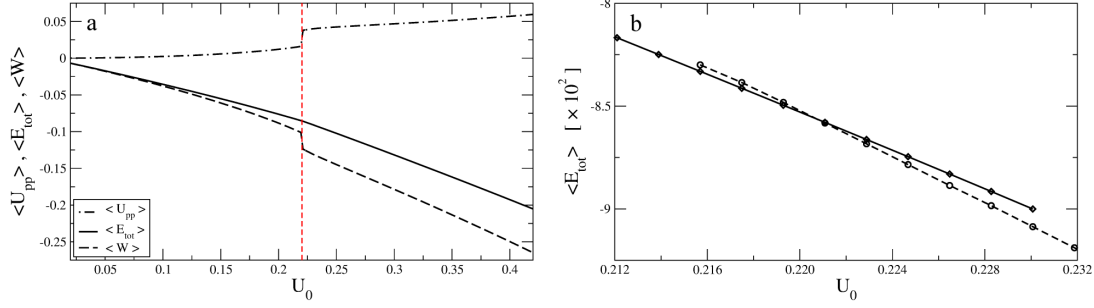
Figure 3.12: (a) The total potential energy $\langle E_{\text{tot}} \rangle$ per particle, its periodic-potential (corrugation) contribution $\langle W \rangle$, and interparticle contribution $\langle U_{\text{pp}} \rangle$ as a function of the corrugation U_0 for the optimally misaligned colloidal monolayer ($\theta = \theta_{\text{opt}} = 2.54°$). The sudden drop of $\langle W \rangle$ and the corresponding jump of $\langle U_{\text{pp}} \rangle$ signal a first-order transition, taking place at constant incommensurability and misalignment angle. As will be shown later, the weak-corrugation phase is unpinned and superlubric, the strong-corrugation phase is pinned by a finite static friction. (b) The intersection between the total energy branches representing the superlubric (small U_0) and statically pinned (large U_0) structures. Like in all first-order transitions, each phase survives in metastable state beyond the transition point.
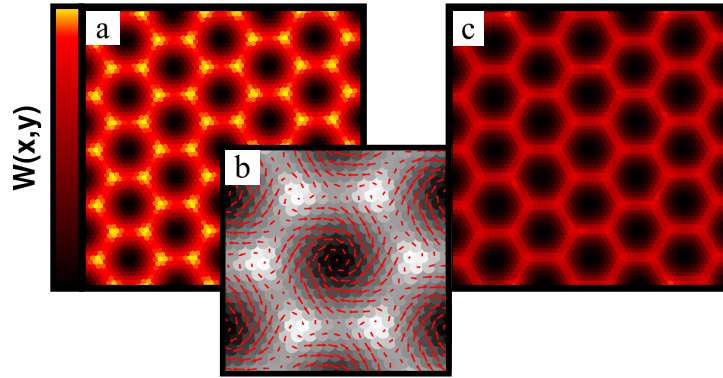

Figure 3.13: The moiré patterns of the fully-relaxed incommensurate colloid monolayer at $\theta_{\text{opt}} = 2.54°$. A small portion of the simulation supercell is shown. Each dot represents a particle, colored according to the local corrugation potential $W(x, y)$: dark for potential minima, bright for maxima. (a) The optimal weak-corrugation configuration ($U_0 = 0.108$). (b) Zoomed-in region with arrows highlighting the particles' displacements (magnified 20×) from the ideal triangular lattice to the fully-relaxed configuration. Vortex-like displacements tend to locally rotate the domains back into registry with the substrate. (c) The optimal strong-corrugation state ($U_0 = 0.395$). The hexagonal domains appear now fully commensurate, and separated by sharp domain walls. Here most colloids fall very close to a potential minimum.

and eventually to the static friction as a function of U_0 at $\theta = \theta_{\text{opt}}$. Figure 3.12a displays the two contributions to the total energy $\langle E_{\text{tot}} \rangle = \langle W \rangle + \langle U_{pp} \rangle$. The total energy evolution is smooth until $U_0 = 0.22$ where we observe a sudden decrease in $\langle W \rangle$ accompanied by an increase of the repulsive term. This indicates a first-order structural transition in the monolayer. Figure 3.13a displays the θ_{opt} moiré patterns of the relaxed monolayer for $U_0 = 0.108$, a weak corrugation well below the first-order transition. For this weak corrugation the triangular colloidal crystal is only slightly affected by the substrate potential. Panel 3.13b illustrates the corresponding colloid
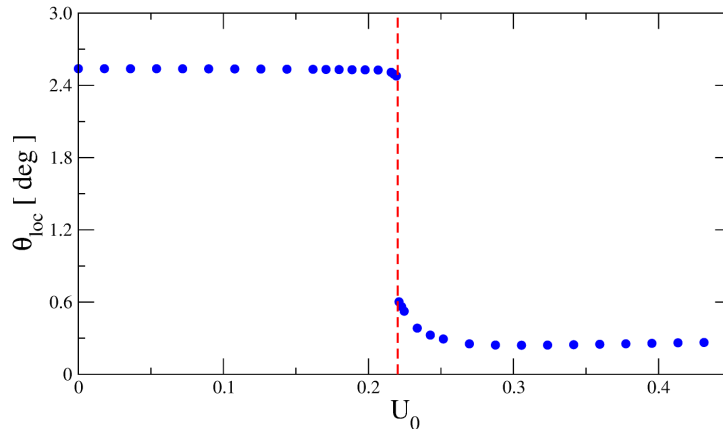
Figure 3.14: The average local orientation of the monolayer θ_{loc} (see Eq. (3.11)) plotted as a function of corrugation. The vertical dashed line separates the weak-corrugation and the strong-corrugation phases.

displacements relative to the rigid unperturbed crystal ($U_0 = 0$). The misalignment of the colloidal crystal over the lattice corrugation is only slightly modulated by the vortex-like distortion reflecting the shear nature of the solitons, whose width is larger than their separation. Panel 3.13c portrays the moiré pattern for $U_0 = 0.395$, a strong corrugation well above the transition. A hexagonal superlattice of domains of colloids locally commensurate with the corrugation are separated by "atomically" sharp antisolitons lines.

It is also instructive to look at the average local orientation of the monolayer (see Fig. 3.14), defined as

$$\theta_{\mathrm{loc}} = \frac{1}{M} \sum_{\langle i,j \rangle} \mathrm{mod}\left(\theta_{ij}, \frac{\pi}{3}\right), \tag{3.11}$$

where the sum is over all M pairs $\langle i,j \rangle$ of nearest neighbor particles, and θ_{ij} is the angle between the relative position vector $\mathbf{r}_i - \mathbf{r}_j$ and the x-axis. At the transition, the commensurate domains realign significantly with the triangular potential. Figure 3.12b shows a crossing of the total energies of the weak-corrugation and the strong-corrugation phase at the transition point, as a function of U_0. A separate stability analysis shows that each phase survives as a metastable state over a finite corrugation interval on the "wrong" side of U_c, eventually collapsing at its respective spinodal point.

3.4.2 Static friction and superlubricity

We now come to the static friction force F_{s} of the colloid monolayer, the main interest of the present investigation. It is obvious that the first-order structural transition uncovered in the previous section must affect it. Figure 3.15 shows the static friction force F_{s} obtained by simulation with $\rho \simeq 0.927$ and $\theta_{\mathrm{opt}} = 2.54°$ as a function of the corrugation strength U_0. For weak corrugation $U_0 < U_c$ the static friction is small below the error. In this regime the colloid monolayer slides freely already at the smallest applied force, demonstrating that the incommensurate state is indeed superlubric. [1]. At the transition corrugation the static friction suddenly jumps

---

[1]Strictly speaking, since we are adopting *pbc*, our systems are commensurate and therefore ultimately pinned. A fine search at $U_0 = 0.216$, below and close to U_c, shows that the static friction force is indeed finite there, being
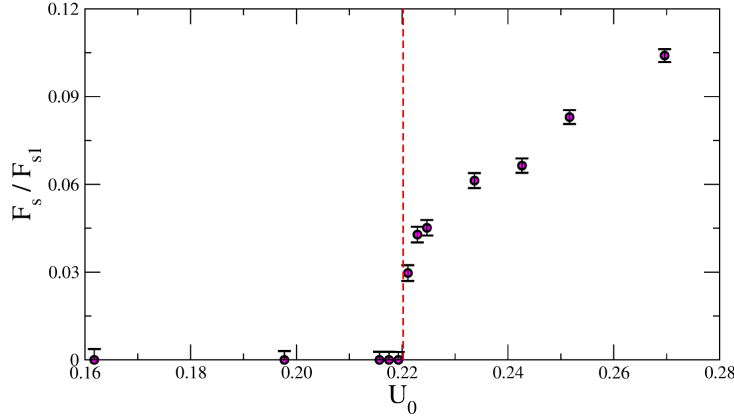
Figure 3.15: The static friction force F_s of the $\rho \simeq 0.927$ colloidal monolayer, normalized to the single-particle barrier F_{s1}. The dashed line indicates the transition point corrugation $U_c = 0.22$ where the colloid monolayer suddenly locks onto the corrugation. The error bar is defined by the force increment $\Delta F = 0.002$ used in the simulation protocol.

to $0.03F_{s1}$. The monolayer becomes pinned, and the superlubricity is lost through a first-order transition. Unlike 1D, where the pinning transition was of second order, here it coincides with the first-order structural transition.

Leaving the transition order aside, it is easy to show that the underlying reason for pinning in the present 2D case is still quite similar to that in the 1D FK model, namely a collapse of the dynamically-available phase space. In 1D, that collapse was signaled by the simultaneous collapse of the probability for any particle to occupy a local potential maximum. In the present 2D case we can similarly investigate the probability for colloids to occupy, in their optimal configuration, the (x, y) triangular region above the saddle-point among adjacent local minima of the corrugation potential. If the analogy with 1D holds, a superlubric, ergodic state should populate abundantly this region, while in a pinned, broken-ergodicity state, the population probability at the center of these regions should collapse to zero, and even remain zero across a whole neighborhood of the maximum – a finite "disorder parameter" [99]. Indeed, as shown in Fig. 3.16a, at the first-order superlubric-pinned transition, these repulsive regions around the maxima depopulate dramatically. This is represented pictorially in Fig. 3.16c-f, reporting the particles' positions folded in one primitive cell of the corrugation lattice (see Fig. 3.16b). These properties represent a 2D version of the disorder parameter Ψ, which measures the width of the largest gap appearing in the hull function at the Aubry transition in the incommensurate 1D FK model [99]. It should be noted that in the pinned colloid state the static friction force remains well below the single-colloid limit value F_{s1}, as shown in Fig. 3.15. The reason for this lower static friction is that of course the monolayer sliding is still strongly collective, whereby the particles surrounding a given particle attempting to cross a forbidden region actually help by pushing it across the barrier.
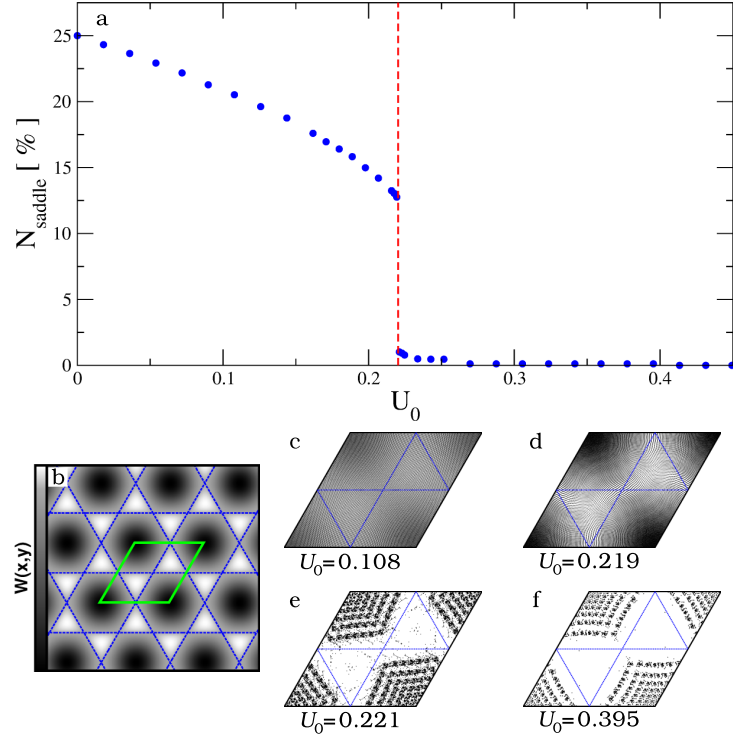
Figure 3.16: (a) The fraction of colloidal particles which sample repulsive regions of the substrate potential, i.e. those positions where $W(x, y)$ exceeds the saddle energy, plotted as a function of the corrugation strength U_0. (b) The triangular potential $W(x, y)$. Dark and bright regions correspond respectively to minima and maxima, isolines are reported at the saddle-point value and a primitive cell is highlighted at the center of the density plot. (c-f) The positions of the particles reported inside one primitive cell of the substrate potential. Configurations are shown for different corrugation values: (c) $U_0 = 0.108$ – superlubric phase; (d) $U_0 = 0.219$ – just below the transition; (e) $U_0 = 0.221$ – just above the transition; (f) $U_0 = 0.395$ – well above the transition.

3.4.3   Static friction at different misalignments

An interesting aspect of the transition to the 2D locked state is its dependence on the misfit angle θ. As discussed in Sect. 3.3, at the optimal orientation θ_{opt} the colloidal crystal deforms mainly via the softer transverse modes, facilitating the interdigitation with the substrate. If the monolayer is rotated away from θ_{opt} its grip of the corrugation weakens: as a result the superlubric state survives up to a larger corrugation strength U_0. As the simplest example, consider the aligned monolayer configurations obtained at $\theta = 0$. Figure 3.17a shows the evolution of the number of particles sampling repulsive regions of the corrugation potential. In this case too we identify a corrugation $\tilde{U}_c = 0.391$ above which the monolayer pins, again with a first-order transition. As expected, the transition corrugation is larger – almost a factor of two – than that at the optimal misalignment, $U_c = 0.22$. Figure 3.17b shows the static friction force F_s across the structural transition. The aligned monolayer is superlubric up to $\tilde{U}_c$, where we observe a sudden surge of

---

$0.0005 < F_s < 0.001$. However, this "pinning transition" is marked by a sudden increase in F_s by two-three orders of magnitude when increasing U_0 above the critical value U_c. On the opposite side, for $U_0 \ll U_c$, F_s is so small that it is quite hard to measure.
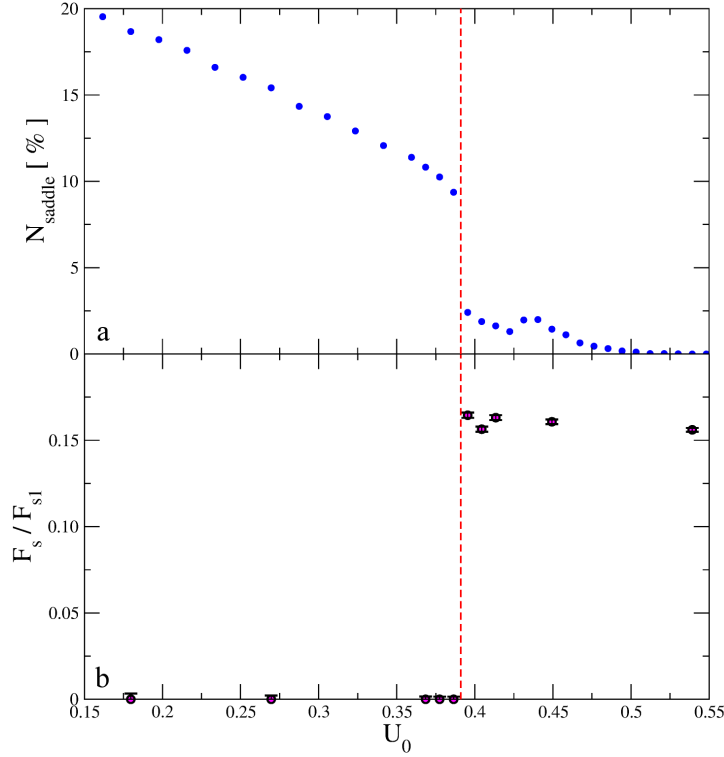
Figure 3.17: Unrotated $\theta = 0$ mismatched colloid monolayer, $\rho \approx 0.927$. (a) Fraction of colloidal particles which populate repulsive regions of the corrugation potential (where $W(x, y)$ exceeds the saddle-point energy) plotted as a function of the corrugation strength U_0 across the superlubric-pinned transition. The dashed line marks the transition point $\tilde{U}_c = 0.391$. (b) Static friction force F_s, normalized to the depinning force F_{s1} of a single particle in the same periodic potential. Above the transition the monolayer locks onto the corrugation. The error bar is defined by the force increment $\Delta F = 0.001$ used in the simulation protocol.

the static friction F_s. Actually in this metastable aligned case the subsequent evolution of static friction becomes somewhat erratic. This behaviour can be explained as follows. A proliferation of energetically close metastable configurations – each characterized by its own static friction – is expected [101] above the transition point. While at θ_{opt} all protocols produced configurations with regularly-spaced hexagonal domains, at $\theta = 0$ we observe several both irregular and regular arrangements of registered domains, which then happen to be energetically favored at different corrugation values U_0 (see Fig. 3.18c,d). Some fluctuations in F_s are therefore expected when one also considers that in incommensurate systems with many degrees of freedom, states with lower energy do not necessarily display a higher static friction force [168]. This complexity disappears below U_c where there always is a unique structure, shown in Fig. 3.18a,b, respectively away and close to the transition. Summing up this part, the evolution of the monolayer structure as a function of U_0 is highly sensitive to the misalignment angle.
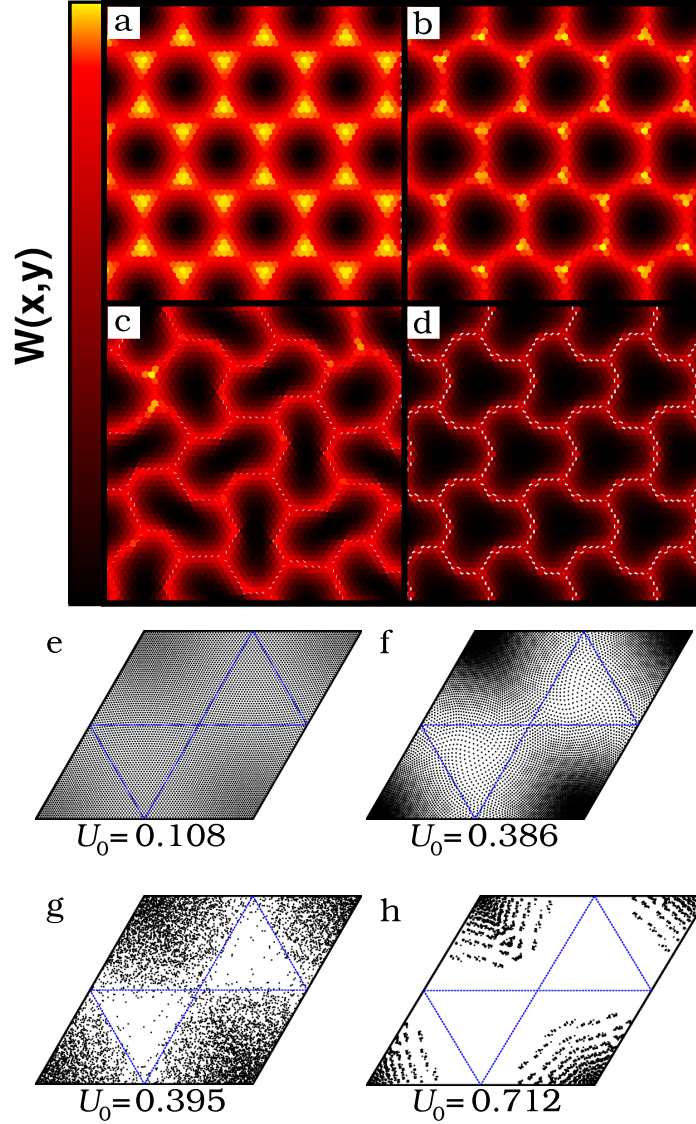
Figure 3.18: Panels (a-d): the moiré patterns of the fully relaxed monolayer at $\theta = 0$. A small portion of the simulation supercell is shown. Each dot represents a particle, colored according to the local corrugation potential $W(x, y)$: dark for potential minima, bright for maxima. Panels (e-h): the particles' positions are reported into one primitive cell of the substrate triangular potential. Configurations are shown for the following values of the corrugation:(a,e) $U_0 = 0.108$ – superlubric phase. (b,f) $U_0 = 0.386$ – just below the transition. (c,g) $U_0 = 0.395$ – just above the transition, where the energetically favored configuration consists of an arrangement of irregular domains. (d-h) $U_0 = 0.712$ – a strong-corrugation phase corresponding to an arrangement of regularly-shaped registered domains.

3.5   Final remarks

Colloids in optical lattices are systems recently introduced, potentially representing powerful tools which may contribute to our understanding of friction between crystalline surfaces [120, 131, 147, 149]. We showed that monolayers in an incommensurate optical lattice develop, in full

equilibrium and with realistic parameters, a small-angle structural misalignment, quite evident in moiré patterns such as those of Fig. 3.7. Upon forced sliding, this misalignment can considerably increase the sliding friction, directly extractable from the colloid drift velocity in experiment, using Eq. (3.8), over the hypothetical aligned geometry. The present results and understanding naturally extrapolate to the sliding of misaligned incommensurate lattices in contact such as, for example, physisorbed rare-gas or molecular submonolayer islands [163–165]. An interesting side aspect is in this case that misalignment transforms the orientation angle of a physisorbed island, generally assumed to be fixed, into a continuous and possibly dynamical variable. The inertial sliding friction of such islands determines the inverse slip time in quartz crystal microbalance experiments [169], whose data must, at least in some cases, embed the frictional enhancement caused by misalignment when present. Even though the time needed to diffuse-rotate a ~ 100 nm-size island may be exceedingly large, the orientation angle distribution of islands will usually, under either stationary or sliding conditions, be continuous rather than delta-function like. The general unavailability of 2D lattice orientation of incommensurate rare gas islands (as opposed to full monolayers, whose epitaxy generally differs) poses at present an obstacle to the investigation of these effects, which must nonetheless be considered as generically present an effective. The possible local misalignment of incommensurate 3D crystals in contact and its potential role in sliding friction is an even less explored, but interesting issue which remains open for future consideration.

Colloidal monolayers in an incommensurate lattice corrugation potential, we propose, also represent ideal systems for the study of the superlubric-pinned transition, expected as a function of increasing corrugation strength. In 1D it is well known that the onset of a disorder parameter – measuring a region of phase space inaccessible to particle positions – impedes the dynamics of free-sliding motion, giving rise to static friction through a continuous phase transition [99, 101]. In the 2D case of colloids we predict a transition of similar character, the main difference being now its first-order character. Moreover, the relative alignment and misalignment of the two lattices plays an additional role. We found vanishingly small static friction up to a critical value U_c corresponding to a joint structural and dynamical transition of the monolayer. At the transition the colloidal crystal adapts to the periodic potential by a local rotation (back to registry) of the nearly commensurate domains forming the moiré of the incommensurate phase. Similarly to the 1D case, pinning of the monolayer is due to a collapse to zero of the number of particles sampling the most repulsive regions of the periodic potential. These poorly placed particles are those which are easily set into motion in the superlubric phase. Their disappearance is therefore responsible for the arising of static friction in the pinned state. Experimentally, vanishingly small values of F_s have been observed in 2D incommensurate structures [111, 131], but the realization and the analysis of the transition between superlubric and pinned states is missing to our knowledge. The present work suggests the possibility to pursue and investigate in detail the superlubric-pinned transition by gradually increasing the optical-lattice strength. Additional phenomena may be accessed by forcing rotations and modifying the natural misalignment of the colloidal crystal with respect to the optical lattice. Since the superlubric phase at $\theta \neq \theta_{\mathrm{opt}}$ survives up to larger corrugation values, rotations of mismatched sliders initially away from the optimal orientation might in fact end up in reentrant pinning as soon as θ_{opt} is hit, in a way similar to the matched case ($\rho = 1$, $\theta_{\mathrm{opt}} = 0$) of a rotated graphene flake sliding over graphite [116].

CHAPTER 4

Static Friction Scaling of Physisorbed Islands

A long-standing puzzle in nanotribology is the persistence of static friction even for ideal mesoscale sized sliders such as incommensurate physisorbed islands on atomically perfect crystal surfaces, where one could expect it to asymptotically vanish. Here we show, based on prototype atomistic simulations of rare gas islands sliding on a crystal surface, that the slider's edges represent the ultimate actors. When the island body is ready to slide "superlubrically", the sliding is impeded by an edge-originated barrier that prevents the misfit dislocations or solitons from moving. Only when the static friction force is reached, the barrier vanishes locally at one point on the edge, solitons enter through this point to sweep the island, which only then becomes depinned and free-sliding. We show that finite size scaling of static friction of a superlubric rare gas island with area A has the same form A^{γ_s} as discussed in literature for dynamic friction, but with specific, generally distinct static scaling exponents γ_s that are edge-controlled and smaller than $1/2$, as opposed to $\gamma_s = 1$ for pinned, commensurate islands. The island static friction connection with edges, here addressed realistically in rare gas islands for the first time, constitutes the controlling factor for inertial depinning in quartz crystal microbalance experiments, and is expected to be a factor of importance for nanotribological applications involving weak contacts.

In Section 4.1 we introduce the problem and we discuss the questions addressed in this Chapter. Section 4.2 is devoted to the definitions of the rare-gas-island/metal model interface potential and to the simulation protocols. In Section 4.3 we present results on the island depinning and the static friction scaling law with island size. Section 4.4 discusses the solitons dynamics at the depinning transition, while in Section 4.5 we describe the effects of temperature. Section 4.6 contains our final remarks.

4.1 Introduction

Understanding the atomic-scale mechanisms which control friction is probably one of the most important challenges in nanotechnology [11, 97, 170, 171]. Static friction is basic not just to our everyday experience, including standing and walking, but is crucial, and often fatal, to the working of nanosystems [172]. In nanomotive devices, as well as in elementary processes such as the pulling or pushing of nano-objects on a surface by a tip [154, 155, 173], or by a colliding molecule [174], or by simple inertia [137, 169], static friction constitutes the ultimate obstacle that affects the onset of sliding. Often undesired, static friction of nano-sliders can also be of help, e.g., to prevent the diffusive sliding away of adsorbed molecules, small proteins clusters and

of islands, favoring so-called nano-positioning when deposited on surfaces [175, 176]. Despite its importance, and several notable exceptions [118, 177–181], static friction is not as much discussed and qualified as dynamic friction. Differently from macroscopic sliding where relatively complex processes due to asperities and multiple contacts [96], or to load inhomogeneity [177, 178, 181] are at play, homogeneous crystalline nano-sliders offer a unique opportunity to address static friction in its simplest form – that between perfectly regular, periodic faces.

Given two crystals in contact, e.g., a two-dimensional (2D) adsorbate monolayer island (the slider) and a perfect crystal surface (the substrate), different possibilities may occur. The island lattice may be commensurate (C) with the surface lattice, or it may be incommensurate (IC), meaning that the two lattice 2D cells cannot be made to coincide by any rational scale change p/q, where p and q are two integers. In the general C case, and also in the IC case if the slider is "soft" (inter-atomic forces weaker than or similar to the typical substrate corrugation forces, causing effective commensurability to prevail), the island will exhibit static friction, due to pinning of the two lattices. The latter situation of strong contact has been theoretically addressed by a number of workers [118, 148, 149, 177–181]. Conversely, static friction should ideally vanish, foreshadowing free sliding, also called "superlubricity", for a prototype weak contact, such as an infinite, hard IC crystalline slider, weakly interacting with a perfectly periodic substrate [1] [75, 95, 99, 102, 183].

Evidence of low dynamic friction in noncrystalline sliding has been collected by AFM manipulation of amorphous and crystalline antimony nanoparticles deposited on a graphite substrate [154, 155, 184]. At the same time however the corresponding static friction, even if conceptually and practically different, and no less important, was generally skirted in these low-friction contacts. In recent studies of 2D incommensurate colloidal crystals sliding over optical lattices, static friction emerged clearly, along with a pinned-to-superlubric transition for decreasing periodic potential magnitudes [120, 131, 185], as discussed in the previous Chapter. Static friction controls directly the quartz crystal microbalance (QCM) sliding experiments [137, 169, 186] which we consider as our reference system. In QCM a crystal surface with a layer, but particularly a submonolayer coverage of physisorbed inert gas is periodically shaken to dislodge the 2D crystalline islands formed by coalescence of the adsorbed gas molecules, giving rise to inertial sliding friction. These submonolayer islands generally constitute incommensurate sliders [187], which as a rule should behave as hard (even if not at all rigid) since the gas interatomic energy, of order 15 meV, although much weaker than the atom-surface adhesive energy of order 150 meV, is usually much stronger than the substrate corrugation, typically only a few meV [188]. QCM data in UHV generally show that for low rare gas coverage, low temperature, and moderate oscillatory force magnitude, adsorbed islands remain stuck to the surface and do not slide, despite cleanliness, hardness and incommensurability [52, 136, 186, 189]. The islands remain pinned by static friction until either the growing inertial force, or the increasing coverage – which implies a larger average island size [190] and thus a larger inertial force – or temperature, reach a threshold value. Only beyond that point, the static friction is overcome, the islands depin, and inertial sliding takes place with a nonzero slip time [2] whose inverse measures dynamic friction [137, 169, 186].

Our main goal is to understand the ultimate reason why static friction should persist even for ideally perfect rare gas islands adsorbed on crystalline surfaces, which constitute weak contacts where owing to incommensurability free superlubric sliding could be expected. Real-life surfaces are of course far from perfect, so that an adsorbed island will generally attach to surface steps,

---

[1]The small static friction at the sliding interface between two ideally hard disordered surfaces, e.g., metal on glass has also been discussed [179, 182].

[2]The definition of slip time and its relation to dynamic friction is discussed in Section 1.1, see Eq. (1.1).

defects, impurities, etc., which can provide extrinsic pinning [118]. Nevertheless, static friction of cold adsorbed islands generally survives the progressive elimination of defects, and their pinning effect by reducing the oscillation amplitude [189, 191, 192]. For a defect free, genuinely incommensurate hard island, such as is realized for example by Kr/Pt(111) [193], and most other cases where the island-surface commensurability ratio is known to drift continuously with temperature, there should be no barrier and no pinning. Here an intrinsic source of static friction must be at work.

The edge is an intrinsic "defect" that every island, cluster, or deposited nanosystem, must have. We conducted simulations mimicking realistic 2D incommensurate rare gas islands up to very large size, adsorbed on defect free metal surfaces. These simulations clearly show that even without defects, these weak contacts exhibit a basic static friction threshold dictated by the island edges. Specifically, for an adsorbed island, where the misfit lattice-mismatched dislocations (i.e. solitons) pre-exist, we find that the entry through the island edge of a new soliton is the event that initiates the depinning and the subsequent superlubric sliding. Soliton entry however is not cost free; the pushing force must overcome an edge-related energy barrier, which is thus the controlling element of the island's static friction. The barrier's relative role and importance, and the ensuing static friction are found to decrease with increasing island size and temperature, precisely as seen in experiments. Since the static friction is edge-originated, its scaling $F_s \sim A^{\gamma_s}$ with the island's area A is not only sub-linear, $\gamma_s < 1$, but sub-linear even with respect to the coarse-grained island perimeter $2(A\pi)^{1/2}$, that is $\gamma_s < 1/2$, indicating that only a zero-measure subset of edge points is responsible for the pinning barrier. By contrast with this result for incommensurate islands we examine in parallel that of commensurate islands, strong contacts which have a "bulk" pinning, with a trivial area scaling exponent $\gamma_s = 1$. Even there nonetheless the edge plays a role. We find that the lattice dislocation triggering the sliding of a commensurate island nucleates, as also discussed by previous workers in different situations [177, 178, 181], preferentially at the island edge, here acting therefore as a facilitating element which quantitatively reduces the static friction.

In the far more common case (for physisorption) of incommensurate islands, we will identify, at the general level, the emerging key parameters which control edge-induced static friction. They are: a) the shape, rugosity, and elasticity of the island edge, which influence γ_s, a sublinear size scaling exponent that does not appear to exhibit universality; b) the amplitude of the substrate corrugation potential, which controls the static friction magnitude; c) the temperature, influencing static friction both directly, and indirectly through the island's changing incommensurability.

The role of edge-induced static friction is, we propose, especially important for QCM experiments, a context in which it has apparently not been previously discussed. As was said above, it is a general observation in QCM that lack of inertial sliding, and a consequent zero slip time, occurs in all cases for a sufficiently low coverage and low temperature, a regime where the adsorbate forms crystalline islands that are generally incommensurate with a crystalline substrate [137, 169, 186, 187, 189, 191, 192]. We will show that realistic parameters for the adsorbed rare gas on a metal surface predict that the QCM inertial force cannot reach, as coverage increases, the low temperature static friction threshold for depinning until the island diameters grow as large as many tens when not a hundred of nanometers. That is a remarkably large size, comparable to that of terraces or facets of even a good quality metal surface. The conclusion is thus that intrinsic edge pinning is not just qualitatively, but quantitatively important in QCM and other incommensurate nano-sliding experiments. We also find that the effects of temperature are diverse and intriguing. Besides increasing the edge rugosity, temperature does reduce the effec-

tive substrate corrugation, which in turn lowers the static friction threshold. At the same time, the commensurability ratio of the two lattices may drift with temperature because the island's thermal expansion is generally unmatched by that of a metal substrate. As temperature grows, one or more low order commensurabilities may accidentally be hit, at which point a geometrical interlocking barrier against sliding arises, leading in principle to the novel possibility of reentrant static friction.

4.2 Computational details

4.2.1 Model interaction

To substantiate our discussion with a specific case study, we model an incommensurate rare gas island on a metal surface with parameters appropriate to Kr/Pb(111), a prototype system of current interest [192] which we adopt here as a generic model hard slider. In our model the Pb(111) hard substrate is treated as a fixed and rigid triangular lattice frame, exerting on the mobile Kr adatoms an average attractive potential $V \sim -150$ meV, and a weak corrugation $\Delta V / V$ roughly in the range 2-5% between the on-top Pb site (the energy is minimum for a Kr adatom), and the hollow Pb site (energy maximum). Each Kr adatom is thus submitted to the overall potential $V = V_{\mathrm{Kr-Kr}} + V_{\mathrm{Kr-Pb}}$. The Kr-Kr interaction is modeled as regular Lennard-Jones (LJ) potential, with $\epsilon = 0.014$ eV and $\sigma = 3.65$ Å. Tiny corrections due to three-body forces as well as substrate-induced modifications of this two-body force are ignored. The Kr-Pb interaction is modeled by the following Morse-modified potential:

$$V_{\mathrm{Kr-Pb}} = \alpha(x, y) \left(\mathrm{e}^{-2\beta(z-z_0)} - 2\mathrm{e}^{\beta(z-z_0)} \right). \tag{4.1}$$

The (111) structure of the substrate is accounted for by replacing the function $\alpha(x, y)$, that must exhibit the same periodicity of the underlying triangular lattice (we neglect here the small differences between fcc and hcp stacking sites). To represent the substrate modulation, we make use of the function

$$M(x, y) = \frac{2}{3} - \frac{4}{9} \cos\left(\frac{2\pi x}{b}\right) \cos\left(\frac{2\pi y}{\sqrt{3}b}\right) - \frac{2}{9} \cos\left(\frac{4\pi y}{\sqrt{3}b}\right). \tag{4.2}$$

The constant b is the nearest neighbor distance of surface atoms. The modulating function $M(x, y)$ has been normalized to span the interval from 0 (top sites) to 1 (hollow sites). Back now to the Morse potential, the energy parameter is given by

$$\alpha(x, y) = \alpha^{top} + M(x, y)(\alpha^{hollow} - \alpha^{top}), \tag{4.3}$$

with the on-top adhesion energy $\alpha^{top} = 150$ meV and on-top equilibrium distance $z_0 = 3.75$ Å [194, 195], while β is obtained by equating the second derivative of the potential to the experimental spring-constant,

$$V''(z_0) = 2\alpha^{top}\beta^2 = \omega^2 m_{Kr} , \tag{4.4}$$

m_{Kr} is the atomic mass of Krypton. With a perpendicular vibration energy of $\hbar\omega \simeq 3$ meV [194, 195], we obtain $\beta = 0.775$ Å^{-1}. The α^{hollow} parameter is varied accordingly to the desired corrugation, and takes the value of 142.5 meV and 147 meV for the simulated corrugations of 5% and 2% of the on-top adhesion energy, respectively.

The LJ parameters leads to a nearest neighbor Kr-Kr distance which at 10 K (the lowest

temperature of validity of our classical simulations, roughly equal to the temperature of quantum freezing in Kr) is close to the 3D experimental value of 4.01 Å, in turn 13% higher than the Pb-Pb triangular substrate nearest neighbor distance of 3.50 Å. Thus, the island and substrate 2D lattices are incommensurate with a ratio of 0.8728 at $T = 10$ K. Upon moderate heating, the island readily expands but the substrate does not. The closest strong commensuration of $6/7 = 0.8571$ of Kr/Pb(111) is reached and surpassed near $T \approx 20 - 22$ K.

To model the commensurate islands we reparametrized the substrate potential in order to match adhesion and corrugation energies of 190 meV and 1.9 meV, respectively, and a lattice constant of $3.61\sqrt{2}$ Å, borrowing them from the Xe/Cu(111) case [148]. Starting from a Xe-Xe Lennard-Jones energy $\epsilon = 20$ meV, we used an ad-hoc $\sigma = 3.90$ Å in order to fictitiously match, at $T = 50$ K, the $\sqrt{3} \times \sqrt{3}$ Cu(111) spacing.

4.2.2 Simulation protocols

We restrict to temperatures well below half the adsorbate bulk melting temperature, $T \ll T_m/2$ (for $T_m = 115$ K, we employ $T \ll 60$ K), where the adsorbate island does not yet melt, remaining crystalline with a 2D triangular lattice only weakly modulated by the incommensurate and essentially rigid underlying (111) metal substrate. For different assumed shapes we simulate a sequence of islands consisting of N adsorbate atoms, with N increasing up to a maximum size of about 300000. Using molecular dynamics we first relax and anneal the islands – initially cut out of a perfect triangular lattice – in the (111) periodic potential mimicking the perfect crystal substrate, and optimize the overall island adsorption geometry so as to minimize energy. In the resulting zero temperature state, the main interior part of the island and the substrate are incommensurate, with the model Kr atom-atom spacing $a = 4.057$ Å only slightly smaller than $(7/6)a_s = 4.084$ Å, where $a_s = 3.50$ Å is the nearest neighbor distance in Pb(111). Exact 7/6 commensurability would require the slightly larger value $a = 4.0842$ Å. Due to this mismatch, the adsorbate island shows commensurate domains joined by bands of higher atomic density: the solitons, whose exact pattern depends on parameters, such as the temperature and the island size. To visualize the soliton superstructures, we developed a method exploiting information from all the adsorbed atoms. If the krypton atoms would occupy the position of a perfect triangular lattice with commensurability ratio 7/6, a uniform dilation by a factor 6 would map each adatom onto a position on top of a substrate atom. Thus, given an atom with coordinates (x, y, z), its dilated in-plane position $(X, Y) = (6x, 6y)$ must render the modulating function M (Eq. 4.2) equal to zero, in the commensurate domains. The solitons, characterized by an enhanced mobility due to the mismatch with the substrate, are instead regions with $M(6x, 6y) \gtrsim 0$. Plotting each atom in blue scale, ranging from blue to white according to increasing values of $M(6x, 6y)$, the commensurate domains appear dark blue and the solitons as white bands (see Fig. 4.1). These pictures highlight the great deformability of this gossamer superstructure, well beyond any rigid or nearly rigid approximation. Compression/dilation strains in the 2D lattice are directly reflected by increased/decreased density of superstructures.

To simulate QCM depinning, we apply to all atoms of the annealed adsorbate island a constant lateral force. This is adequate because the QCM oscillation period of $\sim 10^{-7}$ s is much longer than our simulation times. Static friction is measured in incommensurate systems using the following protocol: (i) an initial 1.2 ns annealing run at $T = 25$ K, with no force applied ($F_{ext} = 0$); (ii) a 1.2 ns run at $T = 0$ K, with typical Berendsen thermostat constant $\tau = 100$ ps and still $F = 0$; (iii) the thermostat is removed, and a series of 1.2 ns runs at 0 K, with F applied instantaneously after the annealing procedure.
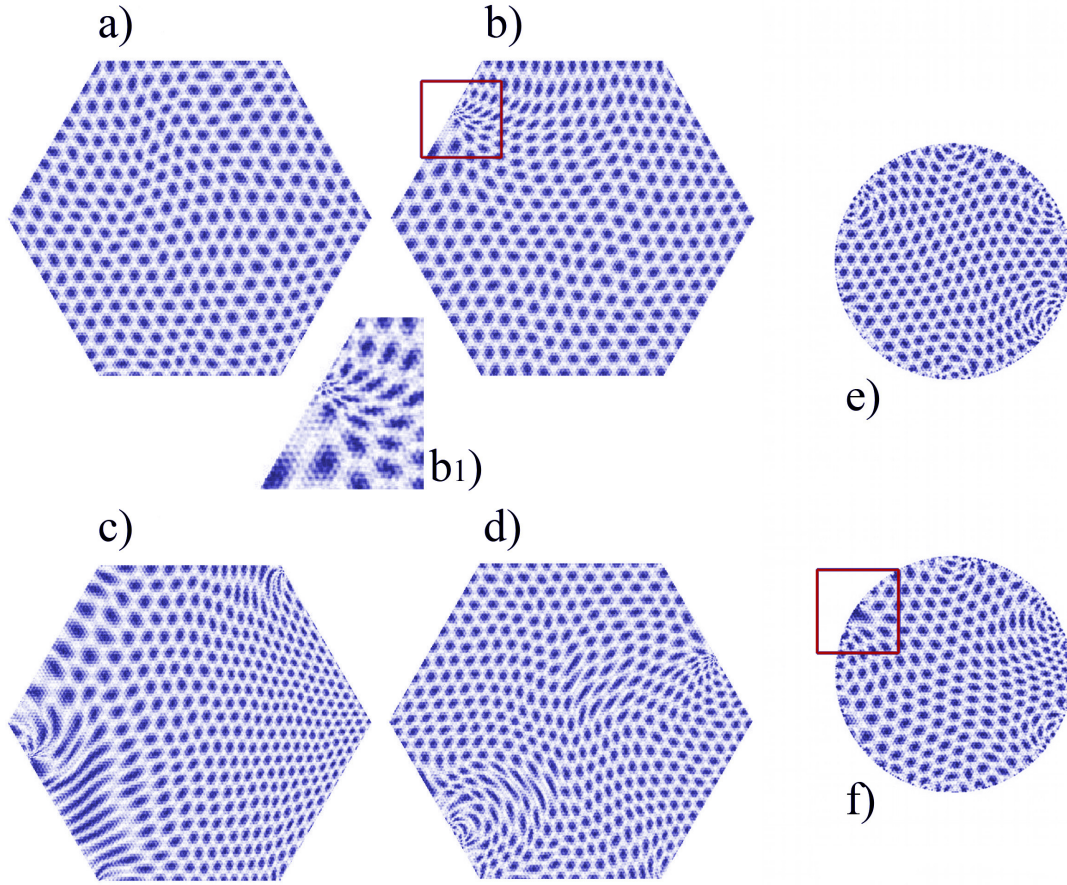
Figure 4.1: Model ideal hexagonal ($N = 269101$) and circular ($N = 177507$) Kr islands adsorbed on Pb(111). Pictures show maps of the island, with colors ranging from dark blue when Kr atoms are maximally coincident with a (6/7) rescaling of the underlying Pb atom positions, to clear when they are minimally coincident. The resulting moiré patterns, enhanced in this manner for visibility, highlight the soliton network between the island and surface lattices and their evolution at the static friction threshold. (a) After annealing, at zero temperature and zero applied force ($T = 0$, $F_{ext} = 0$); (b) with applied force $F_{ext} = 1.4$ eV/Å, just above the static friction value, and right after the soliton entry at a left edge corner – highlighted by the red square and magnified by the zoomed in region (b1); (c) same system after sliding of the island center by one surface lattice spacing. Note the density accumulation at the front edge and rarefaction at the trailing edge, showing the frictional role of the edges; (d) same system at later time when the sliding is 1.5 lattice spacings, and a soliton exits the island on the right hand side. (e) Circular island, just after annealing ($T = 0$, $F_{ext} = 0$); (f) with applied F_{ext} slightly above the static friction threshold. Here again the static friction is determined by the entry of a soliton at the left edge, highlighted by the red square.

Simulations of commensurate systems are performed at $T = 50$ K. Similarly to above, we increase the external force from zero to F_s, at increments of 0.01 eV/Å, letting the simulation evolve for 100 ps after each force step. In all cases, a displacement of the island center-of-mass by 2 lattice spacing within the same force step is taken as the signal of depinning. The static friction so obtained should depend slightly on the waiting time, but we verified that the decrease due to thermal barrier hopping was negligible with a waiting time longer than 1.2 ns.
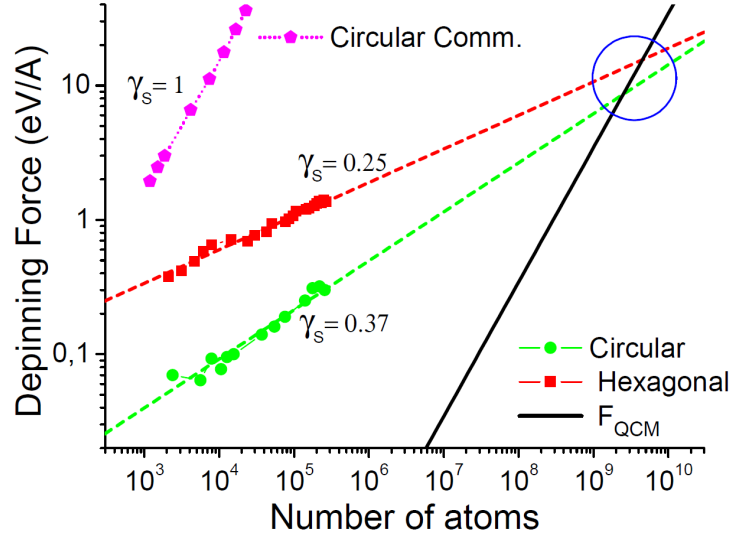
Figure 4.2: Size scaling of total static friction force F_s of simulated incommensurate adsorbed islands (modeled on Kr/Pb(111)) at $T = 0\,\text{K}$ as a function of the atom number N (log-log scale) for (*i*) hexagonal islands (squares); (*ii*) circular islands (circles). Assumed surface corrugation: 5% of the atom adsorption energy; note the strongly sublinear scaling for both shapes. The intersection with the estimated QCM inertial force (black solid line) is emphasized (blue circle), showing how the edge-originated static friction alone can prevent island sliding up to large island sizes, which qualitatively corresponds to large sub-monolayer adsorbate coverages. By comparison we also show the size scaling of static friction ($\gamma_s = 1$) for a *commensurate* adsorbate at $T = 50\,\text{K}$. The commensurate frictional stress F_s/A is about $10^7 N/m^2$ compared with a much smaller 40 N/m^2 of incommensurate islands at inertial depinning.

4.3 Island depinning and size scaling of static friction

We simulate the forced depinning of the island by applying to the island center of mass a constant planar total force F_{ext}, that is by applying to each Kr atom a force F_{ext}/N. In our protocol the static friction is the lowest value of F_{ext} sufficient to cause, within 1.2 ns simulation time, a center-of-mass drift of two substrate interatomic spacings, or 0.7 nm, signaling the depinning of the island [3]. The shapes of the island edge, in principle quite important for static friction, are not easily equilibrated in MD simulations at the low temperatures considered. We therefore examine two ideally opposite test shapes, perfect hexagonal and circular – neither of them realistic but providing together a fair idea of the generic behaviour to be expected. Torques and sliding-induced overall rotations arising from possible non-centered island shapes are also neglected. Despite the natural random asymmetry expected of realistic islands, their large size prevents the brownian motion of their orientations (as well as of their centers of mass) making the torque needed to cause their overall rotation generally very large for QCM.

Fig. 4.2 shows, in log-log scale, the overall static friction force $F_0(N)$ necessary to depin commensurate and incommensurate islands made up of N atoms. Our main result is that the static friction of incommensurate islands is very small but nonzero, and interestingly area-dependent. For each given shape the static friction obeys with striking precision a power law scaling $F_s \sim F_0(A/\Sigma)^{\gamma_s}$ where $\Sigma = a^2\sqrt{3}/2$ is the area per adsorbed atom. The incommensurate

---

[3]Note that QCM oscillations, of typical frequency $f_0 \sim 10\,\text{MHz}$, are essentially static on the simulation timescales.

exponent γ_s varies between 0.25 and 0.37 depending on the choice of edge morphology, here polygonal or circular, respectively. While of course real islands will generally look like neither, the two cases provide reasonably extreme instances, the circular probably more realistic than the polygonal, in virtue of its greater variety of edge atom configurations. We further show that in both shapes the island static friction barrier resides in a small set of points on the edge, as a consequence of which the static friction exponent γ_s is definitely less than $1/2$, the value expected if the density of the pinning points on the edge was uniform.

The commensurate island static friction obtained in simulation is by comparison five to six orders of magnitude larger than the incommensurate static friction, which demonstrates and emphasizes the huge gap between a strong and a weak contact. With increasing island size, we find that the commensurate friction force F_s grows proportionally to the area, $\gamma_s = 1$, as expected when the bulk of the island participates in the static friction barrier, resulting in a static friction stress F_s/A independent of area.

The size-independent static friction shear stress F_s/A for our model commensurate islands of small size is about $10^7 N/m^2$. We can compare that with the nominal theoretical interface stress of a rare gas on metal (G/M) interface $\mu_{G/M} = \frac{2\mu_G\mu_M}{\mu_G+\mu_M} \simeq 1.16*10^9 N/m^2$ (where $\mu \equiv C_{44}$ are the respective bulk shear elastic constants, here of Kr and Pb), to conclude that the commensurate island static friction stress obtained is about $10^{-2}\mu_{G/M}$. Interestingly, that falls inside the range $\mu_{G/M}/30 \div \mu_{G/M}/1300$ expected from dislocation theory of macroscopic, commensurate and inhomogeneous strong contacts [177, 178, 181].

Returning to our main system of interest, the simulated incommensurate Kr/Pb islands, the shear stress F_s/A is many orders of magnitude smaller than the commensurate, and unlike that case is clearly size-dependent. A physically relevant island area where we wish to evaluate the static friction force $F_s(A)$ is the critical area at which it equals the peak inertial force in a QCM experiment, $F_{QCM}(A_{crit}) = \rho A_{crit}\Delta(2\pi f)^2$, where ρ is the adsorbate 2D mass density, Δ the QCM oscillation amplitude, f the frequency. Only in islands whose area exceeds A_{crit} the inertial force exceeds static friction, and inertial depinning followed by dynamic frictional sliding can take place. Experimental QCM orders of magnitude being $\Delta \sim 100 \text{\AA}$, $f \sim 10$ MHz yield an inertial force which grows linearly with A and crosses, as shown in Fig. 4.2, the static friction lines $F_s/A_{crit} = F_{QCM}/A_{crit}$, signaling depinning above a critical area

$$A_{crit}/\Sigma \sim \left(\frac{F_0}{\Sigma\rho\Delta(2\pi f)^2}\right)^{\frac{1}{1-\gamma}}. \tag{4.5}$$

The incommensurate island data of Fig. 4.2, obtained for an assumed 5% Pb(111) substrate corrugation, yields $N_{crit} = A_{crit}/\Sigma \simeq 3 \cdot 10^9$, or $A_{crit} \simeq 4.3 \cdot 10^{10} \text{\AA}^2$.

That amounts to island diameters of the order of several microns, corresponding to an inertial static friction force of order 16 nN, equivalent to a QCM depinning stress $\simeq 40 N/m^2$, more than seven orders of magnitude smaller than $\mu_{Kr/Pb}$, and more than five orders of magnitude smaller than the commensurate island static friction stress $\simeq 10^7 N/m^2$. Qualitatively similar data are found for lower corrugations, where the static friction force and thus the critical depinning area A_{crit} drops by a factor $\sim 5 \div 15$ when the corrugation is decreased from a large 5% (where phenomena are easier to study) to $2 \div 1\%$.

At larger incommensurate lattice mismatch, and under the effect of temperature the critical island size for depinning and the static friction shear stress will be correspondingly smaller, but we still expect large critical island diameters ranging from many tens to hundreds of nanometers.

Incommensurate islands smaller than this size will remain pinned by their own edge, and

only larger ones will overcome the edge-originated static friction and slide inertially in QCM. These large estimated critical radii constitute a strong result of this work: the intrinsic edge-related static friction is by no means a small or academic effect, as one might initially have expected. Strong as it is, the edge contribution can in fact add significantly to impurity and defect pinning [179], even after renormalization of F_s caused by edge roughness and temperature. The order of magnitude obtained for the critical depinning island size must be compared with the general experimental observation of a critical adsorbate coverage of 5-30% below which static friction wins, there is no low temperature inertial depinning, and the slip time remains zero even on the cleanest surface, and even for small oscillation amplitudes, a regime where dilute defects play a smaller role. If a real surface is crudely assumed to consist of terraces of hundreds nanometers in size, the A_{crit} corresponds to a non negligible submonolayer coverage, in agreement with experimental observations, such as e.g., in Ne on Pb(111) [189, 192]. For a strongly commensurate island conversely the inertial force $F_{QCM}(A)$ and the static friction force F_s are both proportional to A and do not cross as A grows, indicating that the island will not inertially depin and remain stuck by its own bulk static friction, at least until larger island sizes and temperatures outside of this study.

4.4   Edge pinning and soliton flow

We can now address the question, what is the physics of edge-induced pinning? One key observation is that in order for an island with lattice parameter a to slide over a surface with lattice spacing b, the misfit soliton lattice, of spacing $L = a/(\frac{a}{b}-1)$ (see Section 3.2.3), must *flow* across the island in the sliding direction with a much larger speed $v/(\frac{a}{b}-1)$ than the overall island speed v [4] – solitons must move very fast in order for the island to move even slowly. The sublinear size scaling of F_s with $\gamma_s < 1/2$ in Fig. 4.2 occurs because solitons enter the island through specific points and not everywhere along the edge – a corner in the perfect hexagonal shape for example – and then sweep past, setting the island's soliton pattern in a state of flow. The motion of solitons is necessary for the island to slide. By preventing the free motion of solitons, which implies their free entry and exit, the island edges cause static friction. The local planar density of atoms for an edge-pinned island at pulling force just below the static friction threshold shows an accumulation on the island front and a rarefaction on the back side, also demonstrating the importance of non-rigid effects in larger regions surrounding the edge – the pinning agent. The edge adatoms lower their potential energy by settling in local minima, thus breaking the ideal island-surface translational invariance. We note incidentally that the settling of edge atoms also implies a local vertical deformation, besides a horizontal one, of the island boundary [196]. The overall relaxation gives rise to an edge related ("Peierls-Nabarro") energy barrier for the motion of solitons into and out of the island: the 2D edges cause the nominally incommensurate island to become stuck and pinned against sliding.

The observed depinning phenomenology with solitons getting in and out of the island edge resembles that of the caterpillar-like motion of the finite one-dimensional Frenkel-Kontorova model, where an edge barrier opposing kink motion gives rise to static friction [99]. Many additional 2D factors, such as sliding-induced relative lattice orientation, island shape, vertical relaxations, edge rugosity, adsorbate elasticity, etc., will enter in determining the exact value of the sublinear γ_s exponent, whose nontrivial theoretical description we do not attempt here.

---

[4]Because of periodicity, a monolayer displacement of one lattice spacing a, occurring in a time interval Δt, brings the moiré superstructure in itself, this means that in the same time interval the moiré has to move a distance L.
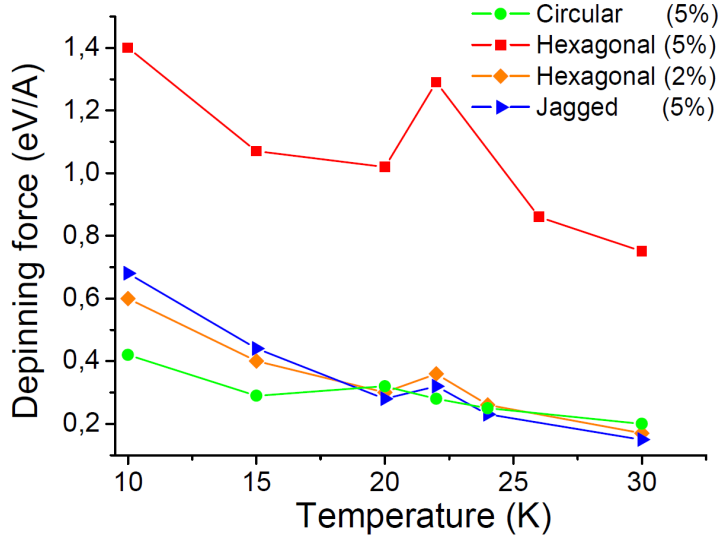
Figure 4.3: Static friction force F_s as a function of temperature, for differently shaped islands (hexagonal, circular, and jagged, of about $3 \cdot 10^5$ atoms) and substrate energy corrugations (between 2 and 5 % of the atom adsorption energy). Superposed to the general decrease, the visible peak at 22 K reflects the low order adsorbate-surface 6/7 commensurability accidentally hit due to the island thermal expansion. This kind of accident, here portrayed for our model of Kr/Pb(111), might more generally lead to re-entrant pinning in QCM.

4.5 Temperature effects

We come finally to discuss the effects of temperature on the edge-dependent static friction of incommensurate islands. The thermal evolution of static friction provided by simulations is shown in Fig. 4.3 for the hexagonal, circular, and jagged islands, and for different substrate energy corrugations. Not surprisingly, thermal fluctuations facilitate the reduction of edge energy barriers, lowering static friction and favoring island depinning under the action of F_{ext}.

A second temperature effect will be to enhance thermal roughening of the island's edge, via adatom migration and 2D evaporation-condensation processes. The edge irregularity slightly modifies the overall soliton map in the island, especially close to the edge atoms that are stuck, a factor probably impacting the tribological response of the system, although most likely not more than shown by the difference between hexagonal and circular islands.

A third temperature effect is the anharmonic thermal expansion of the island's 2D lattice against the metal substrate, not yet expanding at these low temperatures. This thermal drift of lattice parameter ratio between the two crystalline surfaces in contact results in an alteration of the interface commensurability with consequences on static friction. In the chosen example of Kr/Pb(111), the relative registry is expected to drift from frank incommensurability at 10 K to a "6/7" higher order commensurability near 20-25 K and then again to incommensurability above that temperature. In our simulations this accidental, weak high-order commensurability gives rise to a temporary rise of static friction (Fig. 4.3). Even if the effect is not strong, and is sensitively dependent upon unknowns such as the edge rugosity and the substrate crystalline corrugation magnitude, in our realization we observe a small but visible peak of the temperature-dependent static friction for all the simulated island shapes. As highlighted in Fig. 4.4, the corresponding smearing in the pattern of the soliton network, the hallmark of an enhanced
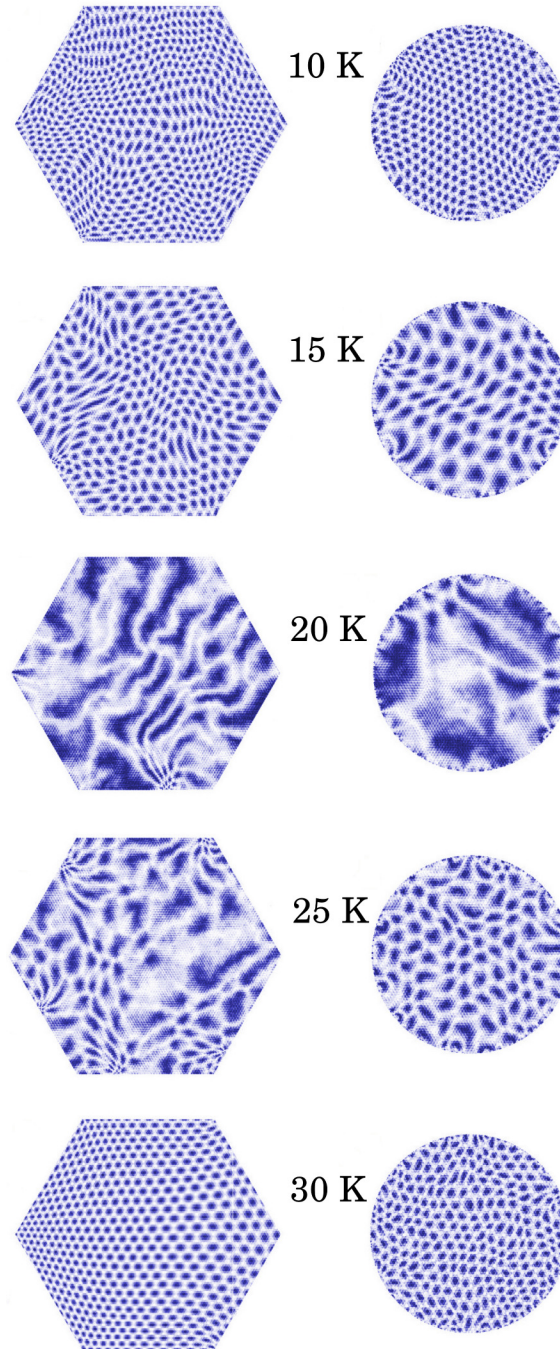
Figure 4.4: Thermal evolution of the soliton network portrayed for hexagonal and circular shaped islands using the contrast enhancement technique for the lateral density variations relative to a 6/7 commensurability. The island thermally expands, going from relatively overdense at low temperatures to underdense at high temperatures, thus exhibiting accidental near commensurability around 20-22 K.

interface commensurability, for $T = 22\,\mathrm{K}$ (hexagonal island) and $T = 20\,\mathrm{K}$ (circular island) is visible and pronounced. This is suggestive of a more general possibility of expansion-induced reentrant static friction peaking around a commensurate phase.

We note as an aside that since incommensurability relative to 6/7 switches from overdense below 22 K to underdense above, the solitons are replaced in the process by antisolitons, entities which unlike solitons flow in the opposite direction to the applied force. The antisolitons being essentially lines of vacancies in the 2D lattice, their properties differ quantitatively from those of solitons, which are lines of interstitials. Antisolitons are generally of narrower width and less mobile, as seen for example in simulated sliding colloid monolayers [131], another system where some of the present results could in the future be verified – although the nature and pinning role of boundaries may be quantitatively different in that case. Although the resulting quantitative asymmetry between underdense islands (with stronger static friction) and overdense ones (with weaker static friction) should not directly affect the critical exponents, it might do so indirectly by affecting differently the island edge shape and rugosity. The above was for incommensurate islands. Very large at low temperatures the static friction of a commensurate island is crucially temperature dependent. It requires the thermal nucleation of a forward displaced domain. The activation time t_a for nucleation is expected to behave as in the edge-free bulk case [148, 149]

$$t_a \sim C \exp(E_b/k_B T) \tag{4.6}$$

where E_b is the effective activation energy barrier, lowered by the applied external force, and dependent on the nucleation site. The time evolution of the particles' trajectories shows that the island slides upon the temperature-related appearance of the nucleus at the island edge, followed by a subsequent force-driven expansion. Here once again the edge plays an important role, even if different, in commensurate island static friction. Nucleation at the edge implies that (owing to greater atom mobility) there is a lower edge value E_b^e of the barrier relative to the bulk barrier E_b which controls homogeneous nucleation [148]. Since t_a establishes the threshold of depinning, one obtains for commensurate islands of increasing size a constant t_a, i.e. a constant E_b, only if the applied force grows linearly with N, and therefore is $F_s \propto A$, or $\gamma_s = 1$, exactly like in homogeneous nucleation. We note incidentally that the same bulk-like static friction scaling exponent $\gamma_s = 1$ should also occur for "soft" incommensurate islands, whose free sliding is dynamically unaccessible [95]. By contrast, for hard incommensurate islands the external force is resisted only by the edge pinning barrier, and therefore F_s will grow at most as $\sqrt{A}$ for a constant E_b^e. In real incommensurate islands the inhomogeneous stress along the edge further reduces E_b at specific points, causing the above-discussed sublinear size scaling of F_s with $\gamma_s < 1/2$.

4.6   Final remarks

We have conducted, in summary, a simulation study of atomistic sliding exhibiting static friction, an important tribological parameter whose physics had been, despite specific case studies [118, 148, 149, 177–181, 197], still insufficiently addressed so far for weak incommensurate contacts. With an eye to adsorbed rare gases typical of QCM experiments we simulated the forced depinning of islands, and found that the island edges play an all-important role, blocking especially the onset of otherwise superlubric sliding below a critical diameter. For rare gas islands inertially pushed on metal substrates, the edge-originated static friction is relevant, hindering the low temperature sliding of islands whose interior would otherwise be superlubric. Static friction is predicted for these islands to obey a sublinear scaling growth with island area, with an exponent roughly between 0.25 and 0.37, depending on the island shape. Previous work by Sorensen et al. [197] showed some effects due to edges of an AFM-like sliding of a Cu tip on a Cu surface. More

recently, the *dynamic* sliding friction, in principle a different quantity from static friction, was studied in nanomanipulation experiments by Schirmeisen's group and found to obey a sublinear scaling laws [155].

That raises the conceptually interesting question of what should be the mutual relationship between the evolution of static and dynamic friction when size grows. This question is presently open, since it is hard to extract reliable dynamic friction size scaling from simulations, whereas conversely the experiments cannot directly address the static friction and its scaling laws. The lack of distinction found in some literature between static and dynamic friction remains in need of justification. The dynamic friction force F of a hard incommensurate island will consist of $F_b + F_e$, namely a bulk term plus an edge term. The edge term F_e should size-scale sublinearly like static friction with an exponent smaller than $1/2$, and will in case of stick-slip also imply a sublinear dependence upon center-of-mass sliding speed. The bulk term F_b (vanishing in the static case) should conversely reflect superlubricity, with a linear, viscous speed dependence, and a bulk-like size scaling exponent $\gamma = 1$. For large speed and large island size the bulk dynamic friction will eventually prevail, with a size dependence very different from that of static friction. At much lower speed and at moderate size the bulk contribution should become less important, until eventually both static and dynamic friction should become edge-dominated, with a similar sublinear size scaling.

It will be very interesting to watch a future expansion of experimental data to verify if static friction will follow scaling laws we find here, with possible modifications when islands are replaced by metal clusters with considerably more rigid edges and stronger contacts, or in the case of 2D colloids, where edges may be completely different. The possible future use of QCM substrates with controlled size terraces, obtained e.g. by vicinal surfaces, should enable a verification of the static friction phenomena described here. The dependence of the static friction upon temperature is another result that could be experimentally pursued, while an estimate of the substrate corrugation magnitude, a generally unknown parameter, could be obtained by comparing data and simulations. More generally, the role of the edges of incommensurate sliding islands and clusters, not sufficiently emphasized until recently, must be acknowledged as an important source of static friction.

Discussion and Conclusions

In this thesis I have addressed the problem of nanoscale friction between dry crystalline surfaces. The focus has been the study of the tribological properties of low dimensional *incommensurate* interfaces. In view of future experiments, I have performed molecular dynamics (MD) simulations of artificial toy-models. This choice has the advantage, with respect to conventional tribological systems, to allow for realistic MD simulations directly comparable with experiments. I considered three case studies: (i) the sliding of one dimensional (1D) chains of cold ions in presence of a laser-induced periodic potential, (ii) two dimensional (2D) colloidal monolayers interacting with a 2D periodic optical lattice, (iii) rare-gas atoms islands physisorbed on hard, clean metallic substrates. The results of the numerical investigations have been presented respectively in Chapter 2, 3, 4, and are summarized below.

Chapter 2. Trapped cold-ion chains have been proposed in early works [78, 130] as tools for applications in nanotribology. These studies focused mainly on statics, in particular the connection between the structural properties of the ground state and static friction. A glimpse to the weakly dissipative sliding at small substrate "corrugation" strengths U_0 was given in Ref. [78], where the predicted [75] quadratic increase of dissipation with U_0 was observed. In this chapter I presented a systematic study of the dynamical properties of the chain over a wide range of corrugations, showing results that suggest how trapped cold ions in an optical lattice can be of help in understanding stick-slip friction, and also the way friction changes when one of the sliders undergoes structural transitions. For that scope, I simulated a 101-ions chain, driven to slide back and forth by a slowly oscillating electric field in an incommensurate periodic potential of increasing magnitude U_0. The chain sliding is found to switch, as U_0 increases, before the "vestigial" Aubry transition of the finite chain [78], from a smooth-sliding regime with low dissipation to a stick-slip regime with high dissipation. In the stick-slip regime the onset of overall sliding is preceded by precursor events consisting of partial slips of few ions only, leading to partial depinning of the chain, a nutshell remnant of precursor events at the onset of motion also observed in macroscopic sliders. Cold ion chains also provide a tool to explore the effects on friction of a structural transition. By reducing the trapping potential aspect ratio, the ion chain shape turns from linear to a planar zigzag configuration. Simulations show that dynamic friction rises at the transition, reflecting the opening of newer dissipation channels.

Chapter 3. Two-dimensional colloidal monolayers sliding over a laser-induced optical lattice, recently emerged as powerful artificial systems for the study of friction between ideal crystalline surfaces. In recent breakthrough experiments, Bohlein and coworkers observed for the first time the motion of solitons, and studied the dynamics of colloid/optical-lattice interfaces with different geometries [120]. Subsequent numerical works further demonstrated the potential applications of colloidal crystals in nanotribology. Using realistic MD simulations, Vanossi and collaborators [131] uncovered the depinning mechanism of commensurate colloidal islands. Moreover, they

pointed out the existence of a threshold value of the substrate corrugation strength U_0 for the onset of static friction in incommensurate interfaces. These simulations gave general insights on the physics of the sliding interface, but several aspects remained uninvestigated. In this chapter I characterized in details the statics and dynamics of mismatched interfaces, highlighting the relations between the ground state configuration and the ensuing static and dynamic friction of the monolayer. To this aim I performed extensive MD simulations, investigating the tribological properties of the interface as a function of the external load U_0.

Simulation results predict two important novelties, one in the static equilibrium structure, the other in the frictional behavior under sliding. Structurally, realistic simulations show that the colloid layer should possess in full equilibrium a small misalignment rotation angle θ_{opt} relative to the optical lattice, an effect so far unnoticed but visible in some published experimental moiré patterns. This misalignment angle increases the degree of interdigitation of the monolayer within the substrate, which in turn has the effect of boosting the colloid monolayer dynamic friction by a considerable factor over the hypothetical aligned case discussed so far in the literature. A frictional increase of similar origin must generally affect other incommensurate adsorbed monolayers and contacts, to be sought out case by case.

If the colloid and the optical lattices are mutually commensurate, the colloid sliding is always pinned by static friction; but when they are incommensurate the presence or absence of pinning depends upon the system parameters. If a 2D analogy to the mathematically established Aubry transition of one-dimensional systems were to hold, an increasing periodic corrugation strength U_0 should turn an initially free-sliding, superlubric colloid into a pinned state, where the static friction force goes from zero to finite through a well-defined dynamical phase transition. Realistic simulations predict the existence of a clear and sharp superlubric-pinned transition for increasing corrugation strength. Unlike the 1D Aubry transition which is continuous, the 2D transition exhibits a definite first-order character, with a jump of static friction. With no change of symmetry, the transition entails a structural character, with a sudden increase of the colloid-colloid interaction energy, accompanied by a compensating downward jump of the colloid-corrugation energy. The transition value for the corrugation amplitude U_0 is found to depend upon the misalignment angle θ between the optical and the colloidal lattices, superlubricity surviving until larger corrugations for angles away from the energetically favored orientation θ_{opt}.

Chapter 4. One question that is routinely raised in nanotribology involves how static friction can be so ubiquitous when two clean interfaces in sliding contact are not expected to exhibit it. This is the case of weak contacts between hard *incommensurate* surfaces, where theory generally predicts superlubric behaviours. A possible answer was proposed [118] which involves "third bodies", mobile impurity atoms or molecules that act to initially pin the interface by inducing a sort of effective commensuration between the two surfaces. In the absence of contaminations, finite size effects can be responsible for locking. In the case study of *small* clusters, previous simulations [119] showed that the degree of commensurability rises from a competition between interfacial and elastic interactions, and depends sensitively on the size. Pinning in this case increases with decreasing cluster size and the clusters eventually become nearly commensurate and therefore strongly pinned at a critical size.

A long-standing puzzle is represented by hard incommensurate interfaces formed by *large* rare-gas solid islands physisorbed on highly clean metallic crystalline substrates. These systems are expected to be superlubric, yet QCM experiments generally show a finite barrier preventing the onset of global sliding at sufficiently small oscillation amplitudes. In this chapter I presented extensive numerical investigations, modeled with parameters describing Kr/Pb(111), which highlight the role of the island's edges in determining the residual static friction of this system. The

static friction force is found to increase with the size A of the island as A^γ, with $\gamma < 1/2$. This result indicates that the pinning barrier originates only from a reduced number of points lying on the islands' edges. This interpretation is supported by a detailed study of the atomic trajectories close to the onset of global sliding. Quantitative analysis further demonstrate that, in absence of other sources of pinning, this edge related barrier can be sufficient to explain the static friction observed in QCM experiments. Interestingly, similar subscaling laws were observed in experimental studies of the dynamic friction of nanoparticles [155]. The results obtained in the case study presented in this chapter thus raise the conceptually interesting question of what should be the mutual relationship between the evolution of static and dynamic friction when size grows. A question that is presently open, since it is hard to extract reliable dynamic friction size scaling from simulations, whereas conversely the experiments cannot directly address the static friction and its scaling laws.

To conclude, clean periodic artificial systems enable the detailed study of the intimate processes going on between sliding crystalline surfaces. In particular the ability to perform directly comparable experimental and theoretical investigations provides a unique opportunity to shed new light on the relevant mechanisms that contribute to kinetic energy degradation, and sticking. Understanding the sliding of ideal crystalline interfaces, where the main sources of friction are due to geometric locking and phononic dissipation, represents the first step towards the control of friction in nanoscale devices. The investigations reported in this thesis highlighted the role played by finite size effects, misfit rotations, and slider elasticity and inhomogeneity in determining the static and dynamic properties of incommensurate interfaces, which are currently attracting a lot of interest because of their relevance in solid lubrication.

There are several other topics that the systems described in this thesis would allow to address. Colloidal monolayers appear to be in this sense the most flexible tool. Possible lines of future research include the study of time-dependent nonlinear phenomena, such as Shapiro steps in driven monolayers, or lubricant speed quantization phenomena. Even more interesting from a tribological point of view would be the possibility to study stick-slip motion in extended 2D contacts. This should be achievable in large colloidal islands by choosing a proper way to drive the monolayer, which must induce the mechanical instabilities at the base of the sudden transition from sticking to sliding. Another possible research line is the study of aging, which is responsible for the build-up of static friction after each slip event. Plastic deformations leading to a better interdigitation of two touching bodies is one of the mechanism underlying the increase of static friction with time in macroscopic sliders. Colloidal monolayers could serve in this sense as an ideal realization of a dry and chemically-inert crystalline contact where locking between the two lattices is reached only via atomic relaxation of the colloids into the substrate potential landscape. While many of these phenomena remain open to investigations, other have already been addressed theoretically [198–202], and are waiting for experimental observation.
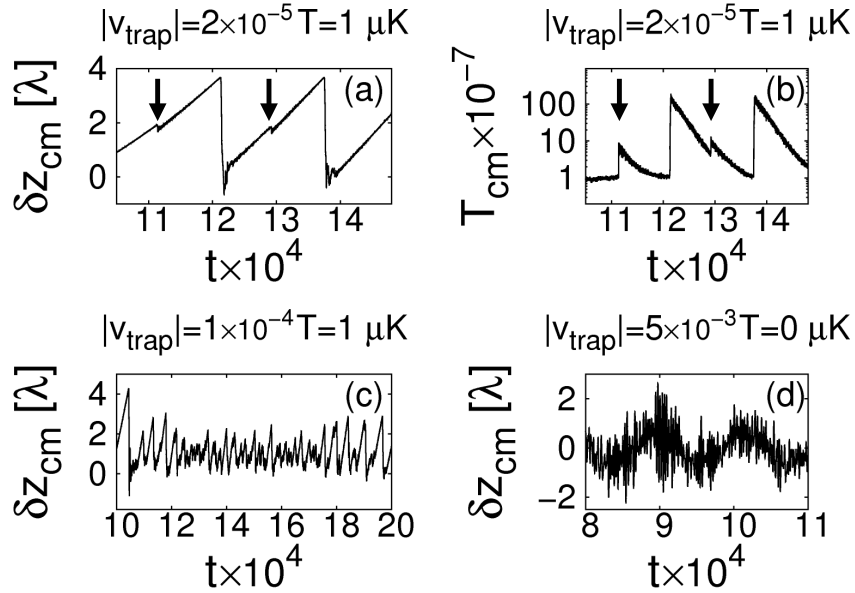
Sliding Cold Ion Chains

Figure A.1: 101-ions chain.
(a)δz_{cm} in the simulation at $|v_{trap}|=2\times10^{-5}$ and T=10^{-7} showing stick-slip and precursor events (indicated by the arrows) corresponding to partial slips of the central portion of the chain. (b)Temperature measured in the center of mass frame in the simulation of panel (a). After each slip event the internal temperature is raised and then it is exponentially damped by the thermostat. Precursor events give rise to the smaller peaks indicated by the arrows. This trend is always observed in the stick-slip regime. (c)For $|v_{trap}|=10^{-4}$ and T=10^{-7} the dynamics is chaotic. Slips of different magnitude occur as the pulling velocity changes during each oscillation. (d)Further increasing $|v_{trap}|=5\times10^{-3}$ the dynamics finally turns into a smooth-sliding regime, even at T=0.

A.1 Practical parameter choice

In real experiments, in order to create an optical lattice, the laser wavelength must fit one of the electronic transition of the chosen ions. For Ca$^+$ the S$_{1/2}$-P$_{1/2}$ transition at 397 nm is naturally exploited, leading to a lattice spacing $\lambda \approx 200$ nm, while an achievable amplitude for
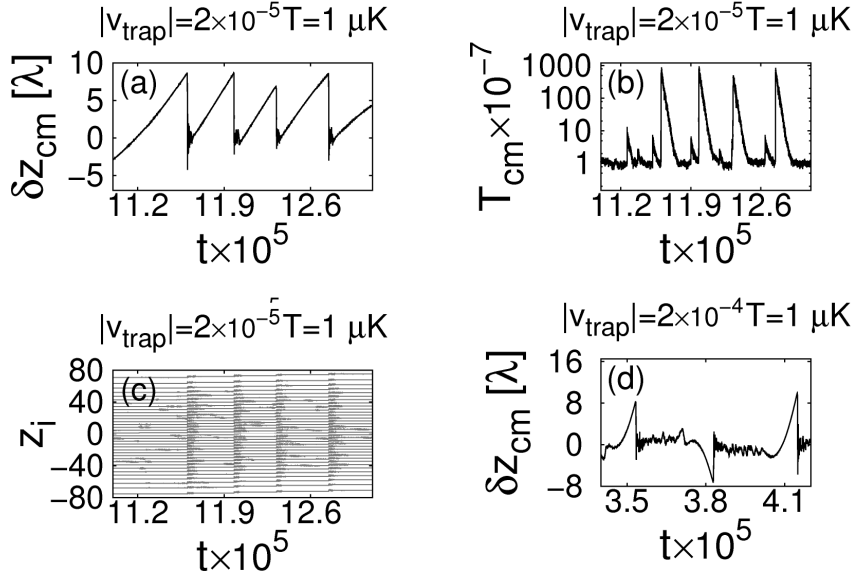
Figure A.2: 35-ions chain.
(a)δz_{cm} in the simulation at $|v_{trap}|=2\times10^{-5}$ and T=10^{-7}. An irregular stick-slip regime is observed. (b)Temperature measured in the center of mass frame in the simulation of panel (a). The highest peaks correspond to the main slip events, slip of few ions within the chain give rise to the smaller ones. (c)Trajectory of each ions during some slip events of the simulation of panels (a) and (b). The chain slip as a whole and precursor events are not observed due to the small size of the system. (d)δz_{cm} in the simulation at $|v_{trap}|=2\times10^{-4}$ and T=10^{-7}. At the inversions of motion the chain is pinned; owing to the small initial pulling velocity a sharp slip event occurs after which smooth sliding begins.

the corrugation potential is of the order of 10^{-27} J. Considering a transverse trapping frequency $\omega_\perp = 2\pi\times4$ MHz then one gets (in dimensionless units) $\lambda = 0.115$, $U_0 = 2.31\times10^{-5}$. A practically achieved temperature is 1 μK corresponding to $T = 10^{-7}$, in simulation units. Setting an aspect ratio $R = 0.0005$ one has $a_o \approx 16\ \lambda$, therefore ions are separated by several lattice spacings, corresponding to a much "weaker" kind of incommensurability that the golden ratio used in the results discussed so far. Moreover for such a small value of U_0 the chain is almost free to slide, in this case also the two extremities being weakly anchored to the substrate. Stick-slip is therefore expected to occur only at very small pulling velocities when, after each slip, the chain is allowed to relax in a new metastable pinned configuration. We performed simulations at the experimental parameters for the 101-ions and a 35-ions chain. We chose $\gamma = 0.0005$ and we used a Langevin thermostat for the simulations at finite T. We also set Ω and E_0 in order to test different average velocities of the moving confining parabola. Let us consider first the 101-ions chain. At very low pulling velocity we observed stick-slip motion, the slip amplitude being of the order of a few lattice parameters (see Fig. A.1a). The dynamics of the slip events is simple and no longer shows the variety of features described for the golden ratio incommensurability. The pinned chain remained stable upon pulling until a weak compression generated within the chain propagates toward the head. Simple precursor events are observed consisting of partial slips of a central portion of the chain at fixed extremities. Figure A.1b shows the temperature T_{cm} measured in the center of mass frame, displaying the expected inverse sawtooth behavior when plotted in a semilogarithmic scale. After each slip T_{cm} increases, and is then exponentially

damped by the thermostat. As the pulling velocity is increased the dynamics turns gradually into a smooth-sliding regime, as shown in Fig. A.1c,d. Chains of a few tens of ions may be more easily stabilized inside a trap. We performed simulations with a 35-ions chain, using the same parameters as above. In this case the central ion-ion spacing is larger and corresponds to $a_o \approx 30$ λ. As shown in Fig. A.2a we observed that stick-slip motion is again preserved in this case as well for small enough average pulling velocities. The slip amplitude is larger than that observed for the 101-ions chain indicating a stronger pinning to the substrate, as is reasonable to expect given a larger prevalence of extremities. From the plot of the temperature of Fig. A.2b we see that small adjustments of the inner ions occur, which give rise to small peaks in T_{cm}, however without proper precursor events due to the reduced size of the chain.

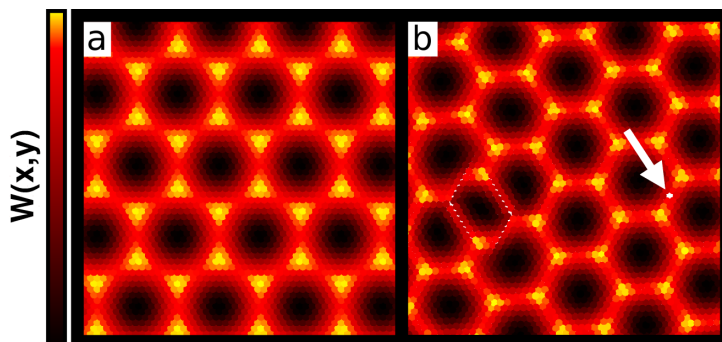# Equilibrium Misalignment and Dissipation in Colloidal Monolayers

Figure B.1: A small region of the particle system optimized at rest in *pbc*. Particles are colored according to the local substrate potential $W(x, y)$. (a) Aligned ($\theta = 0$) configuration obtained at $U_0 = 0.09$. (b) Configuration obtained at $U_0 = 0.18$, showing a spontaneous misalignment angle $\theta \simeq 2.3°$, whose effect is greatly magnified in the corresponding moiré pattern, rotated by $\psi \approx 30°$ with respect to (a). An extended defect (at the left side) and a vacancy (pointed at by the arrow) appear, adapting the misaligned particle lattice to the constraint introduced by the *pbc*.

B.1   Spontaneous misalignment in *pbc* simulations

We briefly comment here about results regarding the static properties of incommensurate mono-layers obtained in *pbc*, which further demonstrate the strong tendency of the colloidal crystal to develop, in full equilibrium, a misalignment angle with respect to the substrate potential lattice. Equilibrium configurations at different values of U_0 were generated as follows. We started with a perfect colloidal crystal at $\theta = 0$ at fixed $\rho = 89/94$. A first series of zero-temperature ($T = 0$) damped molecular-dynamics simulations was carried out increasing the substrate potential amplitude in steps $\Delta U = 0.01$ from $U_0 = 0 \rightarrow 0.5$, relaxing the monolayer at each step until no appreciable movement of the colloids was observed. A second series of configurations was generated starting with a corrugation amplitude $U_0 = 0.5$, decreasing it in steps $\Delta U = -0.05$ down to $U_0 = 0$ and performing an annealing protocol from $T = 1 \rightarrow 0$ at each step. The stability of each of these annealed structures was subsequently tested by further carrying out parallel
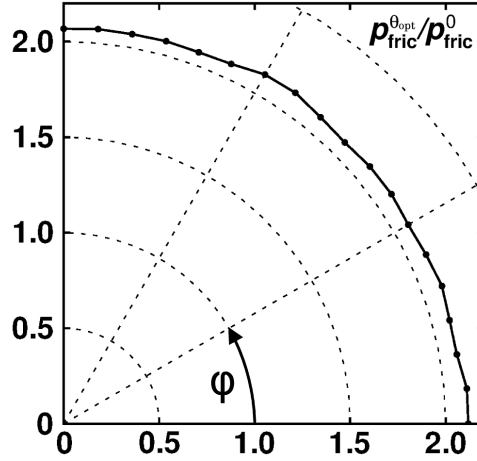
Figure B.2: The polar plot shows the ratio $p_{\mathrm{fric}}^{\theta_{opt}}/p_{\mathrm{fric}}^{0}$ between the dynamic friction of the aligned ($\theta = 0$) and optimally rotated ($\theta_{\mathrm{opt}} = 4°$) monolayers in *obc* as a function of the direction φ of the driving force F_{d}. Results refer to simulation parameters $F_d = 0.36$, $U_0 = 0.27$, $\rho = 0.927$. In general we found p_{fric} to be independent on φ on the whole range $[0, 2\pi]$ and for any island orientation θ.

$T = 0$ relaxations varying the corrugation amplitude in steps $\Delta U = \pm 0.01$ (both upward and downward), until $U_0 = 0$ or $U_0 = 0.5$ were reached. For each value of U_0, among all the configurations generated from these two procedures we eventually selected the one with the lowest total energy. The resulting lowest-energy configuration is usually aligned for small corrugation U_0, and develops spontaneous misalignment, see Fig. B.1, above a certain corrugation threshold. Since *pbc* are satisfied by a perfect lattice only at $\theta = 0°$ an extended defect must be accommodated in the rotated monolayer. Of course, both signs of $\theta = \pm 2.3°$ should be found with equal probability in a sufficiently large statistics of configurations. In practice we did not pursue this sign statistics, and concentrated on a single series of configurations, conventionally with positive misalignment angle. Only above $U_0 = 0.17$ the cost of the defect is overcompensated by the better interdigitation occurring at $\theta = 2.3°$. This threshold value is size dependent since the energy cost of the defect relative to the energy gained by the interaction with the substrate decreases with increasing supercell size. In agreement with that, we found that at smaller sizes the aligned configurations survive up to larger values of U_0. The defect artifacts introduced by *pbc* are overcome in the *obc* simulations, where rotations and misalignment can occur unimpeded and the angular degree of freedom is more easily explored, as discussed in the Section 3.3.

B.2   Dissipation at different driving force orientations

All the results reported in Section 3.3 were obtained by dragging our model island monolayer along the x-axis, corresponding to a high symmetry crystalline direction of the substrate potential. We verified that this arbitrary choice does not induce artifacts by performing simulations varying the direction φ of the external driving force F_d. The results are shown in Fig. B.2. We found that p_{fric} is almost independent of the direction of F_d for any monolayer orientation θ, and so it is the increase of dynamic friction at the optimal misalignment θ_{opt} with respect to the aligned case $\theta = 0$.
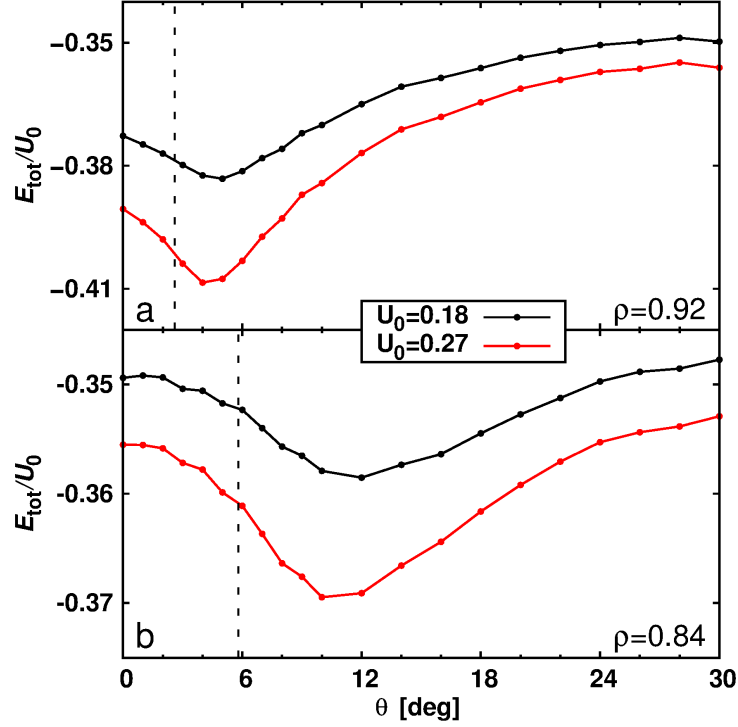
Figure B.3: Static structure optimization. Total energy per particle as a function of the misalignment angle θ for two different incommensurate mismatched ratios $\rho = 0.927$ (a) and $\rho = 0.84$ (b), obtained after optimization in *obc* at different corrugations $U_0 = 0.18, 0.27$. In both cases the preferred orientation involves a small but nonzero misalignment angle with respect to the periodic lattice potential. Vertical dashed lines indicate the theoretical Novaco-McTague angle expected from Eq. (3.10).

B.3   Static and dynamic properties at different mismatch ratios

As a test on the general conditions under which rotational epitaxy is expected to occur in our model *obc* island we considered three different values of the lattice mismatch ratio $\rho = 0.84$, 0.927, 1.08 and searched for the minimum of the total energy as a function of the misfit angle θ. Figure B.3 reports results obtained in the two distinct underdense incommensurate cases $\rho < 1$. The full range $0 < \theta < 30°$ of independent values of θ is considered, demonstrating the existence of a unique minimum θ_{opt}, not considering the equivalent angles at $\theta_{\text{opt}} + k\pi/3$. In all cases θ_{opt} is found to be somewhat larger than the corresponding Novaco-Mc Tague orientation $\theta_{\text{NM}} = 2.6°$, 5.8°, expected from Eq. (3.10), respectively for $\rho = 0.927, 0.84$. Figure B.4 displays the total energy as a function of θ for the overdense $\rho = 1.08$. The theoretical NM angle is $\theta_{\text{NM}} = 2.6°$. The minimum is found in correspondence of $\theta_{\text{opt}} \simeq 3°$, closer to the expected value than what was found in the underdense regimes. In this overdense case, moving toward the periphery the average colloid spacing tends to get commensurate to the corrugation potential, favouring smaller epitaxial angles.

Let us consider now dissipation under sliding of our model monolayer island. In the overdense regime the misfit stress is confined in local compressions rather than dilations. Due to the exponential form of the repulsive interaction the cost of compressions is higher, so that, at equal corrugation U_0, distortions are weaker than in the underdense case. Consequently the dissipative
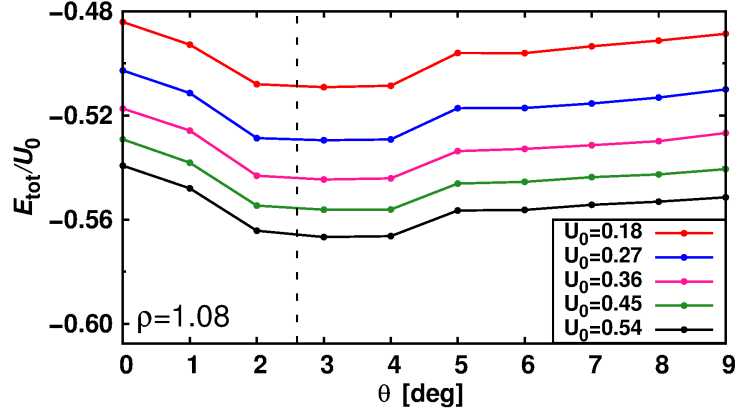
Figure B.4: Static structure optimization. Total energy per particle as a function of θ obtained in *obc* at the overdense $\rho = 1.08$, for different corrugations U_0. The dashed line indicates the expected value $\theta_{NM} \simeq 2.6°$ from Eq. (3.10).

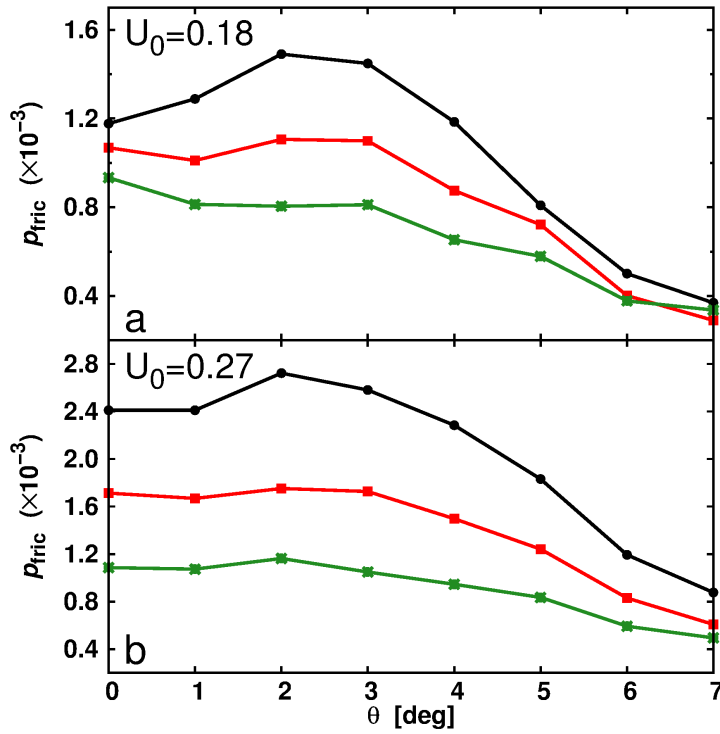**Figure B.5:** Sliding dynamics in *obc*. Dissipated friction power p_{fric} as a function of θ obtained at $\rho = 1.08$, driving forces $F_d = 0.18,\ 0.27,\ 0.36$, corrugation $U_0 = 0.18$ (a), $U_0 = 0.27$ (b), and $T = 0$.

sliding of the aligned and optimally tilted configuration is not very different and the difference in p_{fric} is reduced compared to the underdense regime. Nonetheless, far away from θ_{opt} a significant drop of the dynamic friction is still observed, as shown in Fig. B.5.
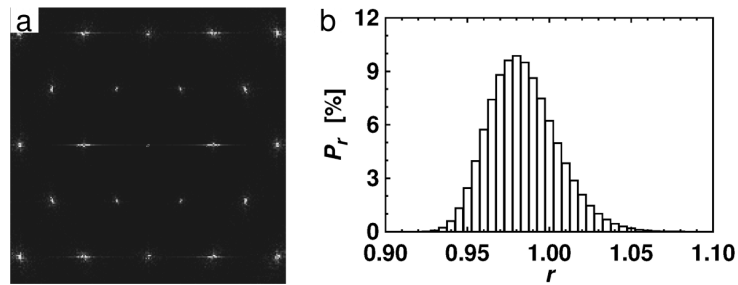
Figure B.6: (a) Structure factor calculated considering a central circular region of radius $R = 40$ of the island in *obc* equilibrated at T_{room}, $U_0 = 0$, $\rho = 0.927$. (b) Distribution P_r of the nearest neighbor distance in the central region of the island at T_{room}. The asymmetry of the distribution toward large values of r is due to the inhomogeneity of the island.

B.4   Temperature effects

The Novaco-Mc Tague harmonic theory [151] assumes zero temperature. Without attempting a rigorous investigation of the problem here we anticipate, based on Eq. (3.10) and on finite-temperature simulations, that thermal effects do not affect the main conclusions obtained at $T = 0$, presented in Section 3.3.

Within a mean-field theory, such as a quasi-harmonic approximation, one may still use $T = 0$ results with thermally renormalized constants. The two parameters defining θ_{NM} are the mismatch ratio $\rho = a_l/a_c$ and the sound velocity ratio $\eta = c_L/c_T$. The mismatch ratio is under control as one can always set the desired incommensuration by fixing the average lattice spacing $\langle a_c \rangle$. Of course a_c will be characterized by a broader distribution at $T \neq 0$. Changes in the sound velocities are also irrelevant if the effects of temperature on the crystal properties act simply as a renormalization of the 2-body interaction. Under this hypothesis η is expected to be weakly affected since, as it turns out, its value is mainly determined by the symmetries of the lattice [1]. Therefore in a mean-field treatment, the rotated epitaxy is expected to survive with only quantitative changes related to lattice thermal expansion.

The peak in the dynamic friction is connected with the increased interdigitation of the monolayer within the substrate occurring at θ_{opt}. At the optimal angular orientation solitons are enhanced, which is reflected in the larger distortions observed in the colloidal crystal (Fig. 3.8, 3.10), and their motion is more dissipative. At room temperature ($k_B T_{\text{room}} \approx 0.04$ in simulation units) we observed that such solitonic superstructures are preserved for corrugations $U_0 > 0.1$ and dynamic friction does indeed increase near the optimal misalignment. We performed simulations at T_{room} adopting a conventional Langevin approach in our model monolayer in *obc*. Starting configurations are generated first by equilibrating the island at zero corrugation $U_0 = 0$. The crystalline order of the system is preserved at room temperature, as shown in Fig. B.6. Actually thermal effects are very weak as one can see from the relatively small broadening of the distribution P_r of the nearest neighbor distances. This is due to the fact that the interparticle interaction at a_c is already of order $\sim k_B T_{\text{room}}$ and it increases exponentially at smaller distances.

We then set a mismatch ratio $\rho = 0.927$ and rotated the monolayer at various misalignment angles $\theta = 0 \rightarrow 10°$, equilibrating each configuration at $U_0 = 0.18, 0.27$. At finite temperature,

---

[1]For any pair potential displaying a minimum and considering only nearest neighbors interactions, in a 2D triangular lattice $c_L/c_T = \sqrt{3}$ is an exact result. Within the nearest-neighbors approximation the same result holds for the Yukawa potential of our interest for $a_c \gg \lambda_D$, a condition generally satisfied in actual experiments.
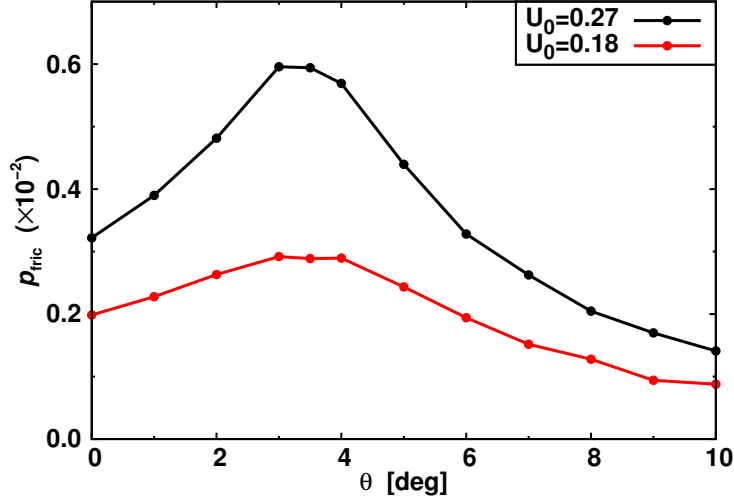
Figure B.7: The dissipated friction power p_{fric} as a function of θ at T_{room}. Simulations have been performed in *obc*, fixing $\rho = 0.927$, driving force $F_d = 0.36$ and corrugations $U_0 = 0.18, \ 0.27$.

running a sufficiently long simulation, the monolayer should rotate spontaneously toward its optimal angular orientation. In practice in no simulations we did observe any appreciable change in the orientation of the crystal. Thus, the main result here is that the simulated dependence of the average energy confirms the persistence of the epitaxial rotation at finite temperature.

Figure B.7 shows the dissipated power p_{fric} as a function of the misalignment angle θ for two intermediate substrate corrugations $U_0 = 0.18, \ 0.27$ and driving force $F_d = 0.36$. Similar to the results at $T = 0$ a friction peak arises at $\theta = 3° - 4°$, corresponding to the ($T = 0$) optimal orientation of the colloidal monolayer. Thus the friction boost caused by the epitaxial rotation survives at finite temperature, of course in a regime where the colloid is still "solid" and not fluid. The peak in the dynamic friction is connected with the increased interdigitation of the monolayer within the substrate occurring at θ_{opt}.

Bibliography

[1] H. P. Jost, Wear **136**, 1 (1990).

[2] J. Heyman, *Coulomb's memoir on statics: an essay in the history of civil engineering* (World Scientific, Singapore, 1998).

[3] T. E. Madey, J. Vac. Sci. Tech. A **2**, 110 (1984).

[4] L. A. Harris, J. Appl. Phys. **39**, 1419 (1968).

[5] F. Hofmann and J. Toennies, Chem. Rev. **96**, 1307 (1996).

[6] P. Palmberg and W. Peria, Surf. Sci. **6**, 57 (1967).

[7] R. E. Weber and W. T. Peria, J. Appl. Phys. **38**, 4355 (1967).

[8] D. Tabor and R. H. S. Winterton, Nature **219**, 1120 (1968).

[9] F. B. Bowden and D. Tabor, *The friction and lubrication of solids* (Oxford University Press, New York, USA, 1950).

[10] F. Heslot, T. Baumberger, B. Perrin, B. Caroli, and C. Caroli, Phys. Rev. E **49**, 4973 (1994).

[11] M. Urbakh and E. Meyer, Nature Mat. **9**, 8 (2010).

[12] J. N. Israelachvili, J. Colloid Interface Sci. **44**, 259 (1973).

[13] Y. L. Chen, T. Kuhl, and J. Israelachvili, Wear **153**, 31 (1992).

[14] M. Heuberger, G. Luengo, and J. Israelachvili, Langmuir **13**, 3839 (1997).

[15] R. M. Pashley, J. Colloid Interface Sci. **83**, 531 (1981).

[16] R. M. Pashley, Adv. Colloid Interface Sci. **16**, 57 (1982).

[17] R. G. Horn, D. T. Smith, and W. Haller, Chem. Phys. Lett. **162**, 404 (1989).

[18] R. G. Horn, D. R. Clarke, and M. T. Clarkson, J. Mater. Res **3**, 413 (1988).

[19] W. W. Merrill, A. V. Pocius, B. V. Thakker, and M. Tirrell, Langmuir **7**, 1975 (1991).

[20] A. Dhinojwala and S. Granick, Macromolecules **30**, 1079 (1997).

[21] J. Klein, J. Chem. Soc. Faraday Trans. I **79**, 99 (1983).

[22] S. Patel and M. Tirrell, Annu. Rev. Phys. Chem. **40**, 597 (1989).

[23] H. Watanabe and M. Tirrell, Macromolecules **26**, 6455 (1993).

[24] T. Kuhl, D. E. Leckband, D. D. Lasic, and J. N. Israelachvili, "Modulation and modeling of interaction forces between lipid bilayers exposing terminally grafted polymer chains", English, in *Stealth liposomes*, edited by F. M. D. Lasic, Handbooks in Pharmacology and Toxicology (CRC, 1995), pp. 73–91.

[25] J. Klein, Annu. Rev. Mater. Sci. **26**, 581 (1996).

[26] M. Ruths, D. Johannsmann, and W. K. J. Rühe, Macromolecules **33**, 3860 (2000).

[27] C. A. Helm, J. N. Israelachvili, and P. M. McGuiggan, Science **246**, 919 (1989).

[28] Y. L. Chen, C. A. Helm, and J. N. Israelachvili, J. Phys. Chem. **95**, 10736 (1991).

[29] D. E. Leckband, J. N. Israelachvili, F.-J. Schmitt, and W. Knoll, Science **255**, 1419 (1992).

[30] J. Peanasky, H. M. Schneider, S. Granick, and C. R. Kessel, Langmuir **11**, 953 (1995).

[31] C. J. Coakley and D. Tabor, J. Phys. D **11**, L77 (1978).

[32] J. L. Parker and H. K. Christenson, J. Chem. Phys. **88**, 8013 (1988).

[33] C. P. Smith, M. Maeda, L. Atanasoska, H. S. White, and D. J. McClure, J. Phys. Chem. **92**, 199 (1988).

[34] S. J. Hirz, A. M. Homola, G. Hadziioannou, and C. W. Frank, Langmuir **8**, 328 (1992).

[35] J. M. Levins and T. K. Vanderlick, J. Phys. Chem. **96**, 10405 (1992).

[36] S. Steinberg, W. Ducker, G. Vigil, C. Hyukjin, C. Frank, M. Z. Tseng, D. R. Clarke, and J. N. Israelachvili, Science **260**, 659 (1993).

[37] G. Vigil, Z. Xu, S. Steinberg, and J. Israelachvili, J. Colloid Interface Sci. **165**, 367 (1994).

[38] M. Ruths, M. Heuberger, V. Scheumann, J. Hu, and W. Knoll, Langmuir **17**, 6213 (2001).

[39] J. Israelachvili, Y. Min, M. Akbulut, A. Alig, G. Carver, W. Greene, K. Kristiansen, E. Meyer, N. Pesika, K. Rosenberg, and H. Zeng, Rep. Prog. Phys. **73**, 036601 (2010).

[40] G. Sauerbrey, German, Zeitschrift für Physik **155**, 206–222 (1959).

[41] J. Krim and A. Widom, Phys. Rev. B **38**, 12184 (1988).

[42] L. Bardotti, P. Jensen, A. Hoareau, M. Treilleux, B. Cabaud, A. Perez, and F. C. S. Aires, Surf. Sci. **367**, 276 (1996).

[43] C. Mak and J. Krim, Phys. Rev. B **58**, 5157 (1998).

[44] J. Y. Park, Y. B. Qi, D. F. Ogletree, P. A. Thiel, and M. Salmeron, Phys. Rev. B **76**, 064108 (2007).

[45] J. Krim, D. H. Solina, and R. Chiarello, Phys. Rev. Lett. **66**, 181 (1991).

[46] A. Dayo and J. Krim, Int. J. Thermophys. **19**, 827 (1998).

[47] A. Dayo, W. Allnassallah, and J. Krim, Phys. Rev. Lett. **80**, 1690 (1998).

[48] M. Pierno, L. Bruschi, G. Fois, G. Mistura, C. Boragno, F. de Mongeot, and U. Valbusa, Phys. Rev. Lett. **105**, 016102 (2010).

[49] M. Pierno, L. Bignardi, M. C. Righi, L. Bruschi, S. Gottardi, M. Stohr, O. Ivashenko, P. L. Silvestrelli, P. Rudolf, and G. Mistura, Nanoscale **6**, 8062 (2010).

[50] T. Oda and M. Hieda, Phys. Rev. Lett. **111**, 106101 (2013).

[51] T. Coffey and J. Krim, Phys. Rev. B **72**, 235414 (2005).

[52] L. Bruschi, G. Fois, A. Pontarollo, G. Mistura, B. Torre, F. B. de Mongeot, C. Boragno, R. Buzio, and U. Valbusa, Phys. Rev. Lett. **96**, 216101 (2006).

[53] G. Binnig, C. F. Quate, and C. Gerber, Phys. Rev. Lett. **56**, 930 (1986).

[54] C. M. Mate, G. M. McClelland, R. Erlandsson, and S. Chang, Phys. Rev. Lett. **59**, 1942 (1986).

[55] E. L. Florin, V. T. Moy, and H. E. Gaub, Science **264**, 415 (1994).

[56] G. U. Lee, D. Kidwell, and R. J. Colton, Langmuir **10**, 354 (1994).

[57] H. Skulason and C. D. Frisbie, J. Am. Chem. Soc. **122**, 8750 (2000).

[58] M. Carrion-Vazquez, A. F. Oberhauser, S. B. Fowler, P. E. Marszalek, S. E. Broedel, J. Clarke, and J. M. Fernandez, Proc. Natl. Acad. Sci. USA **96**, 3694 (1999).

[59] R. J. Cannara, M. J. Brukman, K. Cimatu, A. Sumant, S. Baldelli, and R. W. Carpick, Science **318**, 780 (2007).

[60] D. F. Ogletree, J. Y. Park, M. Salmeron, and P. A. Thiel, Science **313**, 186 (2006).

[61] A. L. Weisenhorn, P. K. Hansma, T. R. Albrecht, and C. F. Quate, Appl. Phys. Lett. **54**, 2651 (1989).

[62] D. Dietzel, U. Schwarz, and A. Schirmeisen, "Nanotribological studies by nanoparticle manipulation", English, in *Fundamentals of friction and wear on the nanoscale*, edited by E. Gnecco and E. Meyer, NanoScience and Technology (Springer International Publishing, 2015), pp. 363–393.

[63] W. A. Ducker, T. J. Senden, and R. M. Pashlel, Nature **353**, 239 (1991).

[64] M. Kisiel, E. Gnecco, U. Gysin, L. Marot, S. Rast, and E. Meyer, Nat. Mat. **10**, 119 (2011).

[65] G. Tocci, L. Joly, and A. Michaelides, Nanoscale **14**, 6872 (2014).

[66] D. J. Evans and G. P. Morris, *Statistical mechanics of non-equilibrium liquids* (ANU E Press, Canberra, Australia, 2007).

[67] J. Lebowitz and E. Rubin, Phys. Rev. **131**, 2381 (1963).

[68] L. Bocquet and J. Barrat, Phys. Rev. E **49**, 3079 (1994).

[69] L. Bocquet and J. Barrat, J. Chem. Phys. **139**, 044704 (2013).

[70] B. N. J. Persson, E. tosatti, D. Furhmann, G. Witte, and C. Wöll, Phys. Rev. B **59**, 11777 (1999).

[71] M. Kisiel, F. Pellegrini, G. E. Santoro, M. Samadashvili, R. Pawlak, A. Benassi, U. Gysin, R. Buzio, A. Gerbi, E. Meyer, and E. Tosatti, Phys. Rev. Lett. **115**, 046101 (1963).

[72] A. Benassi, A. Vanossi, G. E. Santoro, and E. Tosatti, Phys. Rev. Lett. **106**, 256102 (2011).

[73] K. A. Müller, W. Berlinger, and F. Waldner, Phys. Rev. Lett. **21**, 814 (1968).

[74] S. M. Shapiro, J. D. Axe, G. Shirane, and T. Riste, Phys. Rev. B **6**, 4332 (1972).

[75] M. Cieplak, E. Smith, and M. Robbins, Science **265**, 1209 (1994).

[76] T. Coffey and J. Krim, Phys. Rev. Lett. **95**, 076101 (2005).

[77] A. Liebsch, S. Goncalves, and M. Kiwi, Phys. Rev. B **60**, 5034 (1999).

[78] A. Benassi, A. Vanossi, and E. Tosatti, Nature Comm. **2**, 236 (2011).

[79] A. Berman, W. Ducker, and J. Israelachvili, "Experimental and theoretical investigations of stick-slip friction mechanisms", English, in *Physics of sliding friction*, Vol. 311, edited by B. Persson and E. Tosatti, NATO ASI Series (Springer Netherlands, 1996), pp. 51–67.

[80] J. H. Dieterich, J. Geophys. Res. **116**, 790 (1978).

[81] L. Prandtl, Zeitschrift für Angewandte Mathematik und Mechanik **8**, 85 (1928).

[82] E. Gnecco, R. Bennewitz, T. Gyalog, C. Loppacher, M. Bammerlin, E. Meyer, and H.-J. Güntherodt, Phys. Rev. Lett. **84**, 1172 (2000).

[83] E. Riedo, E. Gnecco, R. Bennewitz, E. Meyer, and H. Brune, Phys. Rev. Lett. **91**, 084502 (2003).

[84] S. Stills and R. Overney, Phys. Rev. Lett. **91**, 095501 (2003).

[85] I. Barel, M. Urbakh, L. Jansen, and A. Schirmeisen, Phys. Rev. Lett. **104**, 066104 (2010).

[86] S. M. Rubinstein, G. Cohen, and J. Fineberg, Nature (London) **430**, 1005 (2004).

[87] S. M. Rubinstein, G. Cohen, and J. Fineberg, Phys. Rev. Lett. **98**, 226103 (2007).

[88] B. N. J. Persson, J. Chem. Phys. **115**, 3840 (2001).

[89] B. N. J. Persson, U. Tartaglino, E. Tosatti, and H. Hueba, Phys. Rev. B **69**, 235410 (2004).

[90] Y. Mo, K. T. Turner, and I. Szlufarska, Nature (London) **457**, 1116 (2009).

[91] B. N. J. Persson, Phys. Rev. B **51**, 13568 (1995).

[92] O. M. Braun and J. Röder, Phys. Rev. Lett. **88**, 096102 (2002).

[93] O. M. Braun, I. Barel, and M. Urbakh, Phys. Rev. Lett. **103**, 194301 (2009).

[94] O. M. Braun and E. Tosatti, Europhys. Lett. **88**, 48003 (2009).

[95] M. Peyrard and S. Aubry, J. Phys. Condens. Matter **16**, 1593 (1983).

[96] B. N. J. Persson, *Sliding friction* (Springer-Verlag, Berlin, Germany, 1998).

[97] A. Vanossi, N. Manini, M. Urbakh, S. Zapperi, and E. Tosatti, Rev. Mod. Phys. **85**, 529 (2013).

[98] A. Socoliuc, R. Bennewitz, E. Gnecco, and E. Meyer, Phys. Rev. Lett. **92**, 134301 (2004).

[99] O. M. Braun and Y. Kivshar, *The frenkel-kontorova model: concepts, methods, and applications* (Springer-Verlag, Berlin, Germany, 1998).

[100] O. M. Braun, A. R. Bishop, and J. Röder, Phys. Rev. Lett. **79**, 3692 (1997).

[101] S. Aubry and P. Y. Le Daeron, Physica D **8**, 381 (1983).

[102] K. Shinjo and M. Hirano, Surf. Sci. **283**, 473 (1993).

[103] M. Hirano, "Superlubricity of clean surfaces", English, in *Superlubricity*, edited by A. Erdemir and J.-M. Martin (Elsevier, 2007), pp. 17–37.

[104] L. Consoli, H. J. F. Knops, and A. Fasolino, Phys. Rev. Lett. **85**, 302 (2000).

[105] M. Hirano, K. Shinjo, R. Kaneko, and Y. Murata, Phys. Rev. Lett. **67**, 2642 (1991).

[106] M. Hirano, K. Shinjo, R. Kaneko, and Y. Murata, Phys. Rev. Lett. **78**, 1448 (1997).

[107] L. Rapoport, Y. Bilik, Y. Feldman, M. Homyonfer, S. R. Cohen, and R. Tenne, Nature (London) **387**, 791 (1997).

[108] I. L. Singer, MRS Bull. **23**, 37 (1998).

[109] K. J. W. J. A. Heimberg, I. L. Singer, and A. Erdemir,

[110] Z. Liu, J. Yang, F. Grey, J. Z. Liu, Y. Liu, Y. Wang, Y. Yang, Y. Cheng, and Q. Zheng, Phys. Rev. Lett. **108**, 205503 (2012).

[111] M. Dienwiebel, G. Verhoeven, N. Pradeep, J. Frenken, J. Heimberg, and H. Zandbergen, Phys. Rev. Lett. **92**, 126101 (2004).

[112] J. M. Martin, C. Donnet, L. M. Th., and T. Epicier, Phys. Rev. B **48**, 10583 (1993).

[113] M. Dienwiebel, N. Pradeep, G. Verhoeven, H. Zandbergen, and J. Frenken, Surf. Sci. **576**, 197 (2005).

[114] G. Verhoeven, M. Dienwiebel, and J. Frenken, Phys. Rev. B **70**, 165418 (2004).

[115] C. Donnet, J. M. Martin, and T. Le Mogne, Tribol. Int. **29**, 123 (1996).

[116] A. Filippov, M. Dienwiebel, J. W. Frenken, J. Klafter, and M. Urbakh, Phys. Rev. Lett. **100**, 046102 (2008).

[117] Y. Liu, F. Grey, and Q. Zheng, Scientific Reports **4**, 4875 (2014).

[118] G. He, M. Muser, and M. Robbins, Science **284**, 1650 (1999).

[119] M. Reguzzoni and M. C. Righi, Phys. Rev. B **85**, 201412 (2012).

[120] T. Bohlein, J. Mikhael, and C. Bechinger, Nat. Mater. **11**, 126 (2012).

[121] T. Pruttivarasin, M. Ramm, I. Talukdar, A. Kreuter, and H. Häffner, New Jour. of Phys. **13**, 075012 (2011).

[122] A. Benassi, J. Schwenk, M. M. A., H. J. Hug, and D. Passerone, Adv. Mater. Interfaces **1**, 1400023 (2014).

[123] L. Kantorovich, Phys. Rev. B **78**, 094304 (2008).

[124] X. Li and W. E, Phys. Rev. B **76**, 104107 (2007).

[125] A. Benassi, A. Vanossi, G. Santoro, and E. Tosatti, Tribol. Lett. **48**, 41 (2012).

[126] R. Car and M. Parrinello, Phys. Rev. Lett. **55**, 2471 (1985).

[127] S. J. Stuart, J. Chem. Phys. **112**, 6472 (2000).

[128] A. C. T. van Duin, S. Dasgupta, F. Lorant, and W. A. G. III, J. Phys. Chem. **105**, 9396 (2001).

[129] D. W. Brenner, O. A. Sherendova, J. A. Harrison, S. J. Stuart, B. Ni, and S. B. Sinnott, J. Phys. Condens. Matt. **14**, 783 (2001).

[130] I. García-Mata, O. V. Zhirov, and D. L. Shepelyansky, Eur. Phys. J. D. **41**, 325 (2007).

[131] A. Vanossi, N. Manini, and E. Tosatti, Proc. Natl. Acad. Sci. USA **109**, 16429 (2012).

[132] F. G. Major, V. N. Gheorghe, and G. Werthe, *Charged particles trap* (Springer-Verlag, Berlin, Germany, 2005).

[133] A. Bylinskii, D. Gangloff, and V. Vuletic, Science **348**, 1115 (2015).

[134] D. Gangloff, A. Bylinskii, I. Counts, W. Jhe, and V. Vuletic, Nat. Phys. (2015).

[135] J. Krim, D. H. Solina, and R. Chiarello, Phys. Rev. Lett. **66**, 181 (1991).

[136] L. Bruschi, A. Carlin, and G. Mistura, Phys. Rev. Lett. **88**, 046105 (2002).

[137] J. Krim, Nano Today **2**, 38 (2007).

[138] A. Vanossi and O. M. Braun, J. Phys.: Condens. Matter **19**, 305017 (2007).

[139] J. P. Schiffer, Phys. Rev. Lett. **70**, 818 (1993).

[140] S. Fishman, G. De Chiara, T. Calarco, and G. Morigi, Phys. Rev. B **77**, 064111 (2008).

[141] M. G. Raizen, J. M. Gilligan, J. C. Bergquist, W. M. Itano, and D. J. Wineland, Phys. Rev. A **45**, 6493 (1992).

[142] G. Morigi and S. Fishman, Phys. Rev. Lett. **93**, 170602 (2004).

[143] G. Morigi and S. Fishman, Phys. Rev. E **70**, 066141 (2004).

[144] E. Shimshoni, G. Morigi, and S. Fishman, Phys. Rev. A **83**, 032308 (2011).

[145] D. Mandelli and E. Tosatti, Nature **526**, 332 (2015).

[146] D. Mandelli and E. Tosatti, Unpublished results.

[147] J. Hasnain, S. Jungblut, and C. Dellago, Nanoscale **6**, 10161 (2014).

[148] M. Reguzzoni, M. Ferrario, S. Zapperi, and C. Righi, Proc. Natl. Acad. Sci. USA **107**, 1311 (2010).

[149] J. Hasnain, S. Jungblut, and C. Dellago, Soft Matter **9**, 5867 (2013).

[150] D. Mandelli, A. Vanossi, N. Manini, and E. Tosatti, Phys. Rev. Lett. **114**, 108302 (2015).

[151] A. D. Novaco and J. P. Mc Tague, Phys. Rev. Lett. **38**, 1286 (1977).

[152] R. Zhang, Z. Ning, Y. Zhang, Q. Zheng, Q. Chen, H. Xie, Q. Zhang, W. Qian, and F. Wei, Nature Nanotech. **8**, 912 (2013).

[153] A. Nigues, A. Siria, P. Vincent, P. Poncharal, and L. Bocquet, Nature Mater. **13**, 688 (2014).

[154] D. Dietzel, C. Ritter, T. Mönninghoff, H. Fuchs, A. Schirmeisen, and U. Schwarz, Phys. Rev. Lett. **101**, 125505 (2008).

[155] D. Dietzel, M. Feldmann, U. Schwarz, H. Fuchs, and A. Schirmeisen, Phys. Rev. Lett. **111**, 235502 (2013).

[156] B. N. J. Persson, E. Tosatti, D. Fuhrmann, G. Witte, and C. Wöll, Phys. Rev. B **59**, 11777 (1999).

[157] M. Pierno, L. Bruschi, G. Mistura, G. Paolicelli, A. di Bona, S. Valeri, R. Guerra, A. Vanossi, and E. Tosatti, Nat. Nanotech. **106**, 1 (2015).

[158] A. Vigentini, B. Van Hattem, E. Diato, P. Ponzellini, T. Meledina, A. Vanossi, G. T. Santoro, E., and N. Manini, Phys. Rev. B **89**, 094301 (2014).

[159] G. Trambly de Laissardière, D. Mayou, and L. Magaud, Nano Lett. **10**, 804 (2010).

[160] F. Grey and J. Bohr, Europhys. Lett. **18**, 717 (1992).

[161] P. San-Jose, A. Gutièrrez-Rubio, M. Sturla, and F. Guinea, Phys. Rev. B **90**, 075428 (2014).

[162] S. Bleil, H. H. von Grünberg, J. Dobnikar, R. Castañeda-Priego, and C. Bechinger, Europhys. Lett. **73**, 450 (2006).

[163] C. G. Shaw, S. C. Fain, and M. D. Chinn, Phys. Rev. Lett. **41**, 955 (1978).

[164] T. Aruga, H. Tochihara, and Y. Murata, Phys. Rev. Lett. **52**, 1794 (1984).

[165] M. S. Tomassone, J. B. Sokoloff, A. Widom, and J. Krim, Phys. Rev. Lett. **79**, 4798 (1997).

[166] H. Shiba, J. Phys. Soc. Jpn. **46**, 1852 (1979).

[167] H. Shiba, J. Phys. Soc. Jpn. **48**, 211 (1980).

[168] O. Braun, M. Paliy, and B. Hu, Phys. Rev. Lett. **83**, 5206 (1999).

[169] J. Krim, Adv. Phys. **61**, 155 (2012).

[170] B. Bhushan, J. Israelachvili, and U. Landman, Nature **374**, 607 (2002).

[171] M. Urbakh, J. Klafter, D. Gourdon, and J. Israelachvili, Nature **430**, 525 (2004).

[172] J. W. M. Frenken, Nature Nanotech. **1**, 20 (2006).

[173] S. Kawaia, M. Kochc, E. Gnecco, A. Sadeghi, R. Pawlak, T. Glatzel, J. Schwarz, S. Goedecker, S. Hecht, A. Baratoff, L. Grill, and E. Meyer, Proc. Natl. Acad. Sci. USA **111**, 3968 (2014).

[174] H. Hedgeland, P. Fouquet, A. P. Jardine, G. Alexandrowicz, W. Allison, and J. Ellis, Nature Phys. **5**, 561 (2009).

[175] T. Junno, K. Deppert, L. Montelius, and L. Samuelson, Appl. Phys. Lett. **66**, 3627 (1995).

[176] M. Sitti and H. Hashimoto, IEEE-ASME Trans. Mechatron. **5**, 199 (2000).

[177] J. A. Hurtado and K.-S. Kim, Proc. R. Soc. Lond. A **455**, 3363 (1999).

[178] J. A. Hurtado and K.-S. Kim, Proc. R. Soc. Lond. A **455**, 3385 (1999).

[179] M. Müser, L. Wenning, and M. O. Robbins, Phys. Rev. Lett. **86**, 1295 (2001).

[180] M. Müser, M. Urbakh, and M. Robbins, Adv. Chem. Phys. **126**, 187 (2003).

[181] Y. Gao, J. Mech. Phys. Solids **58**, 2023 (2010).

[182] A. Erdemir and J.-M. Martin, *Superlubricity* (Elsevier Science Amsterdam, Amsterdam, Netherlands, 2007).

[183] M. Hirano and K. Shinjo, Phys. Rev. B **41**, 11387 (1990).

[184] A. Schirmeisen and U. D. Schwarz, Chem. Phys. Chem. **10**, 2373 (2009).

[185] A. Vanossi and E. Tosatti, Nature Mater. **11**, 97 (2012).

[186] A. Carlin, L. Bruschi, M. Ferrari, and G. Mistura, Phys. Rev. B **68**, 045420 (2003).

[187] P. Zeppenfeld, U. Becher, K. Kern, and G. Comsa, Phys. Rev. B **45**, 5179 (1992).

[188] L. W. Bruch, R. D. Diehl, and J. A. Venables, Rev. Mod. Phys. **79**, 1381 (2007).

[189] L. Bruschi, M. Pierno, G. Fois, F. Ancilotto, G. Mistura, C. Boragno, F. B. de Mongeot, and U. Valbusa, Phys. Rev. B **81**, 115419 (2010).

[190] J.-Y. Park, S.-J. Kahng, U. D. Ham, Y. Kuk, K. Miyake, K. Hata, and H. Shigekawa, Phys. Rev. B **60**, 16934 (1999).

[191] R. L. Renner, J. E. Rutledge, and P. Taborek, Phys. Rev. B **63**, 233405 (2001).

[192] G. Mistura, private communication.

[193] K. Kern, P. Zeppenfeld, R. David, and G. Comsa, Phys. Rev. Lett. **59**, 79 (1987).

[194] J. L. F. Da Silva, C. Stampfl, and M. Scheffler, Phys. Rev. B **72**, 075424 (2005).

[195] J. L. F. Da Silva, "The nature and behavior of rare-gas atoms on metal surfaces", PhD thesis (Technische Universität Berlin, 2002).

[196] M. M. van Wijk, M. Dienwiebel, J. W. M. Frenken, and A. Fasolino, Phys. Rev. B **88**, 235423 (2013).

[197] M. R. Sorensen, K. W. Jacobsen, and P. Stoltze, Phys. Rev. B **53**, 2101 (1996).

[198] S. V. P. Ticco, G. Fornasier, N. Manini, G. E. Santoro, E. Tosatti, and A. Vanossi, arXiv:1508.06201 [cond-mat.mes-hall] (2015).

[199] A. Vanossi, N. Manini, G. Divitini, G. E. Santoro, and E. Tosatti, Phys. Rev. Lett. **97**, 056101 (2006).

[200] M. Cesaratto, N. Manini, A. Vanossi, E. Tosatti, and G. E. Santoro, Surf. Sci. **601**, 3682 (2007).

[201] A. Vanossi, N. Manini, F. Caruso, G. E. Santoro, and E. Tosatti, Phys. Rev. Lett. **99**, 206101 (2007).

[202] I. E. Castelli, R. Capozza, A. Vanossi, G. Santoro, N. Manini, and E. Tosatti, J. Chem. Phys. **131**, 174711 (2009).